Università degli Studi di Palermo

AREA RICERCA E TRASFERIMENTO TECNOLOGICO
SETTORE DOTTORATI E CONTRATTI PER LA RICERCA
U. O. DOTTORATI DI RICERCA

Tecnologie e Scienze per la salute dell'Uomo
Dipartimento Scienze e Tecnologie Biologiche Chimiche e Farmaceutiche (STEBICEF)
SSD CHIM/09

Tailored Polymers for Advanced Biomedical Devices: Electroactive Bioadhesive Coatings for Drug Delivery and Electrospun Scaffolds for Improved Biointegration and Functionality

IL DOTTORE
Giovanni Carlo Miceli

IL COORDINATORE
Prof. Bruno Giuseppe Pignataro

IL TUTOR
Prof. Mariano Licciardi

IL CO TUTOR
Prof. Fabio Salvatore Palumbo

CICLO - XXXVI
2024

Abstract

This PhD thesis delves into the principles governing the behaviour, synthesis, processing, and application of polymers. The first section will discuss a novel biodegradable segmented polyurethane urea that was synthesized, characterized, and processed as a biomaterial. It exhibits outstanding hydrolytic resistance against degradation, a low melting point of 55°C and exceptional adhesion after melting. Notably, its adhesion to high-energy surfaces such as glass and metal at room temperature reached 2.6 MPa. Moreover, when evaluated against porcine skin underwater at 37°C, the adhesion measured an impressive 30 kPa. These findings underscore the versatile adhesion properties of the material across different conditions and surfaces, highlighting its potential for various applications, especially in contexts involving biological interfaces. For instance, as a coating interface between metallic prostheses or implantable devices and biological tissues, to improve biological tolerance and biointegration. Consequently, poly(3,4-ethylenedioxythiophene) (PEDOT) doped with polystyrene sulfonate was integrated into the bioadhesive polyurethane urea matrix to create a conductive bioadhesive coating. It was designed for insertion into the tumour microenvironment, with the capability to deliver drugs upon the application of voltage. The resulting polymer underwent comprehensive characterization through electrochemical impedance spectroscopy, conducted in both wet and dry conditions, and cyclic voltammetry. Then, paclitaxel was incorporated in the PEDOT-doped polyurethane urea matrix and porous titanium rods were dip-coated into the loaded polymeric solution. These final devices were designed around the neurosurgical toolkit to perform a biopsy and will

be supported by a cartridge during the insertion. The assessment of drug release was conducted in physiological-like conditions and the in vitro effects were evaluated using a neuroblastoma cell line (SH-SY5Y). Furthermore, the intricate relationship between the applied voltage and the efficacy of the delivered drug was investigated, unravelling crucial insights into optimizing tumour treatment strategies.

The second section of this thesis is dedicated to an electrospun scaffold crafted from polybutylene succinate (PolyBS), specifically designed for tissue engineering applications. The scaffold's morphology was optimized to create a small-diameter conduit featuring interconnected micro-porosity. This design aims to facilitate cell integration, adhesion, and growth, while simultaneously preventing undesirable cellular infiltration through the graft's wall. The mechanical properties of the scaffolds were thoroughly analyzed and compared to those of native conduits. To assess cytocompatibility in vitro, the scaffolds were seeded with adult normal human dermal fibroblasts. Additionally, the haemolytic effect was evaluated following incubation with diluted whole blood. After these in vitro analyses, the in vivo effects were explored by implanting these microfibrillar scaffolds to address critical bone defects. This multifaceted investigation seeks to comprehensively understand the scaffold's performance, both in terms of mechanical properties and its interaction with biological systems, thus contributing valuable insights to tissue engineering applications.

LIST OF FIGURES

INDEX

1. Introduction

Biomaterials

In an era marked by unprecedented medical science and technology advances, biomaterials have emerged producing innovative solutions to pressing healthcare challenges. From life-saving implants to drug delivery systems, biomaterials have transformed the landscape of medicine [1–3]. Biomaterials, commonly defined as materials employed in medical devices, are subject to an evolving interpretation and increasing sophistication. As such, their definition and application continue to evolve in response to technological advancements and emerging medical needs. Humankind's use of materials to repair the body dates to antiquity when natural materials such as wood or metals were used to structurally replace tissues lost to disease or trauma (Figure 1).

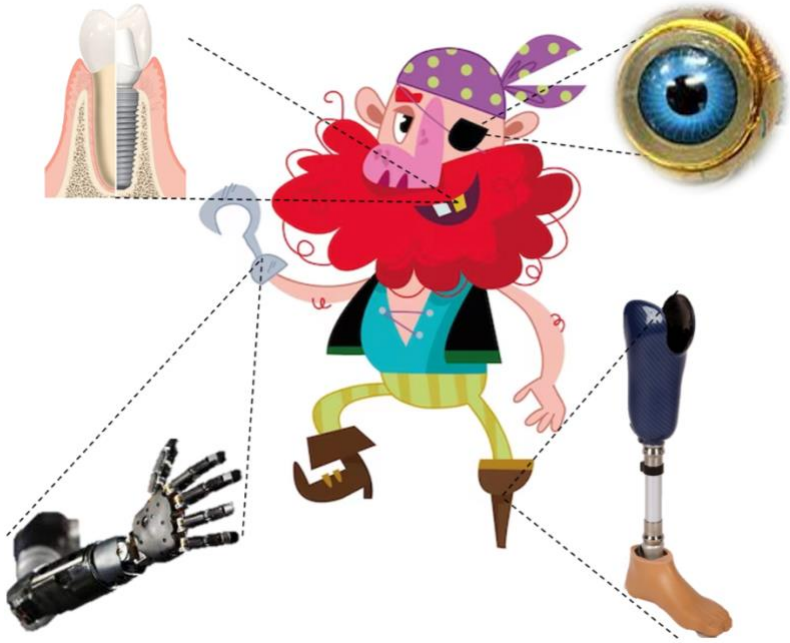

Figure 1 Advancements in biomaterials over the centuries.

Nowadays, advancements in materials science have led to the development of new biomaterials such as polymers, ceramics, and metal alloys that are successfully integrated into healthcare practices [4–6]. Polymeric materials are widely employed due to their ease of fabrication, flexibility, and biocompatible nature. Additionally, they offer a diverse array of mechanical, electrical, chemical, and thermal behaviours, especially when combined with other materials as composites.

Polymers

Polymers are macromolecular compounds, composed of repeating units of monomers, that emerged as a fundamental cornerstone of modern materials science and engineering. With their diverse and versatile properties, from high strength and durability to flexibility and lightweight properties, they changed every aspect of our

daily lives. Nevertheless, their allure doesn't lie only in their remarkable diversity but also in their potential for tailoring properties to meet specific needs. This adaptability is achieved through the careful manipulation of molecular structures and the control of processing conditions, giving rise to a multitude of specialized polymer materials. The precise design and engineering of polymers have opened new avenues for addressing pressing global challenges, including sustainability and resource conservation. Researchers are increasingly exploring renewable sources and green chemistry principles to create polymers that are more environmentally friendly and have a reduced ecological footprint. The use of degradable polymers in medical applications is not a new concept. Indeed, their use for implants which only serve a temporary function has been of interest for more than 40 years [7]. Subsequently, poly(lactic acid) (PLA) and poly(glycolic acid) (PGA), poly(caprolactone) (PCL), and their respective copolymers such as poly(lactic-co-glycolic acid) (PLGA) have been used in applications ranging from solid implantable devices to drug delivery devices [8–10]. From a chemical perspective, the design possibilities are limited only by creativity, time, and resources. Hence, there are likely more suitable materials for in vivo use yet to be discovered or translated to the clinic. In several instances, the materials used for medical treatment do not possess the mechanical and physical properties that match the tissues they are meant to treat. This makes it challenging for the materials to fit perfectly, much like attempting to fit a square peg into a round hole. Although there has been significant growth in the understanding and development of new polymeric biomaterials for various biomedical applications over the past few decades, a clear need for further innovation and comprehension of biomaterials remains.

Synthetic polymers

During the twentieth century, there was a significant improvement in the field of materials science as synthetic polymers gradually replaced their naturally derived counterparts. This advancement led to a notable enhancement in performance, functionality, and reproducibility. Indeed, synthetic polymers outperformed their naturally derived counterparts in these aspects. This shift was instrumental in developing various synthetic materials that are widely used in numerous industries today (Figure 2).

Figure 2 Synthetic materials widely used today.

Polyethylene and polypropylene, for instance, are the ultimate game-changers in the world of packaging. Their lightweight, flexible, and chemically resistant properties have revolutionized the industry, making them the go-to materials for manufacturers

worldwide. Not only do they reduce weight, but they also enhance durability, ensuring that products stay secure and well-protected during storage and transportation. Polyethylene Terephthalate's transparent and lightweight nature, coupled with recyclability, has transformed beverage and food packaging. Furthermore, it can be used to develop synthetic fibres offering durability and performance. Polyurethanes are a type of synthetic polymer known for their remarkable versatility and durability. This polymer can be produced in a wide range of forms, from rigid to flexible, making it suitable for a diverse range of applications. Polyurethanes are used in the production of foam insulation, mattresses, coatings, adhesives, and elastomers. One of the most significant advantages of polyurethanes is their ability to be customized to meet specific needs in terms of hardness, density, and other properties. They are also highly resistant to abrasion, chemicals, and weathering, making them ideal for outdoor applications. Polyurethanes are a type of thermoplastic polymers that are segmented due to the presence of both soft and hard domains within their structure. The hard segments are crystalline or semi-crystalline and provide stiffness, while the soft segments are amorphous and offer flexibility. These polymers also contain a chain extender and a urethane group. Due to their exceptional properties, polyurethanes have become one of the most popular and widely used synthetic polymers in the world.

Synthetic polymers can be tailored on a molecular level, blended with other polymers or functionalized to fit any requirement that should be met for a specific application.

- **Molecular Weight:** synthetic polymers, like all polymers, are large molecules composed of repeating structural units called monomers. These monomers can be combined in different ways to create a wide range of polymers with

varying properties and characteristics. The process of polymerization can be controlled to achieve specific molecular weights, which can be either high or low, depending on the intended application of the polymer. For instance, high molecular weight polymers are often used in industries such as construction, where their strength and durability are important factors, while low molecular weight polymers are commonly used in the production of coatings, adhesives, and other products that require good flow and wetting properties.

- **Flexibility:** the flexibility of a polymer depends on several factors, including its chemical composition, molecular weight, and the arrangement of its structural units. Some polymers are highly flexible, allowing them to bend and stretch without breaking, while others may be more rigid. The degree of flexibility of a synthetic polymer is tailored by its intended use, as certain applications require more flexibility than others.
- **Chemical and Weathering resistance:** synthetic polymers can exhibit resistance to environmental factors such as sunlight, moisture, temperature variations and even chemical reactions with other substances. This property makes them suitable for applications where exposure to various chemicals is a concern or for outdoor applications and long-term use.
- **Biocompatibility:** synthetic polymers can be tailored on a molecular level to control degradation rate or modulate cell behaviour mimicking the ECM. They can also be blended with other polymers to fit any requirement that should be met to function as an integral part of the damaged tissue. The common materials for synthetic scaffolds are biodegradable polymers, such as polyvinyl alcohol (PVA), poly (lactic acid) (PLA), polyethylene oxide (PEO), poly

(glycolic acid) (PGA), poly (ε-caprolactone) (PCL), polyethylene glycol (PEG) and polyurethane (PU) [11–13].

- **Processability:** synthetic polymers can be easily processed into various forms, including fibres, films, and moulded shapes. This makes them versatile and suitable for a wide range of manufacturing processes. One of the next paragraphs will provide a detailed discussion of the electrospinning technique.
- **Adhesion:** synthetic polymers are used in adhesive formulations or as coatings to enhance adhesion between different materials. The bonding strength between the polymer and the adherend depends on chemical interaction, surface energy and mechanical interlocking. Moreover, it could be improved using surface treatments or introducing adhesion promoters compounds.
- **Conductivity:** refers to the ability of a material to allow the flow of electric current. Polymers are usually insulative, but some exhibit electrical conductivity, making them useful in electronic and electrical applications. Conductive polymers often have conjugated double bonds along their backbone, allowing the delocalization of electrons and facilitating electrical conduction.

In summary, synthetic polymers have limitless possibilities and their potential depends on creativity, resources, and time. The following paragraphs will discuss adhesion properties and conducting polymers in detail. It's worth noting that the balance between adhesion and conductivity can be crucial in certain applications, such as in the design of flexible electronic devices where both properties are essential for functionality.

Adhesion properties

Adhesion is a physicochemical phenomenon of attraction between dissimilar molecular species. It is caused by molecular interactions at the interface between materials but also depends on surface properties and environmental conditions [14]. For instance, high-energy surfaces favour adhesion while high temperatures reduce it. Furthermore, spreading adhesives is essential to allow the best distribution of stresses between bonded joints. When at least one of these joints is a biological component (i.e., tissue, organ, or cell) the adhesive is known as a bioadhesive [15]. Cyanoacrylate-based, characterized by high bonding strength and short glueing time, were the first used bioadhesives and are currently used in plastic surgery, skin transplantation and emergency wound treatment [8,16]. Yet, these products are limited to topical conditions due to their toxic degradation products [17]. Glutaraldehyde-based bioadhesives possess strong wet bonding strength and have been widely used in Europe and Japan for treating aortic dissections and in diverse surgical operations. Nevertheless, the formaldehyde molecule carries mutagenicity and carcinogenicity [18,19]. Compared to glutaraldehyde-based bioadhesives, the cytotoxicity of dextran-polylysine is 1000 lower while maintaining a remarkable adhesion strength [20]. In adhesion technology, it is well-known that water is the main reason for adhesive failure [21]. Indeed, there are several ways in which it can compromise the performance of the adhesive, like interfacial wicking and crazing or it can induce swelling and hydrolysis [22]. However, nature is a source of inspiration by providing many outstanding examples of adhesive strategies (Figure 3).

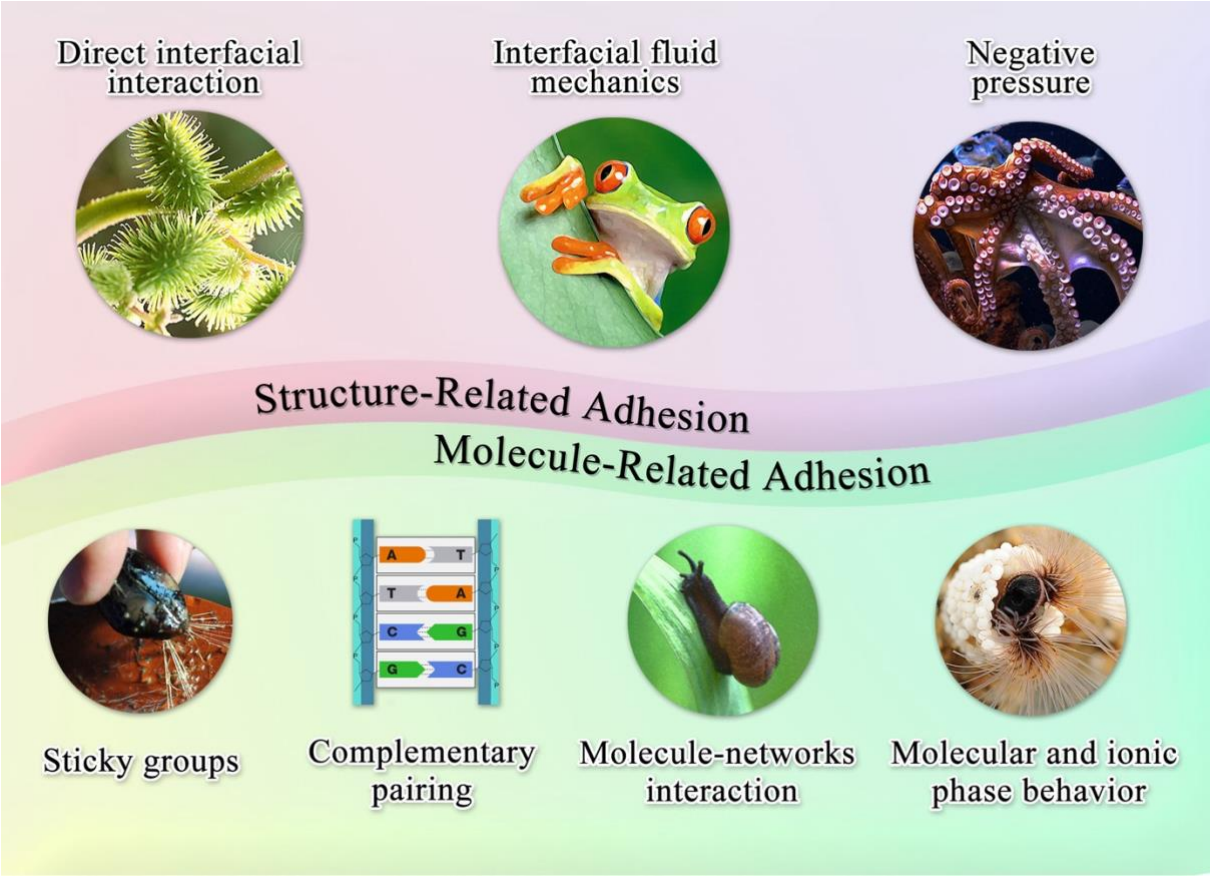

Figure 3 Biomimetic examples of adhesive strategies

The challenges of developing tough and robust underwater bonding are analogous to the adhesion problems solved by many marine organisms, which have developed adhesive strategies to deal with the dynamic sea environment [23]. Marine mussels are naturally equipped with reliable strategies to achieve interfacial adhesion, at the tidal interface, in dynamic and turbulent environments. Mussels are bivalve molluscs, and their foot enables them to attach by byssus threads to a solid substrate. The byssus is a bundle of radially distributed threads that terminates in an adhesive plaque attached to rocks preventing them from being dislodged and crushed by turbulence and waves. They attach to inanimate and living surfaces in both freshwater and marine environments by secreting adhesive proteins that harden in situ. These proteins, isolated from mussel byssus, have been shown to bond with numerous

substrates including glass, Teflon, wood, concrete, plastics, metals, biological cell lines, bone, teeth, and others [24–27]. Nevertheless, these outstanding adhesive systems that allow them to affix themselves over wide ranges of temperature, salinities and movements are not yet well mimicked by human technologies. Therefore, the exploration of biomaterials that are capable of strongly, but safely, interacting with tissues is never-ending. Indeed, scientists have performed detailed studies of the chemistry behind the complex adhesion mechanisms of mussels as a potential source for a water-resistant bioadhesive, opening a wide range of possible applications [28]. Surgical glues could ensure a faster wound closure than conventional stitching methods and avoid the damage caused by sutures. Mehdizadeh et al. prepared injectable biodegradable adhesives that promote wound healing while avoiding inflammation [29]. Bioadhesive drug delivery systems could reach different body regions to locally release drugs over extended periods. Xu et al. used a sulfasalazine-loaded catechol-modified chitosan hydrogel as an injectable mucoadhesive formulation to treat ulcerative colitis [30]. Indeed, inorganic implantable materials have been widely used in various biomedical applications such as metallic endoprosthesis, bioactive glasses or ceramics, sensors, or devices for nerve stimulation [31,32]. However, the integration of these materials with biological tissues often presents challenges related to poor adhesion and sealing at the interface, mechanical mismatch, and inflammatory tissue response that can lead to scar tissue encapsulation of the implant and subsequent device failure. Bioadhesive coatings play a crucial role in improving the performance and functionality of inorganic implantable materials by promoting tissue adhesion, reducing implant-related complications, and improving long-term biocompatibility. These coatings act as a bridge between the implant surface and the surrounding biological environment

promoting tissue integration, reducing inflammation and infection rates, and improving the long-term stability of implants. The biomedical applications of these bioadhesive coatings span from orthopaedic implants, to promote osteointegration and improve implant stability, to cardiovascular stents, neural implants, and tissue engineering scaffolds, which improve biointegration and reduce complications such as mechanical mismatch, thrombosis and implant migration. In the tissue engineering field, mussel-inspired bioadhesives could guarantee tissue adhesion while carrying biomolecules to induce cell growth [27]. However, glues do have not suitable physical properties to be processed as biomaterials with controlled shapes and architectures. The synthesis of a bioadhesive polymer that can be processed with specific manufacturing techniques as a solid biomaterial could increase the current biomedical applications of tissue adhesive biomaterials.

Conductive polymers

The discovery of conductive polymers dates to the late 20th century, and since then, researchers have made significant strides in understanding their structure, properties, and potential applications. Unlike conventional polymers that are insulators, conductive polymers possess the unique ability to exhibit electrical conductivity while still retaining all the other characteristics that are common in other polymers like processability or tunability. This distinctive characteristic has made conductive polymers a fascinating class of materials, that merge the unique properties of both organic polymers and conductive materials, for an even wider

range of applications like flexible electronics, sensors, actuators, energy storage or biomaterials [33–35].

Conducting polymers are often compared to metals in terms of their electrical conductivity, flexibility, processability, and specific applications. While metals excel in high conductivity and stability, conductive polymers offer advantages in terms of flexibility, processability, and corrosion resistance. Each has its own advantages and disadvantages, and the choice between them depends on the specific application and the required properties.

- **Applications**: metals are commonly used in traditional electronics, wiring, structural components, and applications where high conductivity and rigidity are essential. Instead, conductive polymers find applications in flexible electronics, wearable devices, sensors, organic photovoltaics, and bioelectronic devices, where their flexibility and processability are advantageous.
- **Flexibility**: metals are generally stiff and not very flexible. Although they can undergo a certain degree of deformation, repeated bending may cause structural fatigue and ultimately result in failure. Conductive polymers, on the other hand, are often more flexible than metals since their molecular structure enables them to bend and stretch without significant loss of conductivity, making them suitable for applications where the material needs to be conformable or integrated into flexible devices.
- **Processability**: metals are typically more challenging to process compared to conductive polymers. Metal shaping often involves casting, machining, or other methods that require significant energy and resources. Contrariwise, conductive polymers are more versatile in terms of processing. They can be

solution-processed, coated, or even printed onto various substrates, allowing for cost-effective and scalable manufacturing.

- **Corrosion resistance**: conductive polymers are generally more resistant to corrosion than metals, making them suitable for use in corrosive environments where metal would be unsuitable due to its susceptibility to corrosion, which can impact both its conductivity and structural integrity.
- **Functionalization**: conducting polymers can be chemically modified with various side groups, allowing for the introduction of specific properties or the attachment of biomolecules, making them highly customizable.
- **Weight**: metals have higher density and are heavier compared to conductive polymers that are lightweight, therefore the second ones are more suitable for applications where weight is a critical factor.
- **Electrical conductivity**: metals are known for their ability to conduct electricity very well. They have a high density of free electrons that can move easily, facilitating efficient electrical conduction. Therefore, they typically exhibit higher electrical conductivity compared to most conductive polymers. Nevertheless, Conductive polymers can still exhibit remarkable conductivity, especially when doped. Furthermore, their conductivity can be tailored by adjusting factors such as doping level, chemical structure, and environmental conditions.

A crucial process in enhancing the electrical conductivity of conducting polymers is doping. This term, borrowed from semiconductor physics, refers to the introduction of dopant molecules or ions into the polymer matrix. The dopants disrupt the polymer's electronic structure, leading to the formation of charge carriers (electrons or holes) and facilitating the conduction of electricity. Indeed, conducting polymers typically

undergo doping processes, where the introduction of dopant molecules imparts electrical conductivity by altering the charge-carrier concentration.

There are two primary types of doping in conducting polymers: n-type (negative) doping and p-type (positive) doping (Figure 4).

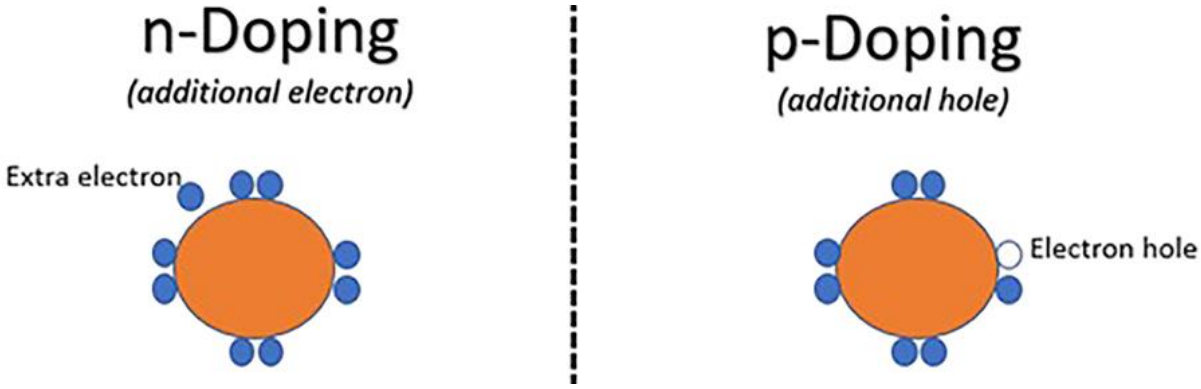

Figure 4 Doping in conducting polymers.

In **p-type doping**, electron acceptors are introduced into the polymer matrix. These acceptors tend to attract electrons, creating electron deficiencies or "holes" in the polymer structure. Common electron acceptors include oxidizing agents such as iodine, bromine, and transition metal salts. For example, polypyrrole (PPy) can be p-doped with ferric chloride ($FeCl_3$) to enhance its electrical conductivity.

Instead, **n-type doping** involves the introduction of electron-donating species into the polymer matrix. These donors provide additional electrons to the polymer, increasing its electron density and conductivity. Common electron donors include reducing agents such as alkali metals (e.g., sodium or lithium) or organic molecules with electron-rich moieties. An example is the n-doping of polythiophene using sodium naphthalenide.

The doping process can be reversible, allowing for the switching between conducting and insulating states by removing or adding dopant molecules. This feature is particularly valuable in applications such as sensors and actuators [36].

The choice of dopant can significantly influence the properties of the conducting polymer, including its conductivity, stability, and optical characteristics. Common conducting polymers include polyaniline, polypyrrole, polythiophene, polyfuran, and polyphenylene (Figure 5).

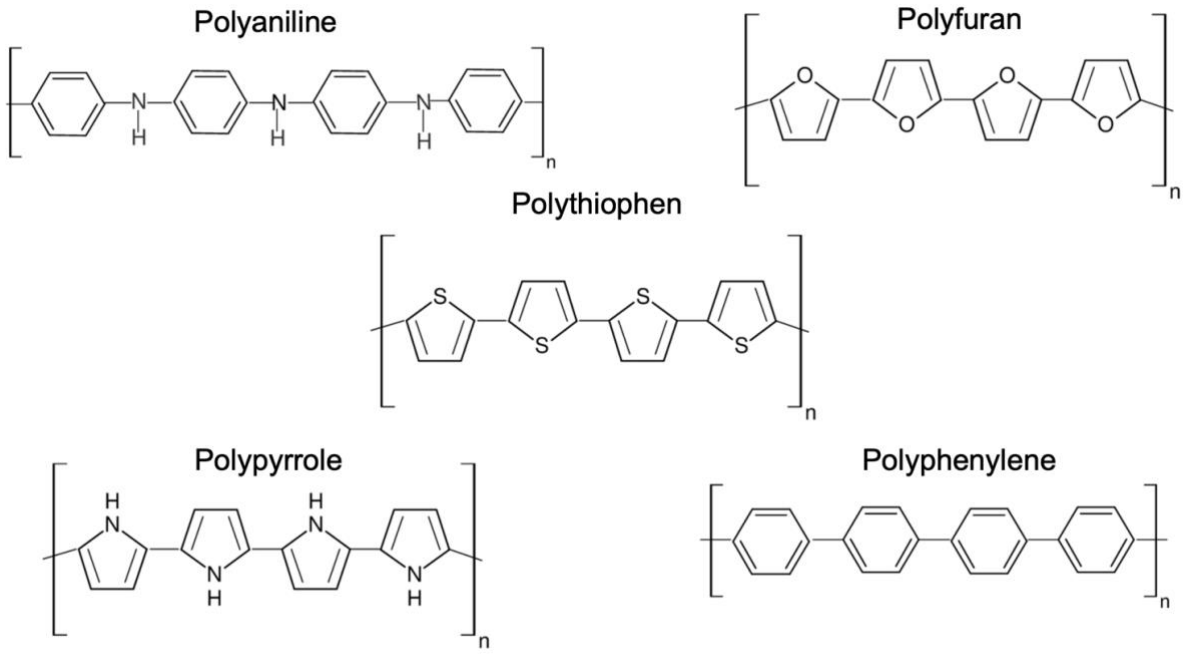

Figure 5 Common conducting polymers.

- **Polyaniline** can exist in both conductive and non-conductive states, depending on its oxidation level. It undergoes reversible doping and dedoping processes, making it suitable for applications where switchable conductivity is desired, such as sensors, corrosion protection coatings, supercapacitors, and electronic devices due to its versatility and ease of synthesis.

- **Polypyrrole** is intrinsically conductive and can achieve high electrical conductivity. Similar to polyaniline, polypyrrole undergoes reversible doping and dedoping processes, allowing for conductivity modulation hence their applications are similar as well.
- **Polyfuran** exhibits moderate electrical conductivity. It can be doped to enhance its conductivity, and the doping process is generally reversible. It has been explored for use in organic electronics, including field-effect transistors and photovoltaic devices.
- **Polyphenylene** can exhibit both conductive and insulating properties, depending on its structure. Its conductivity can be influenced by its chemical structure and doping, but it may not undergo reversible doping to the same extent as some other conducting polymers. Its derivatives find use in organic electronic devices, such as transistors and sensors.
- **Polythiophene** is known for its high electrical conductivity. It undergoes reversible doping and dedoping processes, providing control over its conductivity. Polythiophene is widely employed in organic photovoltaic cells, organic field-effect transistors, and light-emitting diodes.

Researchers often tailor the doping process to achieve specific performance requirements for a given application. As suggested by percolation theory, a minimum amount of conductive polymer is necessary to establish a conductive pathway within an insulative matrix [37].

Percolation theory is a mathematical framework used to study the behaviour of connected clusters in random networks. It has applications in various fields such as physics, materials science, biology, and computer science. The theory was initially

developed to understand the flow of fluids through porous media, but it has since been generalized to study a wide range of phenomena involving connectivity. The basic idea behind percolation theory is to model a system as a network of interconnected nodes and edges. The nodes represent individual elements of the system (such as particles in a material or sites in a lattice), and the edges represent connections between these elements. These connections can be present with a certain probability. The process of percolation involves systematically adding or removing connections in the network based on a probability distribution. As connections are added, clusters of connected nodes begin to form. A key concept in percolation theory is the percolation threshold, which is the critical probability at which a giant connected cluster (percolating cluster) emerges and spans the entire system.

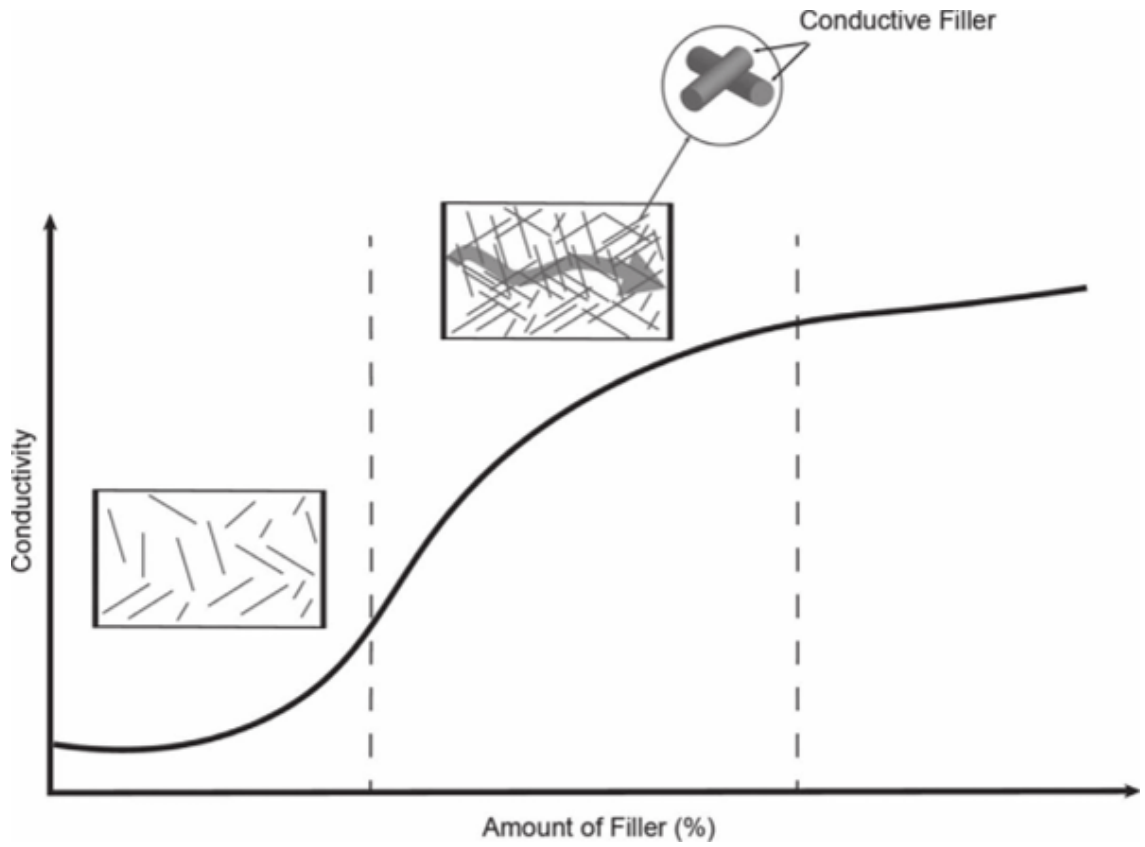

Figure 6 Conductive filler effects, within an insulative matrix, on conductivity.

The behaviour of a system near the percolation threshold is of particular interest. Below the threshold, the system consists of small, isolated clusters, while above the threshold, a giant cluster emerges, and the system becomes percolating. The properties of the percolating cluster, such as its size and shape, provide insights into the overall behaviour of the system. Percolation theory has been applied to various real-world phenomena, including the study of electrical conductivity in disordered materials, the spread of diseases in populations, and the robustness of networks. It provides a powerful framework for understanding the emergence of connectivity in random systems and has led to many interesting discoveries and insights in diverse scientific disciplines.

The ability to control and tailor the conductivity of these materials has paved the way for the development of advanced electronic devices with enhanced performance and functionality.

Poly(3,4-ethylenedioxythiophene):poly(styrene sulfonate), commonly known as PEDOT:PSS, is a conductive polymer blend that has gained significant attention for its unique characteristics and versatility in various applications [38–40]. PEDOT is intrinsically conductive, and its electrical conductivity can be further enhanced by doping. The most common dopant for PEDOT is poly(styrene sulfonate) (PSS), which improves its conductivity significantly.

Therefore, PEDOT:PSS is known for its relatively high electrical conductivity among organic materials (Figure 7).

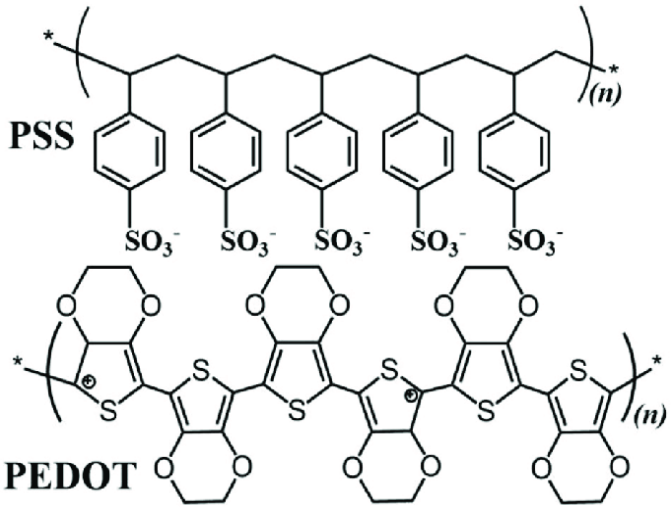

Figure 7 Chemical structure of PEDOT: PSS.

The combination of PEDOT and PSS results in a conductive composite multifunctional material that combines electrical conductivity with biocompatibility. These characteristics make it a promising biomaterial for various applications in the biomedical field, ranging from neural interfaces to biosensors and drug delivery

systems [41,42]. Indeed, the conductive and biocompatible nature of PEDOT:PSS makes it suitable for developing electrodes for neural recording and stimulation. The material's compatibility with neural tissue has shown promise in improving the performance and longevity of neural implants. Its ability to facilitate electron transfer and its compatibility with biomolecules is particularly relevant in the design of electrochemical biosensors for detecting specific biological markers or analytes. Lastly, researchers have explored the use of PEDOT:PSS as a platform for drug delivery. The conductive nature of the material allows for the controlled release of drugs through electrical stimulation, providing a potential avenue for developing smart drug delivery systems.

Drug delivery

Drug delivery refers to the method and process by which pharmaceutical substances are administered to achieve a therapeutic effect in humans or animals. The goal of drug delivery systems is to ensure that the drug reaches its target site in the body in a controlled and effective manner, maximizing therapeutic benefits while minimizing side effects. There are various approaches and technologies employed in drug delivery, each tailored to address specific challenges associated with different drugs and medical conditions. For instance, the choice of the route of drug administration. Oral administration is the most common and convenient route, and it involves the ingestion of drugs in the form of tablets, capsules, or liquid formulations. It is preferred because allows for self-administration without the need for specialized equipment or medical personnel. Tablets and capsules are designed to be swallowed

whole and are coated with a protective layer that helps prevent the drug from dissolving in the stomach. Liquid formulations, on the other hand, may be more easily absorbed and may be preferred for patients who have difficulty swallowing pills. However, it is important to note that not all drugs can be taken orally, as some may be destroyed by stomach acid or may not be absorbed effectively. Therefore, before choosing this route, it is important to consider the drug's ability to withstand stomach acid and choose an appropriate formulation to ensure safe and effective treatment. An injectable administration is often used for rapid and controlled drug release. It can be subcutaneous, intramuscular, or intravenous to allow for precise delivery of drugs into the bloodstream, bypassing the digestive system. A topical administration can be applied to the skin or mucous membranes for local effects. This includes creams, ointments, patches, and transdermal delivery systems. The inhalation of gases or aerosolized particles can directly reach the respiratory system. This is common for treating respiratory conditions and provides rapid absorption into the bloodstream. Lastly, some drugs are delivered using implantable devices, such as pumps or controlled-release systems, providing a sustained release over an extended period. These systems can be used to control the drug release over an extended period, maintaining therapeutic levels in the bloodstream and reducing the frequency of administration. They can also be used to enable the delivery of drugs to specific cells or tissues, minimizing damage to healthy cells and enhancing the therapeutic effect. The release of a substance can be designed to occur specifically at a desired site using advanced drug delivery systems that can respond to specific physiological conditions such as pH or enzyme levels. Additionally, external stimuli such as light or heat can also trigger the release of the substance. This level of precision is particularly significant in cancer treatment, where the delicate balance between

therapeutic efficacy and minimizing adverse effects is paramount. Indeed, cancer remains one of the most formidable challenges in modern healthcare, with approximately 14.1 million new cases diagnosed annually [43].

Chemotherapy

Chemotherapy stands as one of the foremost methods employed in contemporary cancer treatment. This approach utilizes pharmacological agents, commonly referred to as chemotherapeutic drugs, against cancer cells to impede the uncontrolled proliferation of cancer cells, preventing the occurrence of metastases, and ultimately eliminating the tumor. By leveraging the cytotoxic properties of specific drugs, chemotherapy aims to disrupt the rapid division and growth of cancer cells. The history of chemotherapeutic agents began 70 years ago and since then several drugs have been discovered and tested [44]. In combination with other treatment modalities such as surgery, radiation therapy, and immunotherapy, chemotherapy plays a vital role in comprehensive cancer care, contributing to improved survival rates and enhanced quality of life for many patients. Although chemotherapy is a potent tool against cancer, it often comes with side effects due to its impact on rapidly dividing normal cells, necessitating a delicate balance between therapeutic efficacy, and minimizing adverse reactions. The complex and diverse nature of cancer demands innovative approaches across various domains, including early detection, personalized treatment strategies, and advanced delivery systems. Regional chemotherapy stands out as an alternative to conventional anticancer treatments, offering a targeted approach by releasing potent anticancer agents directly at the

tumour site [45]. This strategy holds great promise in overcoming some of the limitations associated with traditional cancer treatments. It allows for more precise and focused delivery of therapeutic agents, increasing their concentration at the tumour site while sparing healthy tissues from unnecessary exposure.

The treatment of solid tumours, which represent more than 85% of human cancers, is challenging due to unfavourable pharmacokinetics, poor delivery, low local concentrations, and limited accumulation in target cells [46]. By employing biomaterials as carriers for anticancer agents, regional chemotherapy seeks to enhance drug stability, improve pharmacokinetics, and enable sustained release over time [47].

Recent advancements in materials science have led to the development of state-of-the-art materials characterized by organized structures and high performance. A noteworthy example is stimuli-responsive polymers, often termed "smart" or "intelligent" polymers, capable of undergoing chemical and/or physical alterations in response to internal or external stimuli [48,49]. These systems offer several advantages, including precise control of drug release rates and triggered, tunable, and targeted delivery. These features are particularly crucial in the delivery of chemotherapeutics, reducing the risk of unwanted side effects associated with off-target drug action and minimizing the need for high drug doses. Additionally, they can mitigate the harmful effects of burst release, commonly referred to as dose-dumping [50,51].

Electroactive materials represent a class of stimuli-responsive systems capable of triggering drug release upon the application of an electrical stimulus [52]. Within drug delivery, conductive polymers serve as electrical switches, offering unparalleled control over drug release [53]. Furthermore, electric fields find applications in electroporation and iontophoresis, facilitating the transport of drug molecules through membranes, and directly utilized in the treatment of tumors [54].

Glioblastoma multiforme

Glioblastoma multiforme (GBM) is a highly aggressive and malignant type of brain tumour. The term "multiforme" reflects the histological diversity of the tumour cells within GBM. Under the microscope, the cells appear quite different from each other, and this heterogeneity is a characteristic feature of the tumour (Figure 8).

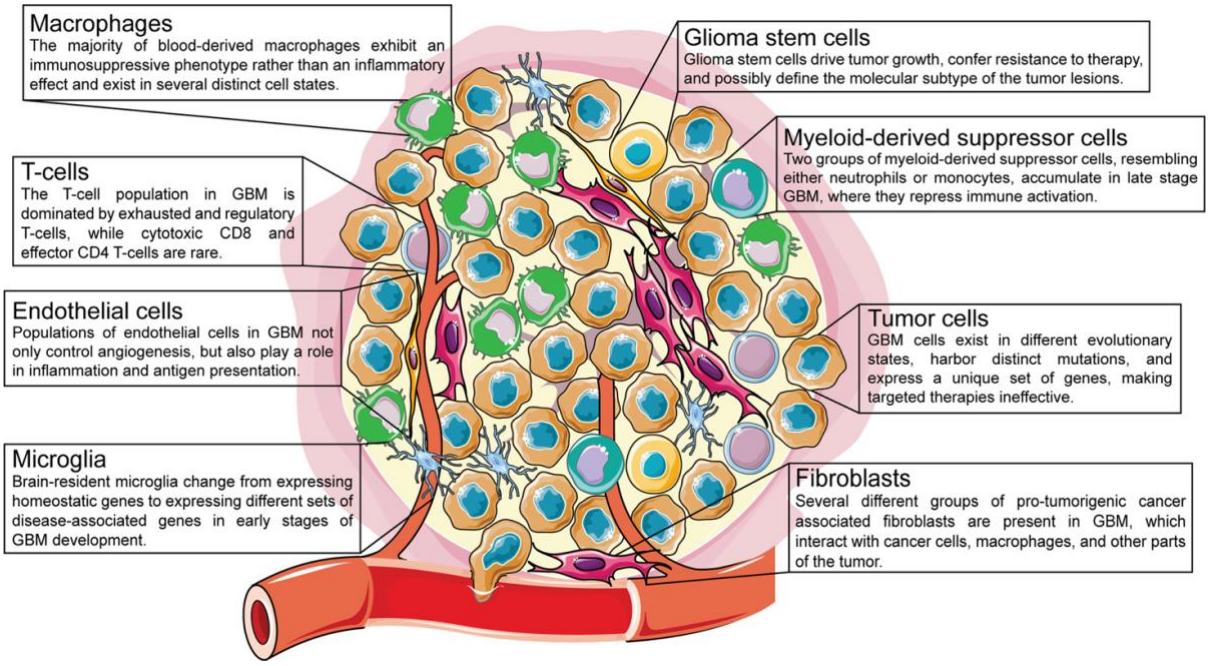

Figure 8 Histological diversity of the tumour cells within GBM.

It is the most common type of malignant brain tumour in adults. Specifically, it originates from a type of glial cell called astrocytes, which provide structural and metabolic support to neurons in the brain. GBM is characterized by the rapid and uncontrolled proliferation of these cells, leading to the formation of a mass or tumour in the brain. It is considered to be one of the most challenging forms of brain cancer to treat due to its highly invasive nature and resistance to traditional therapies. The prognosis for GBM is generally poor. Indeed, the survival rate is only 15 months, with

less than 5% of patients surviving beyond 5 years even with aggressive treatment [55]. Symptoms of GBM can vary depending on the location of the tumour, but common signs include headaches, confusion, weakness, difficulty speaking, coordination problems, seizures, and personality changes. These symptoms often result from the pressure exerted by the tumour on the surrounding brain tissue. The diagnosis typically involves a combination of imaging tests such as magnetic resonance imaging or computed tomography scans, and a biopsy to confirm the presence of the tumor. GBM is known for its high degree of aggressiveness. It grows rapidly and infiltrates the surrounding brain tissue, making complete surgical removal challenging. The treatment is complex and often involves a combination of surgery, radiation therapy, and chemotherapy. Due to its aggressive nature, GBM is challenging to treat, and long-term survival is often limited. Ongoing research aims to develop new and more effective treatments for GBM. This includes exploring targeted therapies, immunotherapies, and novel approaches to address the challenges posed by the aggressive nature of this tumour. One of the main treatment challenges is the blood-brain barrier (BBB), a natural barrier that separates the circulatory system from the brain and spinal cord. It consists of a specialized layer of endothelial cells lining the blood vessels in the brain. The primary function of the BBB is to regulate the entry of chemicals into the brain, allowing only selected molecules to pass through. In the context of treating glioblastoma multiforme (GBM) and other brain tumours, the presence of the BBB can significantly impact the administration of drugs and their effectiveness. It is designed to prevent harmful substances from entering the brain, and as a result, it hinders the effectiveness of some routes of administration. Some drugs are designed to cross the BBB, or they have been modified to do so. However, not all drugs have this capability, necessitating the development of specific therapies

for GBM treatment. To overcome the BBB, medical professionals may employ various strategies. For example, they may administer drugs directly into the tumour during surgery, use slow-release implantable devices in the brain, or use osmotic agents to temporarily open the BBB and allow drug passage. Nevertheless, when the BBB is temporarily opened to administer drugs, there can be side effects, as other unwanted substances may also enter the brain.

Scaffolds

Over the past decades, the development of biomaterials has advanced significantly leading to new ways of interacting directly with host tissue. They have evolved from inert materials that lack interaction with the body to biologically active, instructive materials that host and provide signals to surrounding cells and tissues [56–58]. One of the most promising approaches involves incorporating biologically active components into the material, which can then stimulate specific cellular responses. Nanomaterials can play a significant role in modifying cell behaviour by interacting with specific receptors present on the cell surface [9,59]. For instance, in a biomaterial intended to promote tissue regeneration, the biochemical factors should stimulate the process of cell proliferation and differentiation. Besides, the cells should be capable of regenerating the required tissue, and the scaffold should confer adequate mechanical properties. The scaffold is a tridimensional structure that should guide cell growth towards the reconstruction of tissues in terms of biological, functional, and morphological characteristics. It plays an essential role in tissue engineering providing a physiological-like microenvironment that allows perfusion of nutrients and

oxygen and transfers biochemical signals that influence cell phenotype and tissue formation [58]. Scaffold architectures, in Figure 9, play a pivotal role in dictating the success of a scaffold acting as the three-dimensional frameworks that guide cellular behavior and tissue regeneration[60].

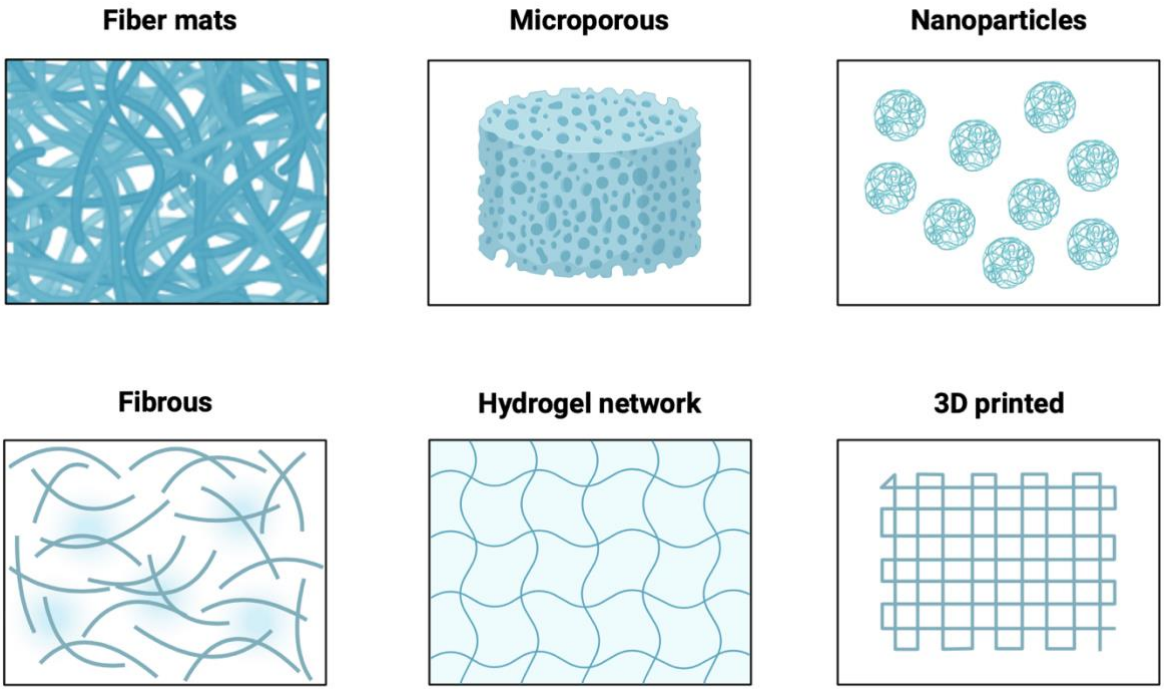

Figure 9 Scaffold Types for In Situ Tissue Regeneration

Its surface chemistry must be suitable for promoting adhesion, proliferation, differentiation, and incorporation of ECM. If biodegradable materials are used, the rate of degradation and reabsorption must be coordinated with the rate of tissue reconstruction. Whether natural or synthesized, the scaffolds are typically biodegradable, biocompatible and can be used to release drugs and growth factors while providing mechanical support. When selecting a new biomaterial, whether synthetic or natural, the demands of clinical applicability, such as easy to acquire and long-term storage should be taken into consideration [59]. Synthetic polymers can be

tailored on a molecular level to control degradation rate or modulate cell behaviour mimicking the ECM. They can also be blended with other polymers to fit any requirement that should be met to function as an integral part of the damaged tissue. The common materials for synthetic scaffolds are biodegradable polymers, such as polyvinyl alcohol (PVA), poly (lactic acid) (PLA), polyethylene oxide (PEO), poly (glycolic acid) (PGA), poly (ε-caprolactone) (PCL), polyethylene glycol (PEG) and polyurethane (PU) [12,61,62]. Scientists aim to develop more precise and efficient treatments for a broad range of medical conditions, using cutting-edge technologies to produce scaffolds. Several manufacturing techniques have been used to obtain tridimensional porous scaffolds:

- **Rapid prototyping:** this expression includes several manufacturing techniques used to quickly fabricate complex micro-architectures using computer-aided design (CAD) files.
- **Solvent casting and particulate leaching:** this technique uses different porogen agents, in different percentages, to modulate porosity and pore size.
- **Gas foaming:** gas, usually CO2, is inserted under pressure into the bulk polymer mould to generate high porosity.
- **Thermally-induced phase separation:** it can create porous structures with high interconnectivity and controllable pore size using a fast cooling of the solvent-polymer solution.

In recent years, this field has witnessed a paradigm shift in its approach towards regenerative medicine, with a growing emphasis on the design and fabrication of biomimetic scaffolds. Electrospinning (ES) has emerged as a key player in scaffold

fabrication, offering unprecedented control over the morphology and structure of nanofibrous matrices. This method harnesses the principles of electrostatic forces to produce ultrafine fibres, mimicking the natural extracellular matrix of tissues.

Electrospinning

ES is a versatile technique highly used to develop fibrous scaffolds, from polymeric solutions or melts, constituted by continuous fibres with diameters ranging from nanometers to sub-micrometers. It is widely used in research and industry due to its versatility, scalability, high area-to-volume ratio, and porosity. Therefore, it has potential applications in different fields like drug delivery and tissue engineering [63,64]. Since nanofibrous architecture highly favours cell binding and other cell behaviour activities, It was successfully employed in fabricating porous scaffolds of nano and microscale fibres that can replicate the structural and biological functions of the natural extracellular matrix [65,66]. The method involves electrostatic spraying of polymer to obtain porous scaffolds. An appropriate solvent is necessary for dissolving the polymer to be loaded into a syringe. The polymer solution is injected through a needle with a constant flow, and it is electrostatically charged. A conductive collector is placed at a proper distance from the tip of the needle. The shape of this collector depends on the desired outcome, and it can remain static, or it can have a rotational and/or translational movement during the deposition. Usually, the collector is negatively charged, and the needle is positively charged. When the electrostatic force created between the needle and the collector balances the surface tension of the polymer droplet, the pendant droplet forms a Taylor cone, and a fibre jet is

emitted from the apex of this cone. The electrified jet is attracted by the collector, and during the ejection and elongation process, the solvent evaporates, reducing fibre diameter until a dimension of micrometres or hundreds of nanometers. The fibres could be oriented to generate an anisotropic structure with a rotating mandrel. The rate of control of polymer flow can be adjusted by modifying the syringe flow rate from a syringe pump. A schematic representation of this technique is reported in Figure 10.

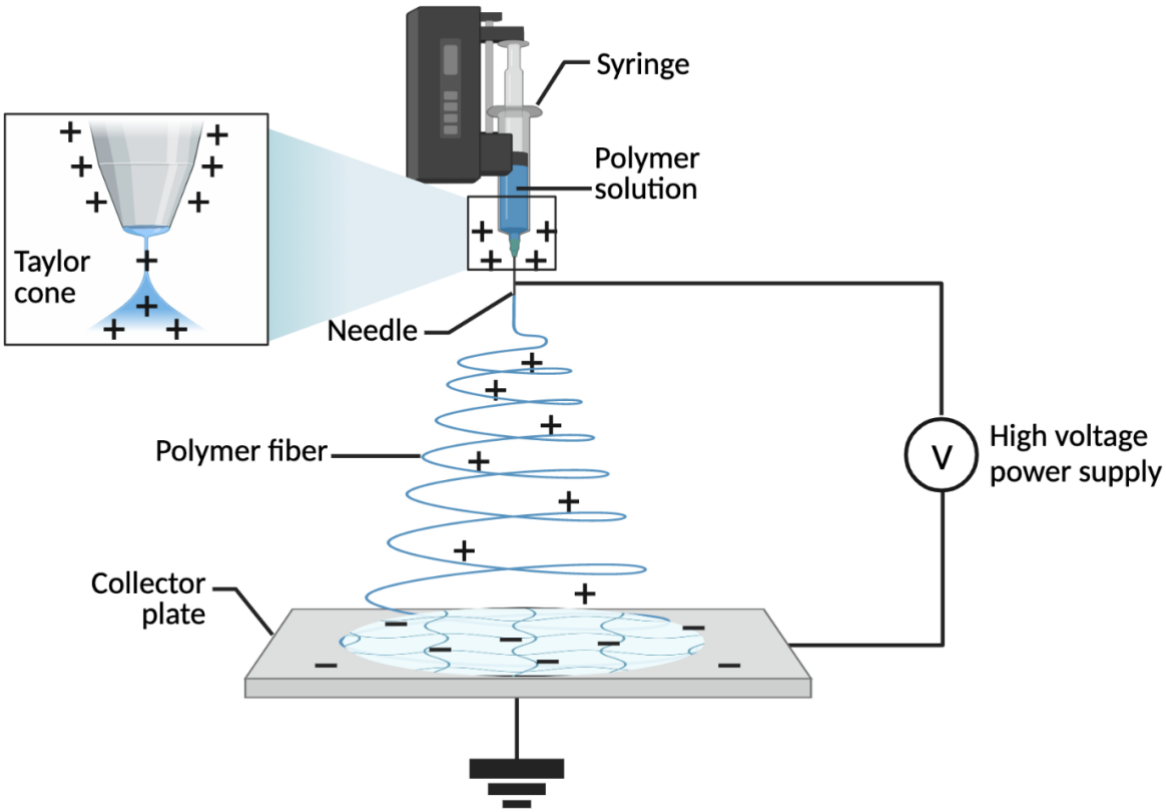

Figure 10 Schematic representation showing the electrospinning of the polymer nanofibers on a collector plate.

When fabricating scaffolds using the electrospinning method, it is essential to consider several key factors, such as:

- **Polymer concentration**: this parameter affects the spinnability of the solution by modifying the solution viscosity, and thus the fibre morphology. Different polymers have varying optimal concentrations required to produce smooth nanofibers. A lower concentration allows to obtain thinner fibres but leads to artefacts. Indeed, when the concentration is too low breakages occur and fibres become droplets before reaching the collector, so smooth fibres cannot be obtained. Higher concentrations minimize artifacts but also increase the fiber's diameters and high viscosity results in too hard injection. If the concentration of the solution is too low, it will result in electrospray instead of electrospinning.
- **Surface tension**: depends on the solvent of the solution, so different solvents lead to different surface tensions. Reducing surface tension while fixing polymer concentration can improve the result by converting some bead fibres into smooth fibres.
- **Voltage**: the difference in electric charge between the capillary needle and the collector can modify fibre diameters. Usually, the needle is positively charged, and the collector is kept at ground or negative potential. If the difference is too low some drops of the polymer can fall instead of being spinned to the target. If the difference is too high spikes will appear on the outer surface of the graft.
- **Flow rate**: when the flow rate is too high beads formation is observed due to the short time-lapse for solvent evaporation, hence the fibres are not completely dry before reaching the collector.

- **Distance**: the space between the collector and syringe tip influences the time-lapse for solvent evaporation before depositing on the collector. A long distance could lead to the deposition of bead fibres while a too short distance could lead to wet fibres.
- **Molecular weight**: too low-molecular-weight polymer solutions tend to generate beads instead of fibres, while very high-molecular polymer solutions produce fibres with a high average diameter.

Other parameters influencing the final product are solvent volatility, conductivity, temperature, and humidity. The primary benefit of this technique is its ability to produce fibres of similar dimensions to ECM fibres, thereby facilitating cell adhesion. However, the main challenge associated with this technique is its reproducibility since there are several variables involved, and some of them can be difficult to control. ES could be combined with other manufacturing techniques such as solvent casting and thermally induced phase separation to obtain complicated porous microstructures with hierarchical pore sizes. Over the past decades, several attempts have been made to prepare biodegradable polymeric materials with appropriate pore networks for different applications, like ES, thermally induced phase separation, rapid prototyping, and particulate leaching [9,56,61,67].

The ability to engineer scaffold architectures with precision at the nanoscale opens new avenues for tailoring the mechanical, structural, and biological properties of the resulting scaffolds. These architectures, characterized by their intricate network of nanofibers, provide a biomimetic environment that closely resembles the natural extracellular matrix. The rational design of scaffold architectures influences cellular adhesion, proliferation, and differentiation, essential processes for successful tissue

regeneration, opening up various potential applications in tissue engineering scenarios.

Electrospun scaffolds in tissue engineering

The failure of a tissue is one of the most frequent, devastating, and costly problems in human health care [59,68,69]. Tissue engineering is the branch of engineering that applies scientific principles for the design, growth, and maintenance of living tissues. It was born in the late 1900s to offer a valid alternative to traditional organ transplant or prosthesis techniques aimed at restoring the physiological functions of a particular tissue. The goal is to reproduce in vitro a tissue with structure and functions as similar as possible to physiological tissue. It therefore involves, in addition to traditional mathematical and scientific applications, the use of cells, biomaterials and bioactive molecules to promote tissue formation and integration in the host environment. To promote the desired regenerative process, the biochemical factors should stimulate proliferation and differentiation; cells should provide the appropriate tissue regeneration; scaffolds should confer sufficient mechanical properties (Figure 11).

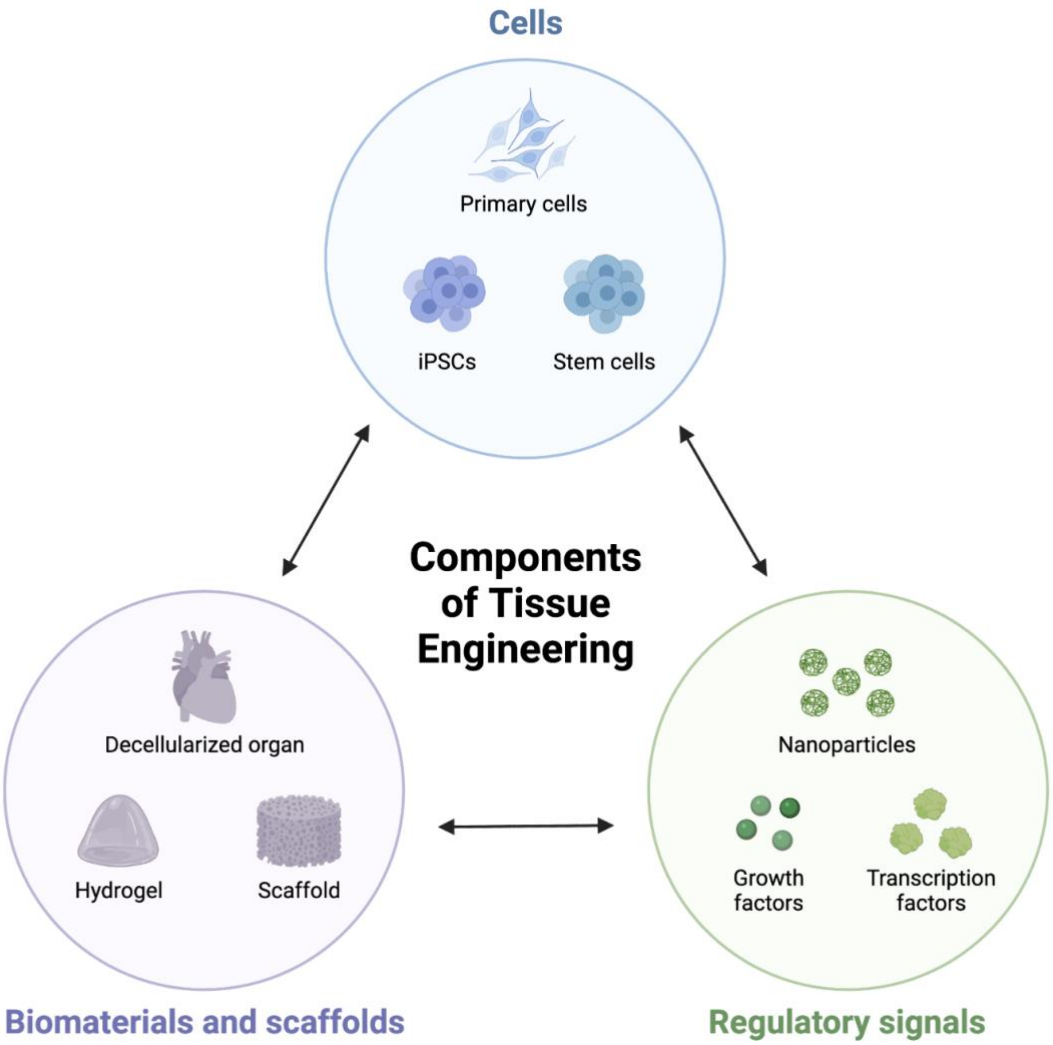

Figure 11 Components of Tissue Engineering.

Several polymers either natural (e.g., collagen, silk fibroin, chitosan, alginate) or synthesized (e.g., PU, PCL, PLA, PGS) were successfully employed in fabricating porous scaffolds by electrospinning [65,70,71]. Although several electrospun conduits have been studied for different tissue engineering applications, none of them is currently used for small-diameter conduits. Currently, used prosthetic grafts (ePTFE, Teflon® or PET, Dacron®) are satisfactory in large-diameter applications, but they fail to demonstrate long-term patency comparable to that of autologous grafts in small-diameter (<6 mm) settings due to their susceptibility to inflammation, thrombosis,

intimal hyperplasia, and consequent compliance mismatch with the host vessels [2]. Furthermore, clinical demand for tubular scaffolds is not limited to vascular grafts. The global burden of cardiovascular diseases is on the rise and is projected to affect 50% of Americans by 2030 [68]. The use of an artificial bile duct instead of choledochojejunostomy, which is the standard technique for biliary reconstruction, could maintain a physiological conduit for bile. Moreover, there are other needs for tubular conduct substitutes like peripherical limb revascularization, arteriovenous fistulae for haemodialysis and peripherical nerve regeneration. In recent years, for these reasons, several research groups have been studying other tubular scaffolds [72,73]. These grafts should be permanently implanted to restore the effectiveness of a tract that is no longer able to correctly transport the fluids. Designing requirements are hemocompatibility, elasticity, avoiding leakage, compatibility with the standard sutures, mechanical resistance, sterilizability, reliability and with the appropriate length and diameter. Furthermore, they must provide initial mechanical support and functionality, then are supposed to degrade and be replaced by the cells. Their properties and degradation profile could be controlled during the manufacturing process to provide the best outcomes for ECM synthesis and tissue regeneration.

Poly(1,4-butylene succinate) (PolyBS) as an electrospun polymeric tubular scaffold for tissue engineering applications

PolyBS is a commercially available, biodegradable, thermoplastic aliphatic polyester, synthesized by the polycondensation of succinic acid and butanediol (Figure 12).

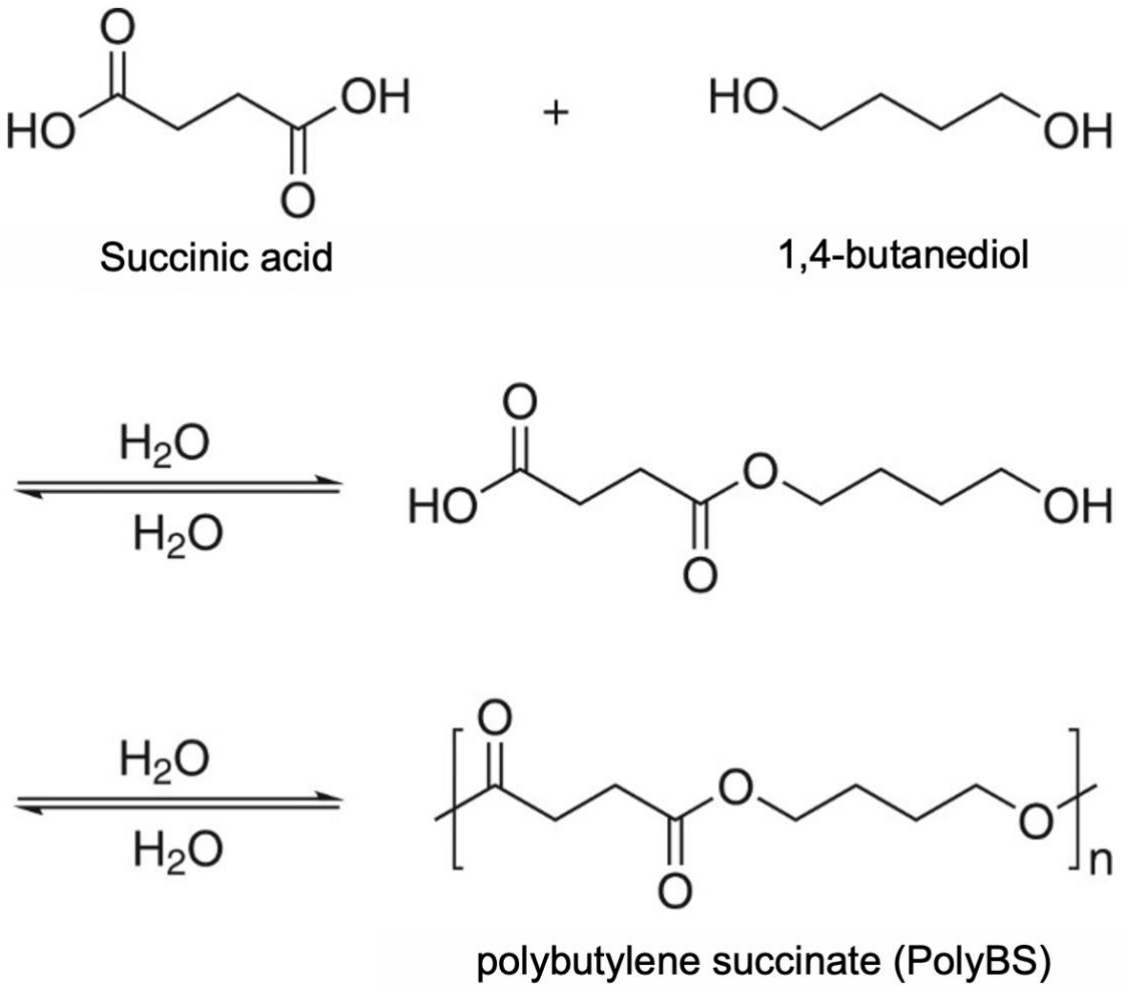

Figure 12 Polycondensation of succinic acid and butanediol.

These monomers can be either derived from fossil fuels or renewable resources and currently commercially available PolyBS is synthesized from chemically derived monomers. Butanediol (BDO) can be derived from glucose using a total biosynthetic

route. Succinic acid is an important intermediate of the TCA cycle and is produced by several microorganisms as a fermentation product under anaerobic conditions. Therefore, complete bio-based PolyBS can be produced at an industrial scale [74]. PolyBS is insoluble in water, its melting temperature is 120 °C and the glass transition temperature is below 0 °C. It can be sterilized with several techniques without compromising the scaffold's properties. Lastly, it has excellent processability and proven biocompatibility making it a promising polymer for various biomedical applications [75–79]. Cicero et al. used PolyBS as a planar microfibrillar scaffold implanted as a conduit, in a rat model, to preserve nerve continuity and promote its regeneration. They observed biodegradability from high-resolution MRI investigation showing complete reabsorption in 120 days post-implant [80]. Almeida et al. produced and characterized anisotropic planar scaffolds through weft knitting, demonstrating that PolyBS is a promising material for tissue engineering applications due to the high level of processing control and because it supports cell adhesion and proliferation [81]. Di Prima et al. chose PolyBS as a polymeric ocular insert due to its manageability in the electrospinning process and hydrophobicity. They modified the electrospun scaffold surface via plasma-induced chemical functionalization to improve biomimetic and mucoadhesive properties [82].

The mechanical properties are strictly dependent on the presence of diisocyanates used as chain extenders. High molecular weight PolyBS synthesized without chain extenders shows a brittle behaviour, with very short elongation at break, while the use of isocyanates significantly improves its elongation [83]. Hence, PolyBS extended with 1,6-diisocyanatohexane emerges as a promising choice for applications in dynamic environments. This formulation exhibits the capacity to endure and rebound from short-term deformation, rendering it well-suited for scenarios that demand

resilience and adaptability. The robust characteristics of this extended PolyBS make it particularly suitable for use in settings where dynamic conditions, such as mechanical deformation, are prevalent and necessitate a material that can sustain and recover effectively.

The material's capability to sustain and recover from deformation makes it promising for use in vascular grafts, where flexibility and resilience are crucial for optimal blood flow. The dynamic nature of the extended PolyBS makes it well-suited for applications in artificial bile ducts, where it can adapt to the variable conditions of the digestive system. The material's resilience is advantageous for peripheral limb revascularization, supporting blood circulation and recovery in damaged or compromised peripheral arteries. The extended PolyBS can potentially be utilized in the creation of arteriovenous fistulae for hemodialysis, benefiting from its ability to withstand mechanical stresses associated with blood circulation. In the realm of regenerative medicine, the material may find applications for peripheral nerve regeneration, providing a supportive and adaptable environment for nerve repair and growth.

2. Aim

In the quest to understand and optimize polymers, this PhD thesis embarks on a comprehensive exploration of the principles governing the behaviour, synthesis, processing, and application of polymers. This work delves into the intricate science underpinning polymer chemistry and physics, investigating the relationships between molecular architecture and macroscopic properties. Furthermore, it investigates different methodologies for polymer processing, as well as their applications as biomaterials. The overarching objective of this thesis is organized into two main chapters, each centred around a specific polymer and its applications. The initial section delves into the exploration of biodegradable segmented polyurethane urea synthesized, characterized, and processed with a focus on its potential as a biomaterial.

- *The synthesis, characterization, and processing of highly bioadhesive polyurethane urea as a microfibrous scaffold inspired by mussels* [84]

The primary objective of this study is to synthesize and characterize versatile polyurethane urea through a biomimetic approach. This innovative material incorporates a dopamine-containing chain extender, imparting it with the ability to exhibit strong adhesion in response to specific stimuli. Additionally, the research seeks to establish the biocompatibility and processability of this biomaterial, affirming its potential as a valuable biomaterial for various applications.

- *Overcoming the Blood-Brain Barrier: A Novel Approach Using a Conductive Bioadhesive Coating for Voltage-driven Drug Delivery in Glioblastoma Multiforme*

Glioblastoma multiforme stands out as the most prevalent form of malignant brain tumour among adults, marked by a disheartening 15-month median survival rate, and less than 5% of patients managing to survive beyond 5 years. A pivotal obstacle in treating this aggressive condition is the blood-brain barrier (BBB), which regulates the entry of chemicals into the brain. To address this challenge, this study endeavours to pioneer the development of a conductive bioadhesive coating. This innovative coating is designed to be strategically inserted into the intricate microenvironment of the tumour, facilitating the delivery of drugs by circumventing the impeding effects of the BBB when a controlled voltage is applied. Furthermore, our investigation seeks to delve into the intricate relationship between the applied voltage and the efficacy of the delivered drug, unravelling crucial insights into optimizing tumour treatment strategies.

The second section shifts its focus to an electrospun scaffold crafted from PolyBS, specifically tailored for applications in tissue engineering. Here, the emphasis lies in optimizing the scaffold's morphology to create a conduit with interconnected micro-porosity, fostering cell integration, adhesion, and growth while preventing undesired cellular infiltration through the graft's wall.

- *The processing and evaluation as a microfibrous graft for tissue engineering applications of polybutylene succinate* [85]

The objective of this study is to refine the processing of polybutylene succinate using electrospinning, to fabricate a microfibrous graft tailored for tissue engineering applications. The envisioned graft must maintain its structural integrity and properties following short-term mechanical conditioning, while also being suture-compatible. Simultaneously, it should facilitate the physiological exchange of metabolites and catabolites, all while preventing undesirable cell infiltration through the graft wall.

Moreover, the scaffold's structural design is meticulously crafted to emulate the composition of the extracellular matrix (ECM), aiming to foster optimal cell growth and minimize the risk of hemolysis.

- *An in vivo evaluation of its biocompatibility and potential to act as a scaffold for bone regeneration* [86]

The in vivo experimental study was designed to elucidate the biocompatibility and biodegradability characteristics of the scaffold. Furthermore, it aims to demonstrate that the administration of a microfibrillar scaffold made of PolyBS constitutes a highly effective strategy for promoting accelerated bone regeneration, particularly in situations involving critical bone defects.

As we embark on this academic journey into the realm of polymers, we are reminded of the countless opportunities and challenges that lie ahead.

3. Results and Discussion

3.1 Synthesis, characterization, and processing of highly bioadhesive polyurethane urea as a microfibrous scaffold inspired by mussels

Summary

There is a growing demand for robust adhesive scaffolds that can be processed to establish favourable micro-environments, guiding cellular behaviours and promoting tissue regeneration. Bioadhesive coatings emerge as pivotal elements in enhancing the performance and functionality of inorganic implantable materials. They play a crucial role by fostering tissue adhesion, minimizing implant-related complications, and enhancing long-term biocompatibility. This emphasis on bioadhesive properties represents a significant stride in the development of processable advanced biomaterials, aiming to optimize their interaction with biological systems for improved clinical outcomes.

Synthesis and characterization of PU-LDA

The triblock copolymer PCL-PEG-PCL was synthesized, by ring-opening polymerization, from ε-CL and PEG with a yield above 95% as reported in literature [87]. Both are widely used for biomedical applications due to their excellent biocompatibility [12,13,88,89]. Furthermore, PEG has a low melting temperature (T_m~ 38°C) and we have chosen the molar ratio between them consequently to achieve a

melting temperature of around 55°C. The ^{1}H-NMR spectra, reported in Figure 13, showed the characteristic peaks of methylene protons of PCL block, labelled as *a*, *b*, *c* and d at 1.4, 1.7, 2.3 and 4.3 ppm respectively, while the ethylene oxide protons of PEG labelled as *e* were displayed at 3.7 ppm.

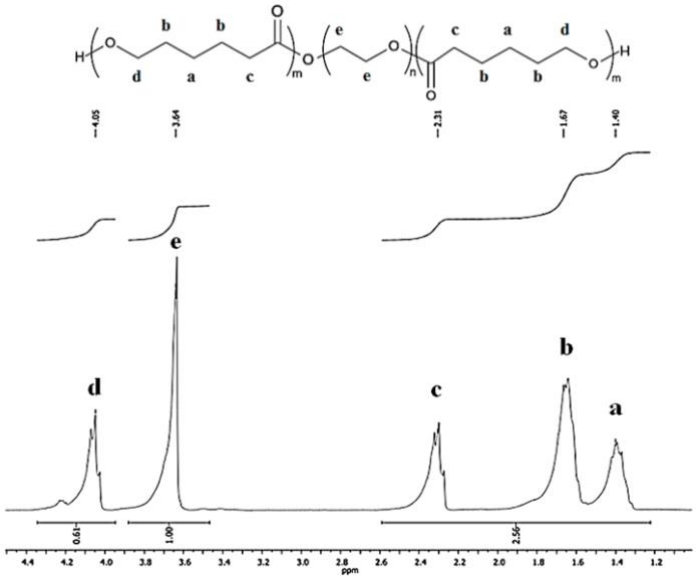

Figure 13 ^{1}H-NMR of PCL-PEG-PCL labelling the characteristic peaks of methylene protons of PCL block, as a, b, c *and d.*

The sum of all the PCL peaks contributions is 3.17 times higher than the PEG peak and since the PCL peaks are due to 10 protons and PEG to 91 the resulting molar ratio is 29. The macromolecular weight (Mn ~ 4300) and PEG/PCL block ratios estimated from the ^{1}H-NMR spectrum were consistent with the theoretical value calculated from the feed ratio.

Lysine-dopamine LDA was synthesized from L-Lysine HCl and dopamine-HCl as reported in literature [23]. The structures of LDA and intermediate products, $(Boc)_2$-lysine-OH (BL), $(Boc)_2$-lysine-NHS (BLN), $(Boc)_2$-lysine-dopamine (BLDA), lysine-

dopamine (LDA), were confirmed by FTIR, ^{1}H-NMR and UV-vis spectroscopy (Figure 14-a).

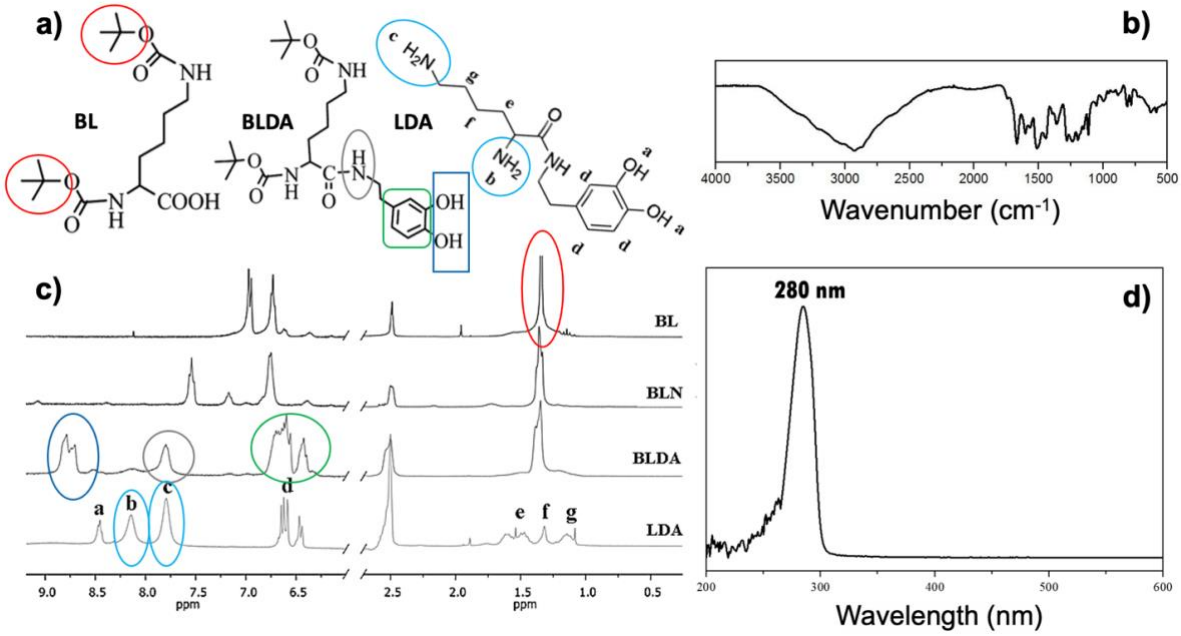

Figure 14 a) schematic of LDA molecule and intermediate products, b) FT-IR analysis of LDA, c) ^{1}H-NMR of the intermediate products and LDA, d) UV-vis spectrum of LDA.

In the ^{1}H-NMR spectra (Figure 14-c), for BL, the peaks at 6.98 ppm and 6.78 ppm, corresponding to protons on the –CH(COOH)–**NH**-Boc and –CH_2–**NH**-Boc respectively. The peak at 1.36 ppm relative to the 18 protons of the two ammine protecting groups –O–C(**CH_3**)$_3$ implies the successful protection of ammine groups. Compared with BL, new peaks in BLDA at 8.60–8.90 ppm correspond to protons on –Ar(–**OH**)$_2$. The peak at 7.76 ppm is relative to –CO–**NH**–CH_2 and peaks at 6.60–6.30 ppm correspond to the 3 protons of CH inside the phenyl ring of dopamine that implies the successful amidation reaction. Compared with BLDA, there was no peak at 1.36 ppm in LDA, indicating successful deprotection of amine groups. In the UV-vis spectrum of LDA (Figure 14-d), there is an absorbance peak for the catechol

group at 280 nm, which confirms the conjugation of dopamine with lysine. The synthesized LDA is a functional biomolecule containing a mussel-derived adhesive moiety (catechol) and a bio-functional moiety (lysine). Moreover, the primary amine groups of lysine residue have particularly high reactivity with the isocyanate group to act as a chain extender on polyurethane urea's synthesis.

LDA was utilized to obtain PU-LDA, allowing the chain extension, and lysine was used for PU-LYS as the control group for comparison (Figure 15-a).

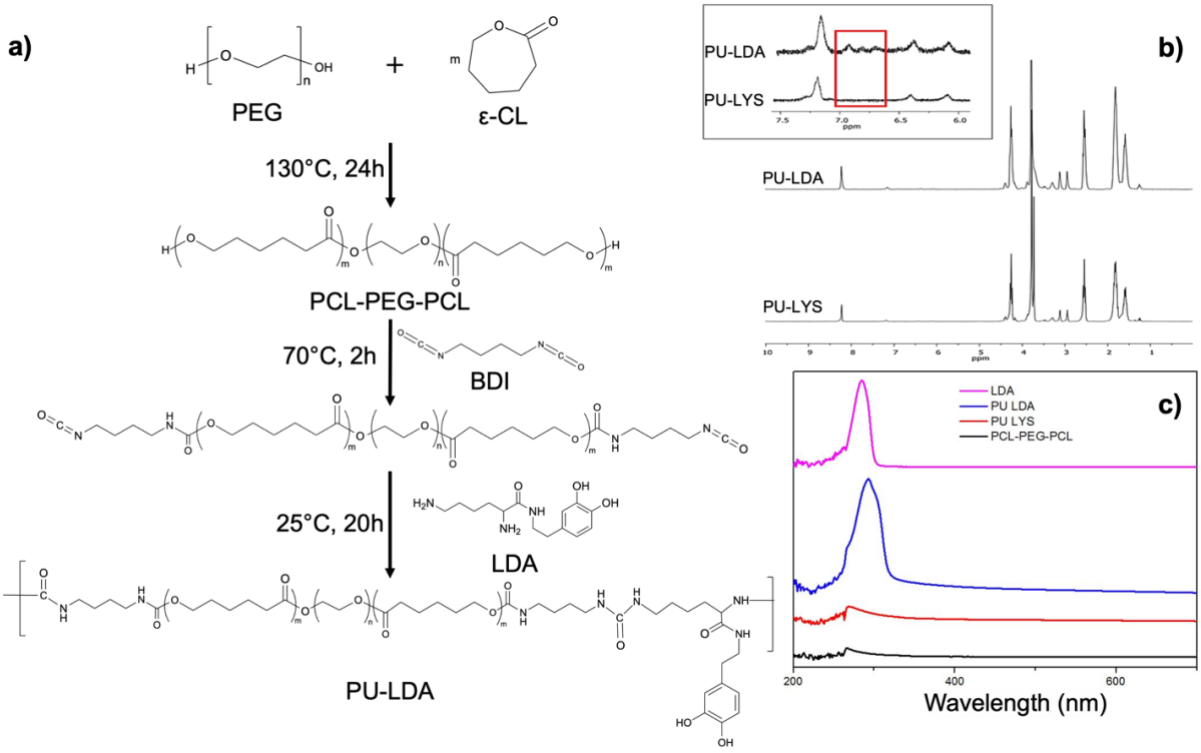

Figure 15 a) Scheme of PU-LDA synthesis, b) ^{1}H-NMR comparison between PU-LDA and PU-LYS, c) UV-vis comparison between synthesized products.

PU-LDA and PU-LYS were synthesized using triblock copolymer PCL-PEG-PCL as a soft segment and 1,4-diisocyanatobutane as a hard segment. Indeed, their ^{1}H-NMR spectra (Figure 15-b) showed the same characteristic peaks of PCL-PEG-PCL between 1.4 and 4.3 ppm. Comparing PU-LDA and PU-LYS spectra it is possible to

highlight the presence of peaks between 6.65 and 7.00 ppm attributable to the 3 protons of aromatic CH. In the UV-vis spectrum of LDA (Figure 15-c), there is an absorbance peak for the catechol group at 280 nm, which confirms the conjugation of dopamine with lysine for the chain extender. This peak is present also in PU-LDA confirming the presence of dopamine in the polyurethane. This information, combined with the previous ones obtained from FTIR, ^{1}H-NMR and SEC confirms the success of the reported synthesis reactions. The amount of LDA bounded to the PU-LDA was quantified through UV and is equal to 5.5% (w/w).

Biodegradable polyurethanes are an exciting class of synthetic polymers widely used as biomaterials and many of today's commercially successful PUs include alternating block copolymers like the synthetized PCL-PEG-PCL. However, PUs that are synthesized from only polyols and diisocyanates often have poor mechanical properties [90]. Therefore, the synthesized LDA was used as a chain extender to promote phase separation between the incompatible hard and soft segments while incorporating a pendant functional biomolecule, dopamine, containing a mussel-derived adhesive moiety [28]. The result is a solid and processable biomaterial that can express adhesion after melting.

Size Exclusion Chromatography (SEC) analyses, reported in Table 1, showed that Mw increased significantly from PCL-PEG-PCL (5.7kDa) to PU-LYS (45.1kDa) and PU-LDA (51.6kDa).

Table 1 Molecular weight evaluation from SEC analysis (Mn, Mw and PDI) and Mn of PCL-PEG-PCL from ^{1}H-NMR.

	M_n ^{1}H-NMR	M_n	MW	PDI
PCL-PEG-PCL	4300	5600	5700	1,1
PU-LDA	/	41900	51600	1,2
PU-LYS	/	23700	45100	1,9

This result demonstrates the successful polymerization process and is coherent with the previous results [87]. In the analysis of Fourier transform infrared of the derivatives (Figure 16) bands at 3434 and 1527 cm^{-1} were the stretching, and deformation vibration of -NH- groups of urethanes and urea groups and to C–N stretching, the carbonyl stretching vibration was at 1720 cm^{-1}.

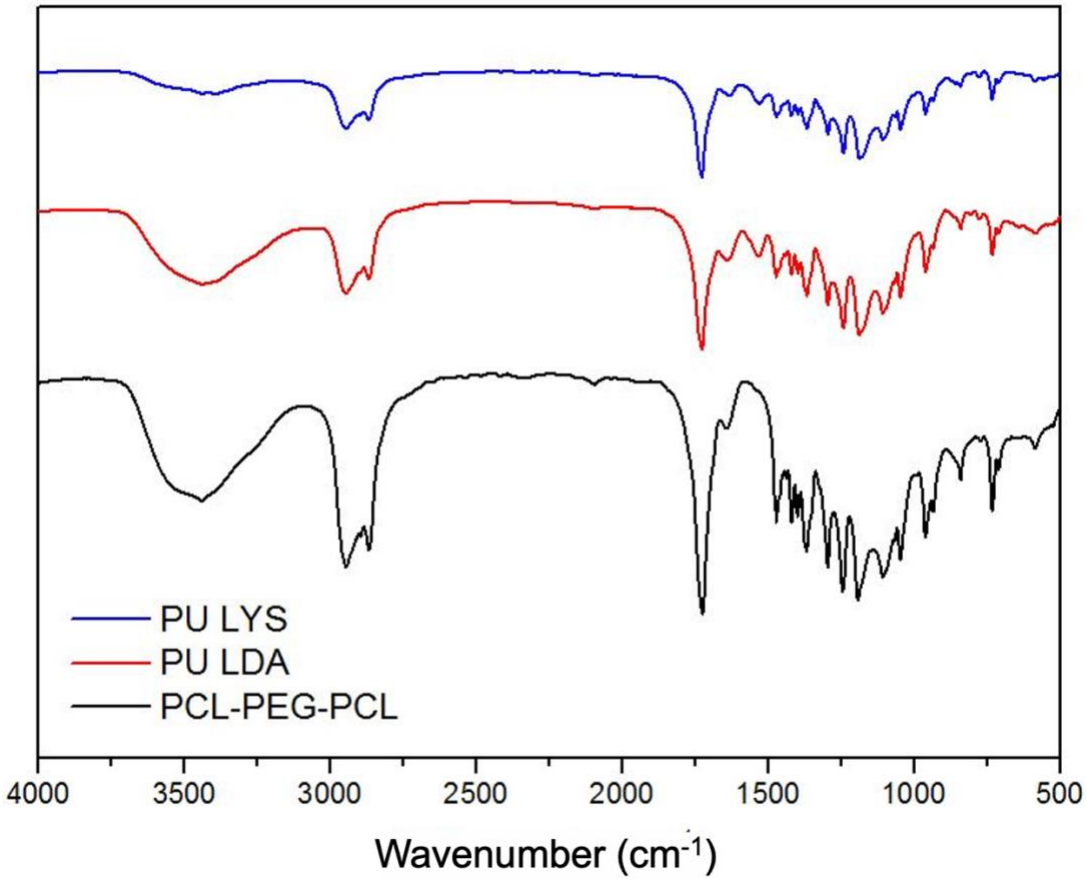

Figure 16 FTIR comparison between synthesized polyurethanes and the triblock copolymer.

The appearance of a band at 1603 cm^{-1} in PU-LYS and PU-LDA confirmed the occurrence of ammine bonds implying the successful polymerization process. The peaks at 1237 and 1162 cm^{-1} could be attributed to the asymmetrical stretching vibration of the N–C–O and CO–O groups. The peaks at 1101 cm^{-1} were interpreted as asymmetric stretching vibration of the O–C–C band in PCL blocks.

The thermal behaviour of selected polyurethanes was studied by TG-DSC analyses (Figure 17-a).

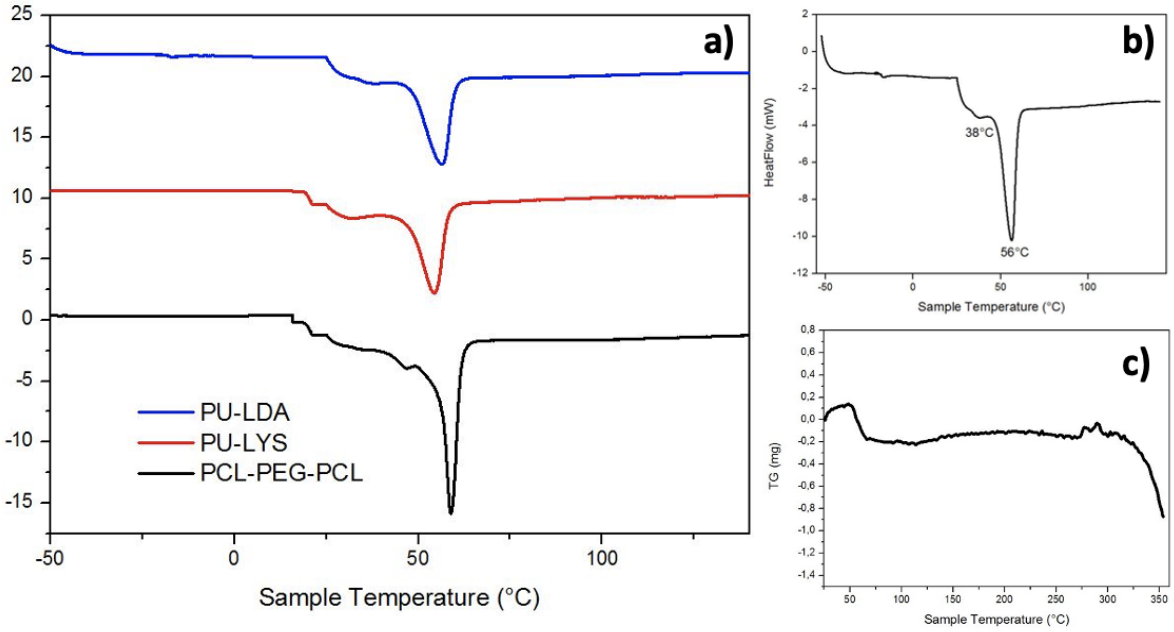

Figure 17 a) DSC comparison between synthesized polyurethanes and the triblock copolymer, b) DSC details of PU-LDA, c) Thermal degradation of PU-LDA.

Figure 17-b clearly shows two different melting temperatures of polyurethanes. The first one at 38°C is correlated to the PEG block and the other at 56°C is due to the PCL. A glass transition temperature (T_g) was observed at -17°C. The PU-LDA exhibited soft segment transitions over the temperature range of -50 to +150 °C and the absence of a hard segment transition agreed with results detected for similar Pus [87]. Figure 17-c highlights the absence of degradation <325°C which allows melting of the material to process it. To characterize properties of the polymer like degradation rate, cytocompatibility, adhesiveness after melting and viscosity, the polyurethanes were processed as films by film casting procedure. Hydrolytic degradation was measured in sodium azide/DPBS at 37 °C over six months. The results reported in Table 2 showed that the amount of mass lost is always <4% which is consistent with previous studies since PCL degrades very slowly [91].

Table 2 Residual mass (Rm) % after hydrolytic degradation of PU-LDA over 6 months.

Time (weeks)	0.7	1.4	3	5	9	13	17	21	25
R_m (%) PU-LDA	98±0.7	99±1	98±0.5	98±0.5	97±0.5	96±3	99±2	96±1	97±1

This result underlines the synthesised PU's remarkable hydrolytic resistance, which is a fundamental design requirement for tissue-engineered scaffolds to maintain structure and function over time.

The swelling analysis didn't show significant differences between the PUUs for each time point up to 14 days (Table 3). The slightly higher swelling values for PU-LYS could be attributable to the free carboxyl group that can interact with water [92].

Table 3 The swelling ability of the PUUs films tested after incubation in DPBS pH 7.4 for up to 14 days at 37°C.

Swelling (%)	1g	7g	14g
PU-LDA	18.4±0.9	18.3±1.2	18.4±1.2
PU-LYS	17.6±1.2	20.5±0.8	20.1±1.1

The water contact angle of the films (Figure 18) started at 61° for PU-LDA and 71° for PU-LYS and both decreased to 37° and 53° respectively.

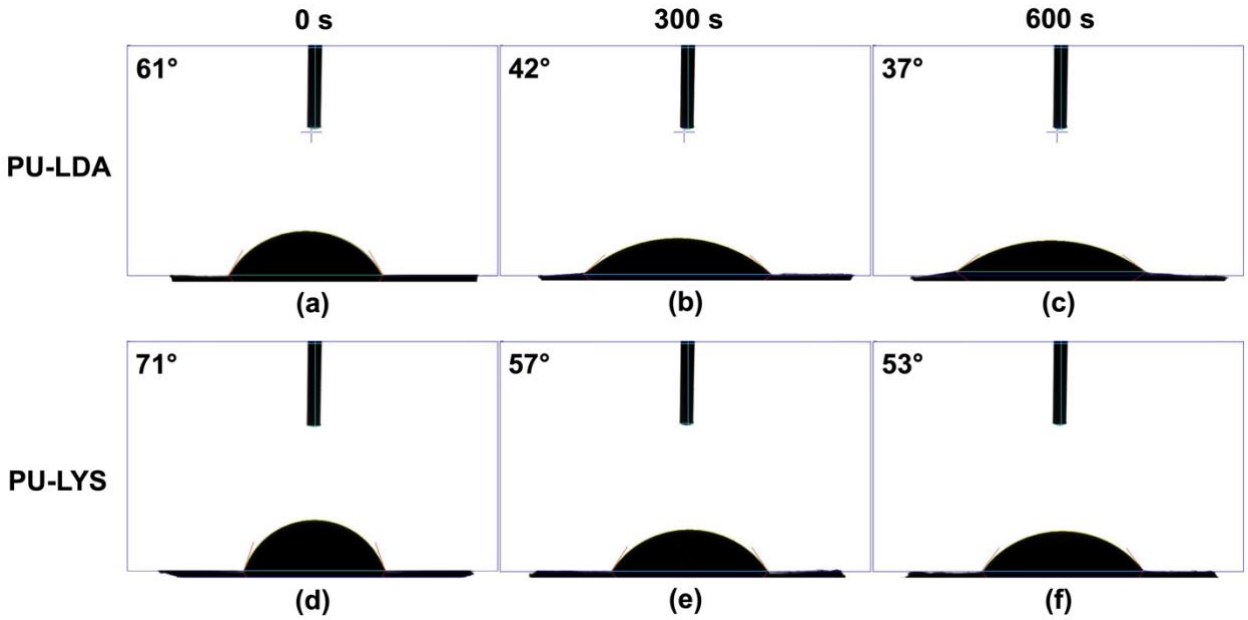

Figure 18 Determination of the contact angle on PU-LDA (a, b, c) and PU-LYS (d, e, f) films: images acquired after 0, 300 and 600 seconds.

The small difference between the two polymers can be attributable to the presence of the catechol group that increases hydrophilicity. Hydrophilic polymers perform better as bioadhesives because they can form strong bonds with highly hydrophilic tissues [14].

In vitro cytocompatibility studies

Cell viability of NHDF in the presence of PUs disks was assessed by an MTS assay for up to 7 days. The results showed no significant difference between the polyurethane and the viability was >96% at each time point. Therefore, we can assume the absence of cytotoxic degradation products for both PUU derivatives (Figure 19-a).

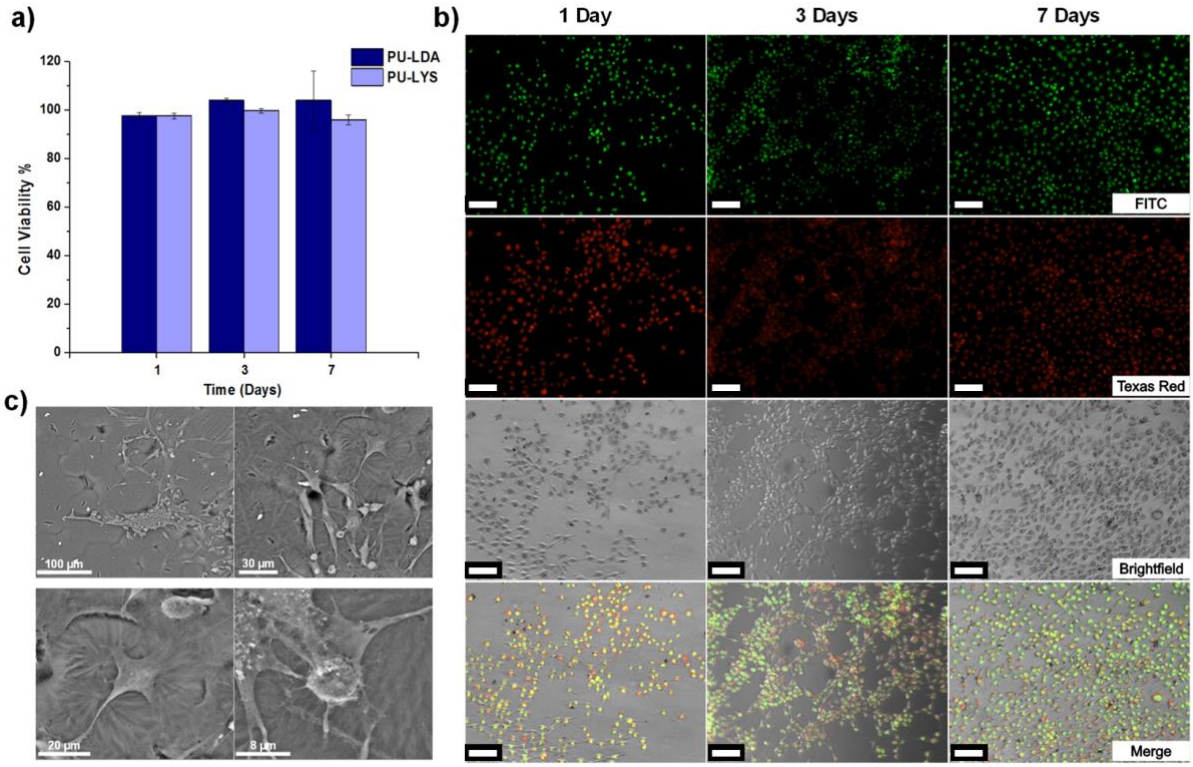

Figure 19 a) Indirect viability comparison between PU-LDA and PU-LYS; b) Fluorescence images of NHDF cells stained with acridine orange/ethidium bromide (AO/EB) double staining after 1, 3 and 7 days of culture with PU-LDA films (indirect cells viability) 100 µm scale bar; c) SEM images of cells growing in direct contact with PU-LDA films after 7 days of culture.

This data was also confirmed by Acridine orange/ethidium bromide (AO/EB) double staining. According to fluorescence emission is possible to distinguish viable cells from apoptotic and necrotic cells. Indeed, acridine orange is taken up by both viable and non-viable cells emitting green and red fluorescence if intercalated with double-stranded nucleic acid (DNA) and single-stranded nucleic acid (RNA) respectively. Instead, ethidium bromide is taken up only by non-viable cells and emits red fluorescence through intercalation within the DNA. Viable cells appear with a uniform bright green nucleus and orange cytoplasm. Even early apoptotic cells have green nuclei but, in this case, it is possible to note a perinuclear chromatin condensation as bright green fragments. Orange to red nuclei with condensed or fragmented chromatin is visible to late apoptotic cells while necrotic cells have uniformly orange to red nuclei with organized structure [93]. As shown in Figure 19-b most cells were viable for up to 7 days and no significant apoptosis was detected with only a few dead cells found.

The cytocompatibility was further confirmed by direct culture of cells on PU-LDA films. SEM images (Figure 19-c) showed that cultured fibroblasts maintain the typical shape and morphology after 7 days of culture, showing elongation and complete integration within the PUU matrix. This preliminary data conceivably suggests the optimal cytocompatibility of synthesized polymer and the cell-adhesive properties of PU-LDA films.

Adhesion evaluation

The adhesive behaviour of PU-LDA was preliminary assessed by tack test analysis and results are reported in Figure 20-a-b.

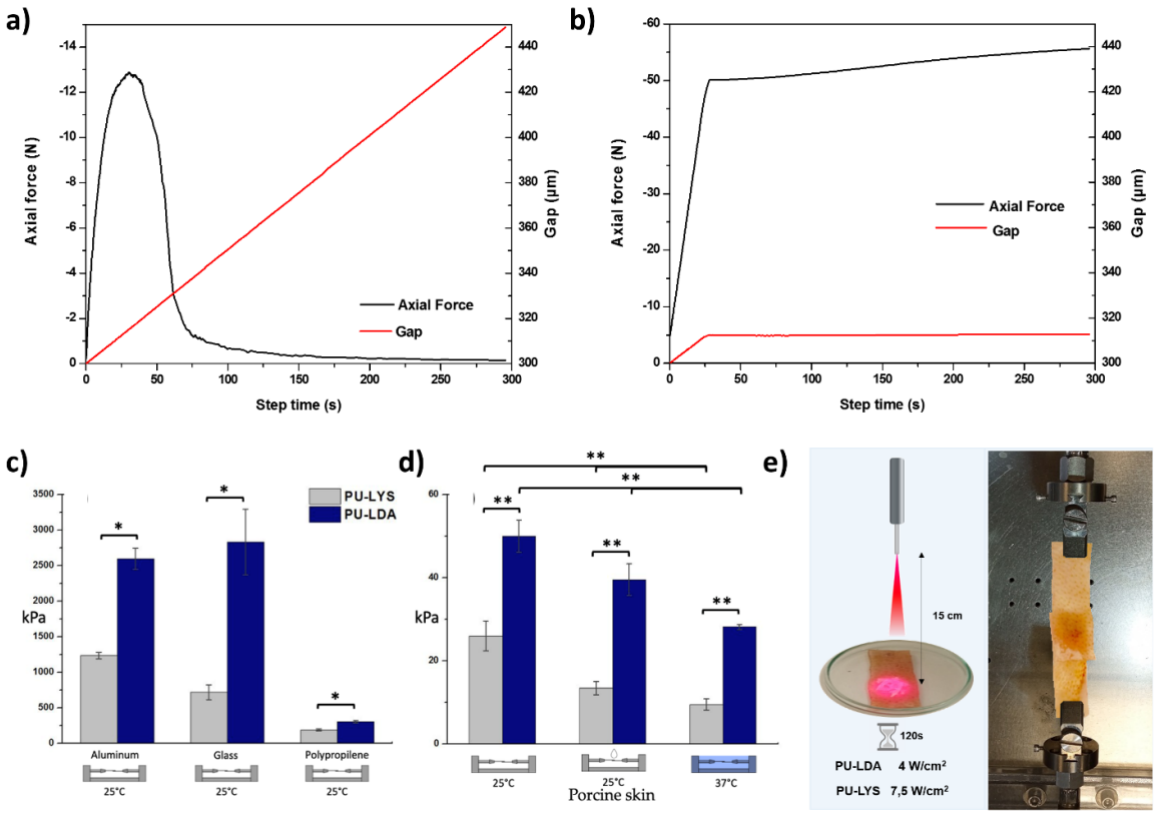

Figure 20 Force (N) versus time curves of PU-LDA film obtained in Tack test at 37°C (a) and 25°C (b); c) Lap shear results at room temperature and dry conditions, T-test (2:2) P<0.001, d) Lap shear results on porcine skin adherents respectively at 25°C and dry conditions (left), 25°C and wet conditions (middle), 37°C submerged in water, Two-way ANOVA P<0.001; e) Phases of the lap shear test: NIR induced film fusion by laser NIR irradiation for 120 s; adhesion of the two specimen of skin; immersion in DPBS; evaluation of the lap-shear adhesive strength by Bose TA Instruments ElectroForce Test Bench System.

The tackiness of materials, which depends on the cohesive forces between the adhesive itself and the substrate, is associated with stickiness and may result from

adhesive or cohesive forces between two materials in contact or a material bridging two substrates. The tack is then recorded as the maximum force required to break the resultant bond, describing the tendency of materials to form a connection to a substrate. Here, PU-LDA film was subjected to a tack test to measure its adhesive properties as a function of temperature recording the minimum force and the tackiness of the material expressed as the area under the force-time curve.

The gap (red line) and axial force (black line) profile for PU-LDA are shown in Figure 20-a-b. These graphics show a reduction in compressive force with a residual tensile (negative) force, corresponding with tack and adhesion of the material, at 37 °C (Figure 20-a) or 25 °C (Figure 20-b) after the gap (µm) was raised linearly at 0.5 µm/s.

When the experiments were performed at 37 °C the time failure, which corresponds to the time for the force to decay by 90% of peak values (13 N), was 75 seconds. This preliminary result demonstrated that the adhesive potential of PU-LDA can be exploited only once the polymer is melted in contact with the specific surface. Once it is fused the molecular interactions between the adhesive and the material can occur, then when the material is cooled under the melting point the adhesive interactions can be exploited. At 25 °C the force reached higher values with no failure observed and gap constant at 317 µm. Cooling down the material from 37 to 25 °C caused an increment of adhesion of the sample. This qualitative analysis suggests that PU-LDA film can exploit its adhesiveness after low-temperature melting (55 °C) and cooling at 37 °C and 25 °C.

The quantitative evaluation of bonding strength is usually evaluated through tensile tests until the detachment of the adherent specimens. If the failure occurs within the adhesive layer is considered a cohesive failure, instead, if it occurs at the interface

with one of the specimens is an adhesive failure. The adhesion force of PU-LDA was examined in lap shear configuration and compared with the control group PU-LYS. Indeed, it has been the most often used adhesion bonding test among the several existing methods for evaluating adhesives [21,94,95].

We have chosen four materials to evaluate the adhesion of PU-LDA and used PU-LYS as the control group. Lap shear results for all surfaces and conditions tested are provided in Figure 20-c. Aluminium and glass are high-energy surfaces, and the resulting adhesion is considerably higher (respectively 2600 ± 150 kPa and 2836 ± 462 kPa for PU-LDA and 720 ± 103 kPa and 1237 ±47 kPa for PU-LYS) than low-energy surfaces like polypropylene (306 ± 17 KPa for PU-LDA and 194 ±14 for PU-LYS). These differences between high and low-energy surfaces could be attributable to hydrogen bonding or polar interactions since the polymers have a relatively large polar component and ester/urea bonds [96]. Instead, the effect of dopamine bonded to the chain extensor is remarkable and the increase in adhesion strength is >100% when compared with the control group (PU-LYS) for aluminium, ≈ 200% for glass and >50% for polypropylene.

Lap shear adhesion tests were performed also on porcine skins to evaluate the adhesive's possible applications on biological tissues (Figure 19-d). With the biological similarity to the human dermis, porcine skins are commonly used for biomedical experiments [95,96]. A NIR irradiation procedure was set up to achieve a fast and spatially controlled melting of PU to allow the exploitation of adhesiveness on biological tissues (Figure 20-e). NIR irradiation can be a fast and efficient procedure to localize specific areas of melting on the PU-LA biomaterials when it is applied on a tissue surface. Low laser intensity for fast irradiation times is sufficient to allow a complete fusion of the material with efficient spatial control. NIR irradiation was

employed to induce spot melting of PU-LDA, enabling precise size tuning by adjusting the laser diameter (Figure 21).

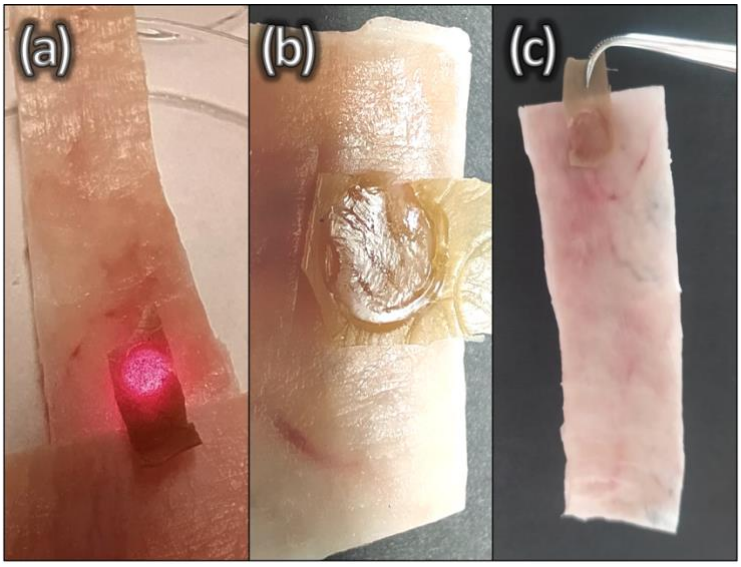

Figure 21 (a) PU-LDA film melting, by laser NIR irradiation, after 60 seconds at a power density of 4W/cm^2; (b) film adhesion on porcine skin after melting; (c) adhesive strength of PU-LDA film on porcine skin.

Complete melting was achieved in less than 60 seconds at a power density of 4W/cm^2. We observed that dopamine remarkably increases the adhesiveness of polyurethane in every tested condition. In dry conditions, the adhesion strength of PU-LDA is 50 ± 4 kPa which is 100% higher than PU-LYS (26 ± 3.6 kPa). The difference increases even more when water is involved, 150%, indeed after 2 minutes of immersion in DPBS the adhesion strength of PU-LDA decreased to 40 ± 3.8 and PU-LYS to 13.53 ±1.6. Lastly, when the experiment was performed underwater at 37°C, PU-LDA decreased to 28.2±0.6 kPa which is 150% higher than PU-LYS equal to 9.5 ± 1.4 kPa.

Adhesive failure was observed for all tested samples, indicating a stronger cohesive strength than adhesion. Overall, all the presented adhesion results are consistent with the literature on lap shear configuration. Zhou et al. synthesized a Poly(ester-urea) based degradable adhesive polymer, inspired by mussel adhesive proteins, using interfacial polycondensation. They have demonstrated that their polymer has an adhesion strength, without oxidative cross-linker, of 1000 KPa on aluminium adherents and 3kPa on porcine skin [95].

Xu et al. have designed a stretchable bio-interfacial electrode based on highly adhesive elastomer that contains dopamine as a pendant group suitable for electromyogram measurement. It exhibits underwater adhesive strength equal to 16 kPa with epithelial tissue [96].

Matos-Pérez et al. observed a 1.3 ± 0.2 MPa adhesion strength to aluminium with their 10% catechol and 90% styrene copolymer [94].

The main advantage of our polyurethane, although our results showed higher performances than cited works, is that it is a solid processable material, capable of expressing high adhesion to different substrates and in different conditions after melting occurs. Indeed, it does not require the use of organic solvents to be spread properly on the target and can be processed to obtain precise and defined microfibers and to build up structures with a tuneable microarchitecture and external shape. Furthermore, it does not require crosslinkers or oxidants to express high adhesion. To express high adhesion PU-LDA can either be pre-melted by simple fusion or, once applied as solid on the surface to be attached, by precise spatial control by laser irradiation. These conditions, for instance, are ideal for wearable devices that require a stimulus-sensitive adhesive interface between the sensor and the skin.

Rheological analyses of PU-LDA and 3D printing procedure

Material rheological properties are the most critical parameters for extrusion 3D printing of melted polymers [97,98]. Rheology influences the melt temperature and helps to determine the material output and flow rate by predicting the material flow and the required pressure through the nozzle during the process. In melt extrusion 3D printing both temperature and shear rate strongly affect the deformation behaviour and melt viscosity which represents the most important parameter in determining the optimal processing conditions. Viscosity decreasing with increased shear rate can be associated with shear thinning behaviour which is favoured melt extrusion 3D printing application as this means the ability of the material, at a given temperature, to be easily pushed through a nozzle but also to maintain the given structure and shape after deposition due to the initial viscosity value recovered as pressure is removed [99]. Studying the optimal viscosity range can help in predicting material suitability in the 3D printing process. A high value of zero-shear viscosity, at a low shear rate, could help to maintain the shape after deposition. Instead, viscosity data at high shear rates are more representative of the materials' rheological properties during extrusion. Indeed, it has to be low for efficient printing but, at the same time, it should not be so low that it flows as liquids from the printing nozzle [100].

As shown in Figure 22-a, PU-LDA, tested at 80, 75, 70 and 65 °C, showed shear thinning behaviour at all tested temperatures with values ranging between 10^4 and 10^5 Pa x s at a low shear rate (0.01 s^{-1}) down to 10^2 Pa x s at 100 s^{-1} with more than two orders of magnitude difference, which agrees with previous studies suggesting that printable polymeric systems are in the range 10-1000 Pa x s at high shear rate [97,101].

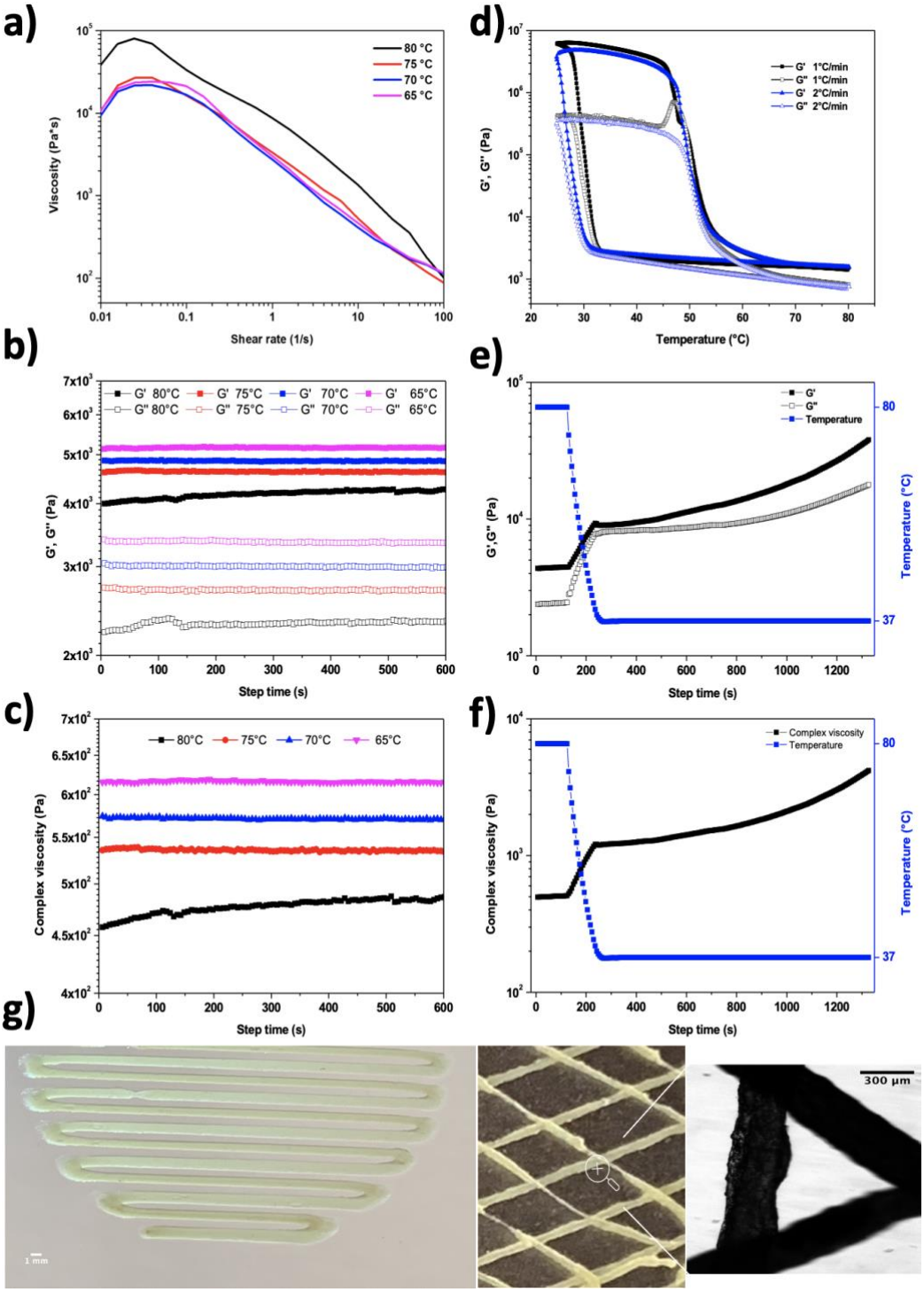

Figure 22 a) Flow sweep analysis, b) Time sweep analysis with moduli versus time at 80, 75, 70 and 65 °C of PU-LDA, c) complex viscosity during Time sweep at constant temperatures, d) Temperature ramp analysis (80-25 °C) and back (25-80 °C) at 1°C/min, e) Time sweep analysis with moduli versus time at 80 °C for 120 seconds and at 37 °C for 1200 seconds, f) complex viscosity during time sweep after temperature variation g) Printed patterns of PU-LDA and microfiber detail.

However, at fixed temperature and deformation, melted materials have to keep constant their storage (G′) and loss modulus (G″), such as their viscosity values, if not it might be necessary to change printing parameters during printing with negative repercussions on the success of the extrusion process. Time sweep analyses were performed at different temperatures, keeping constant strain and angular frequency to evaluate this aspect. It is possible to note that complex viscosity (in the order of 10^2 Pa x s) and both G′ and G″ (in the order of 10^3 Pa) were constant up to 600 s and values increased as temperature decreased from 80 to 65°C (figure 22-b-c). The higher the modulus and viscosity the more difficult the flow resulting in nozzle clogging. However, as values are too low it can result in a leakage of material from the nozzle [102]. Thus, material rheological properties are dependent on temperature, which is another crucial factor to not overlook. Rheological investigation results show that the viscosity and moduli values of PU-LDA are in a range that is well suited for processing by the melt extrusion 3D printing technique [103].

In the melt-extrusion setting the correct temperature can change the printing outcomes. High print temperatures can determine the too-low viscosity of polymer with consequently flow instability. On the other hand, low processing temperatures can determine points of failure and defects due to incomplete polymer melting [67,104]. The temperature ramp rheogram (Figure 22-d) showed how G′ and G″ strongly depend on changing temperature. This and the tack test measures highlight PU-LDA's broad adhesive working temperature range. Indeed, after melting occurs, it is possible to express high bioadhesion even at 37°C to avoid any undesired effect due to temperature difference when applied to tissues. As temperature decreased from 80 to 25 °C moduli increased with a drastic jump at 33 °C of about four orders of magnitude, reaching, at 25 °C, 6 x 10^6 and 4 x 10^5 Pa for G′ and G″ respectively,

showing a more structured material at this temperature. As the temperature increased again up to 80 °C moduli gradually decreased up to 46 °C and at this temperature dropped immediately reaching 1.5 x 10^3 and 8 x 10^2 Pa for G′ and G″ respectively at 80°C. Data are in accordance with DSC results.

In the melt-extrusion 3D printing process, an essential consideration is the capacity of the deposited layer to adhere effectively to the subsequent layer. The quality of inter-layer adhesion significantly influences the outcome of the 3D-printed construct. Poor adhesion between layers can result in constructs with compromised mechanical properties, emphasizing the critical importance of achieving strong and consistent inter-layer bonding for the overall structural integrity and functionality of the printed object. Both viscosity and temperature play another key role in filament coalescence [105]. To better predict shape fidelity to the digital model, moduli and viscosity have to quickly recover their value after deposition. Ideally, the temperature should be high enough to ensure adhesion between successive layers, but at the same time able to support deposition and consequently structural integrity of the printed construct. Thus, time sweep analyses (Figure 22-e-f) were performed to study the time to get an increment of G′, G″ and complex viscosity of the material as temperature decreased. As the temperature dropped from 80 °C to 37 °C all values sharply increased by half an order of magnitude, while, as the temperature was constant at 37°C, they gradually increased up 3.8 x 10^4 Pa, and 4 x 10^3 Pa x s for G′ and complex viscosity respectively after ~1320 seconds. The quick and incomplete increase of these values may enable the layer's deposition, however, these values can allow layers adhesion thanks to the gradual increase over time.

The melt extrusion 3D printing study, reported in Figure 22-g, aimed to assess the feasibility of generating various fibre diameters and maintaining shape fidelity to the

digital model through the implementation of two distinct patterns. Both patterns were reproduced with high accuracy even when the nozzle traversed narrow curves. Melt-extrusion 3D printing, used to produce oriented microfibres, involves the heating and extruding of the polymer through a nozzle tip. The fibres are deposited on a heated build plate forming a specific pattern. The remarkable adhesion strength could allow us to produce adhesive coating patterns on inorganic metallic materials providing a structured interface that facilitates cellular attachment, promotes tissue growth, and improves long-term biocompatibility. Indeed, the presence of specific micropatterns, such as lines, dots, or pits, can guide cell adhesion, spreading, and alignment. These micropatterned coatings promote focal adhesion formation, cytoskeletal rearrangement, and enhanced cell-substrate interactions, ultimately leading to improved tissue integration. The main concern about this technique is the potential degradation due to the high temperature. Indeed, in most of the literature, it is set in a range between 150 and 230°C [106]. However, thanks to the low melting point of PU-LDA, we were able to perform this process at <80°C. Furthermore, thanks to the results over time observed from the rheological time sweep analysis, we were able to perform the melt-extrusion processing with a constant pressure of 75 psi. Lastly, the quick recovery in moduli and complex viscosity, by half an order of magnitude, when the temperature dropped from 80 °C to 37 °C helped us better predict shape fidelity to the digital model.

3.2 Overcoming the Blood-Brain Barrier: A Novel Approach Using a Conductive Bioadhesive Coating for Voltage-driven Drug Delivery in Glioblastoma Multiforme

Summary

Glioblastoma multiforme is the most common type of malignant brain tumour in adults. The survival rate is only 15 months, with less than 5% of patients surviving beyond 5 years. The main challenge in treating it is the blood-brain barrier (BBB), which regulates the entry of chemicals into the brain. To address this challenge, we have developed a conductive bioadhesive coating that can be inserted inside the tumour microenvironment and deliver drugs, bypassing the BBB, when a voltage is applied.

Bioadhesive coating fabrication

PEDOT:PSS was incorporated in a PU-LDA matrix to develop a conductive bioadhesive (CB) electrophoretic platform that enables the direct transfer of molecules from a solid-state device (Figure 23).

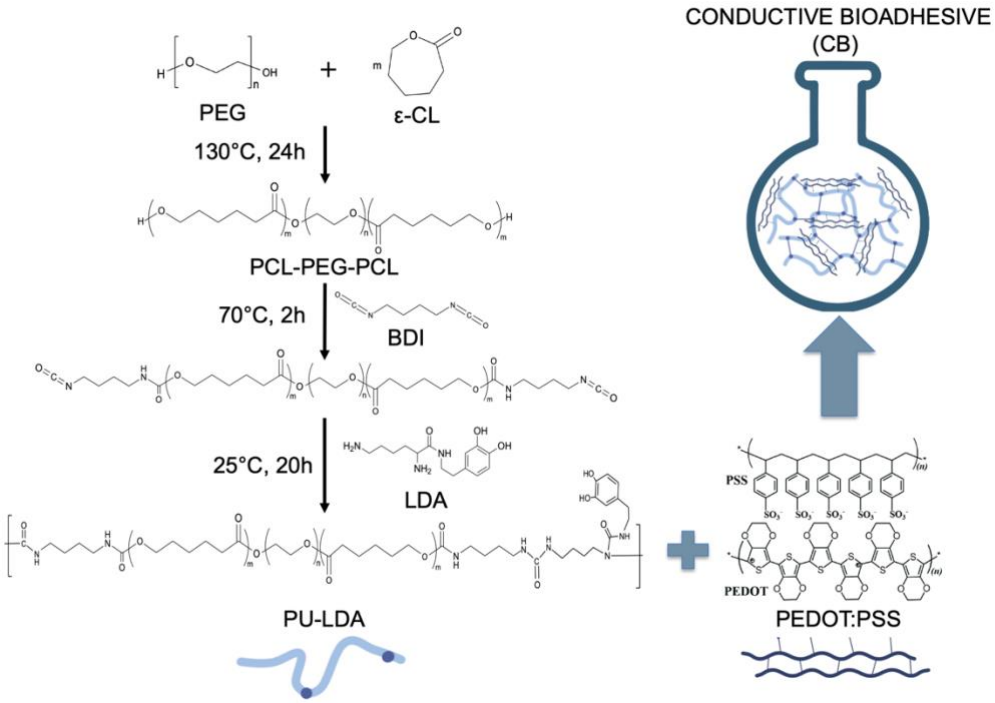

Figure 23 Scheme of PU-LDA synthesis and PEDOT:PSS incorporation to develop a conductive bioadhesive (CB) electrophoretic platform.

As highlighted in the preceding chapter, PU-LDA is a type of polyurethane urea that exhibits exceptional hydrolytic stability, a low melting point of 55°C, and high adhesiveness. These attributes make PU-LDA a suitable choice for use as a coating interface between metallic prostheses or implantable devices and biological tissues, thereby enhancing biointegration and biological tolerance. PEDOT:PSS is a conductive polymer blend that combines electrical conductivity with biocompatibility. Its conductive nature enables the controlled release of drugs through electrical stimulation, developing smart drug delivery systems. Nevertheless, as suggested by percolation theory, a minimum amount of conducting polymer is necessary to establish a conductive pathway within an insulative matrix [37]. Therefore, the polymeric blend was formulated by incorporating 75% insulative matrix (PU-LDA) and 25% conducting polymer (PEDOT:PSS). The final polymer was cast onto Teflon

moulds to create rectangular films, 2.5x1.5 cm and 100µm thick, to perform dry conductivity and onto platinum disks, ∅ 1cm and 140 µm thick, to perform electrochemical impedance spectroscopy and cyclic voltammetry in wet conditions (Figure 24).

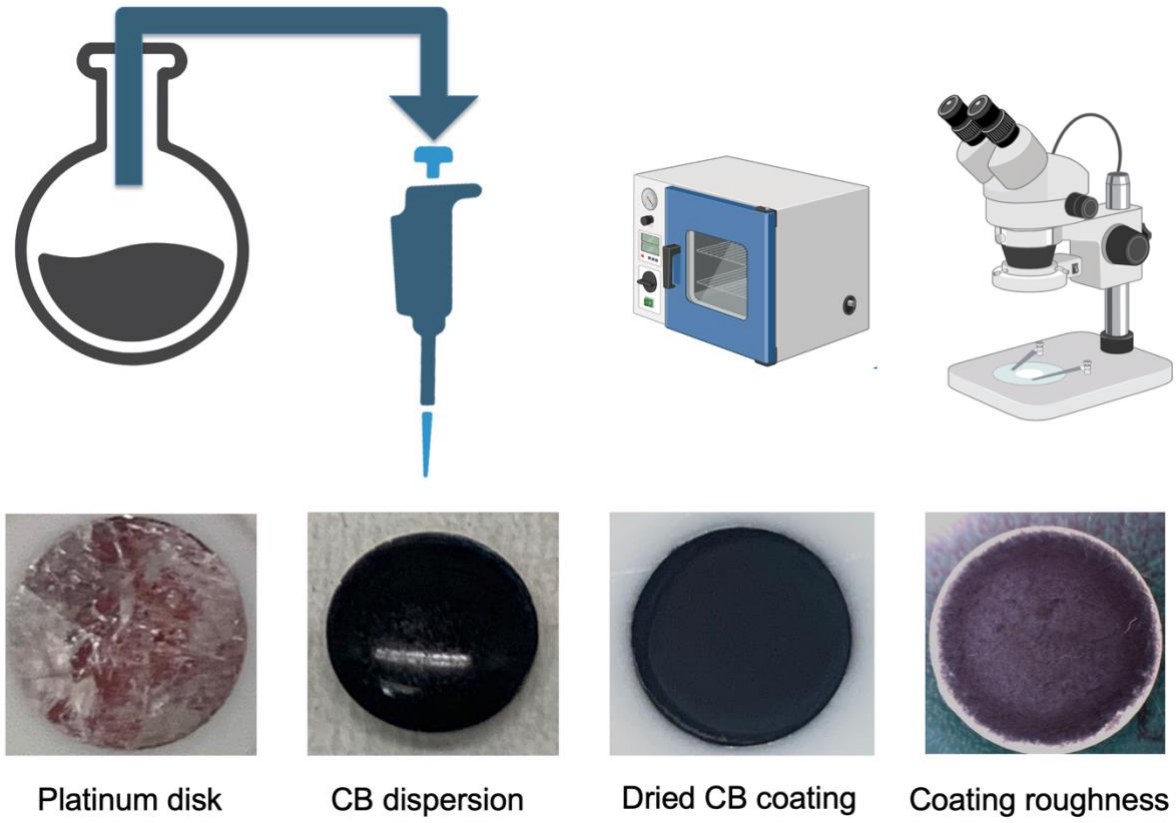

Figure 24 Illustration of the CB coating process on the platinum disks and its roughness observed under a microscope.

The roughness, observed using the microscope, could increase the interfacial surface area available for charge transfer, which results in lower impedance and higher capacitance, thereby enhancing the electrochemical performance.

Electrochemical characterization

The electrical conductivity of dry samples was measured using impedance spectroscopy in the frequency range of 10^{-1} to 10^{4} Hertz. The average impedance of the samples was found to be 13.18 ± 1.1 Ω , while the impedance at 1kHz was measured to be 13.56 ± 1.23 Ω. Based on these measurements, the electrical conductivity was calculated to be 5.34 ± 0.46 S/cm and 5.19 ± 0.49 S/cm respectively. The resulting data is presented in Figure 25.

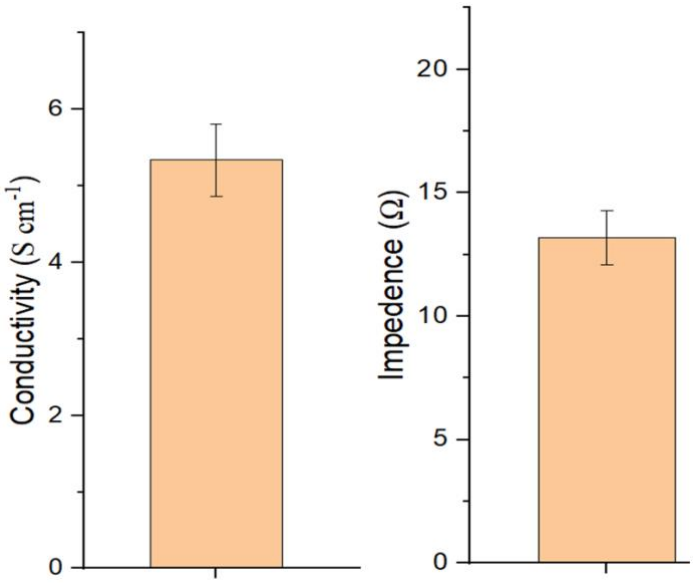

Figure 25 Electrochemical characterization of CB in dry conditions. Data represent the mean± standard deviation (n=5) in the frequency range of 10^{-1} to 10^{4} Hertz.

The findings of this study are consistent with those of prior research that employed identical concentrations of PEDOT: PSS in alternative polyurethane matrices. In their study, there was a noticeable decline in impedance and a corresponding increase in conductivity between the 5 wt% and 10 wt% PEDOT: PSS/PU composites. This

indicates that a percolation threshold was most likely surpassed between those two loadings, with saturation occurring around 20 wt% [107].

During the electrochemical impedance spectroscopy (EIS) measurements performed in wet conditions, impedance and phase shift were measured over a frequency range of 10^{-1} to 10^{5} Hertz while applying a sinusoidal voltage magnitude of 10 mV. The resulting values, bode plots of the impedance magnitude and phase angle, obtained for the sample in comparison with platinum are displayed in Figure 26.

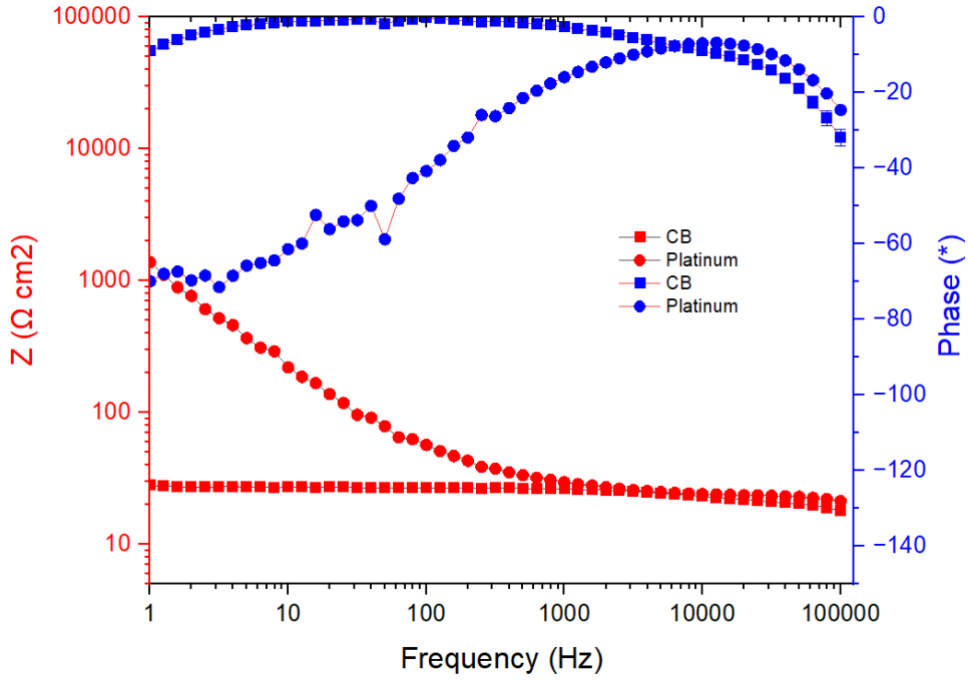

Figure 26 Bode plots of the impedance magnitude and phase angle of CB compared with platinum. Data represent the mean± standard deviation (n=5) in the frequency range of 10^{-1} to 10^{5} Hertz.

At high frequencies, between 1 and 100 kHz, the impedance and phase of CB were similar to those of platinum. However, at low frequencies, between 1 and 1000 Hz, the impedance of CB remained stable while the impedance of platinum increased significantly by two orders of magnitude. Additionally, from 1000 to 1 Hz, the phase

angle of CB reduced whereas the phase angle of platinum increased. The phase angle depends on the kinetics of the electrochemical reactions, the impedance of the system, and the frequency of the applied signal. Capacitive elements tend to lead the current waveform relative to the voltage waveform, resulting in a negative phase angle. Instead, when the current and voltage are in phase there are no faradaic processes involved indicating a resistive system. In such systems, the current follows the voltage waveform without any phase shift, and power is dissipated as heat.

The electrochemical behaviour of a material can be characterized by its capacitive and resistive charge transfer properties, which can be analyzed using a cyclic voltammetry (CV) technique. To determine the current that resulted from sweeping the voltage between -0.6V and 0.8V at a scan rate of 150 mV s^{-1} in wet conditions, a CV was carried out. The mean value of the last 10 cycles was then calculated and compared to that of platinum. The CV plot of the material under investigation displayed a trapezoidal shape, indicating a combination of capacitive and resistive charge transfer, which is indicative of pseudo-capacitive behaviour (Figure 27).

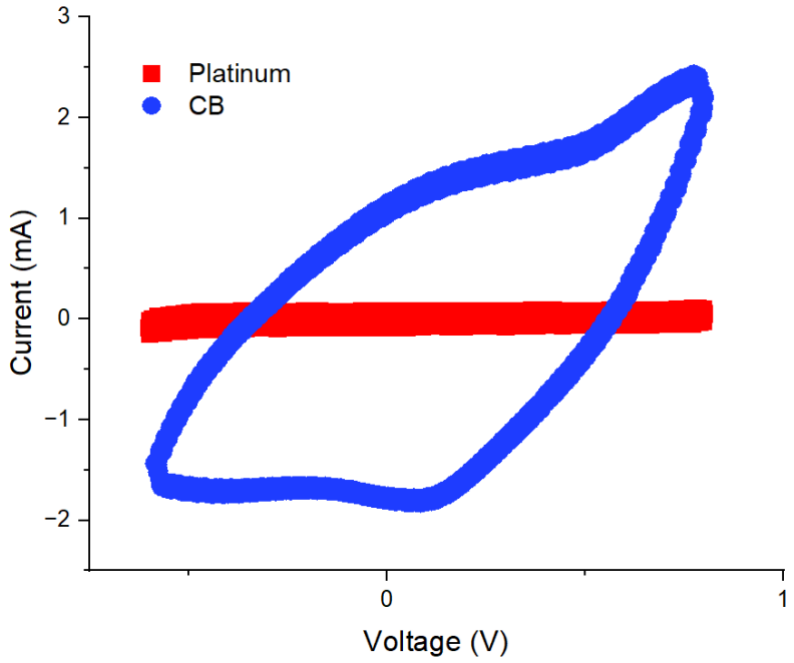

Figure 27 Cyclic voltammetry of CB compared with platinum. Data represent the mean± standard deviation of the last 10 cycles (n=5).

To quantify this trend, the Charge Storage Capacity (CSC) was computed by integrating the current response over time for the 10th cycle, as demonstrated in Figure 28 in comparison to the response of platinum.

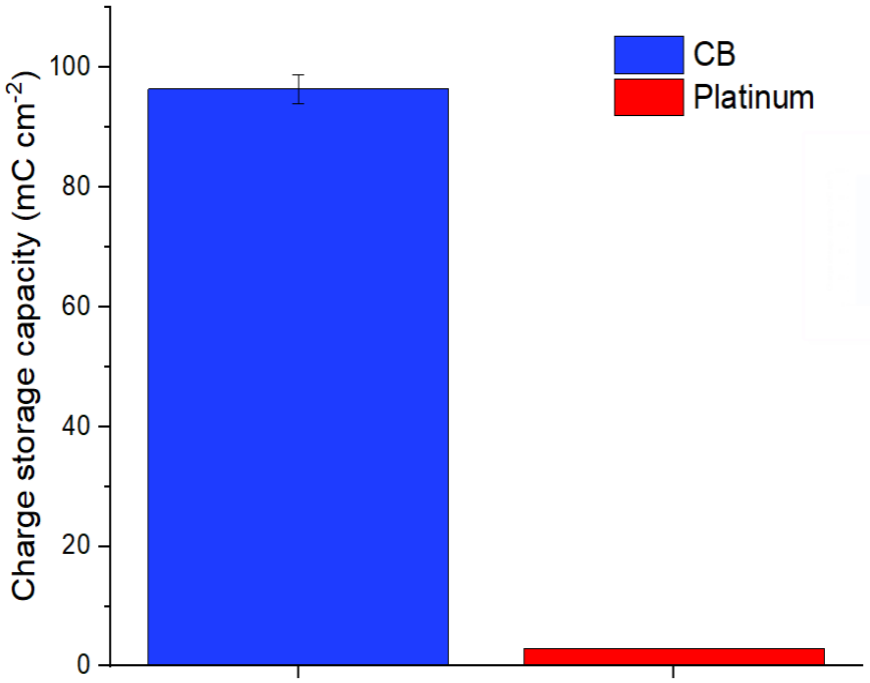

Figure 28 Charge Storage Capacity of CB compared with platinum. Data represent the mean± standard deviation (n=5).

It was noted that the CSC value is two orders of magnitude larger than that of Platinum confirming a significant benefit in electrochemical performance over conventional Platinum electrodes. Hence, solvent casting PEDOT:PSS dispersions in PU-LDA proved an effective way of fabricating an electrically conductive bioadhesive coating. It holds potential applications as an interface between metallic prostheses or implantable devices and biological tissues. This usage is anticipated to enhance biological tolerance and biointegration, creating a more harmonious interaction between the implant and the surrounding biological environment. Furthermore, the coating's conductivity opens up opportunities for voltage-driven release of molecules, providing a dynamic and controlled method for the delivery of therapeutic agents or other substances within the biological context. This dual functionality positions the coating as a versatile and promising element for advancing the performance and compatibility of biomedical implants.

Drug delivery device fabrication

Building upon the suitable electrochemical properties extensively examined in the preceding chapter, CB emerges as an enticing candidate for a multifunctional coating capable of actively regulating therapeutic release within the tumour microenvironment. To harness this potential, a 3 wt% dispersion of Paclitaxel (PTX) was seamlessly incorporated into the polymeric blend. The fabrication process involved dip-coating porous titanium rods (Ti rod) into the PTX-loaded polymeric dispersion to produce the devices for voltage-driven drug delivery (Figure 29).

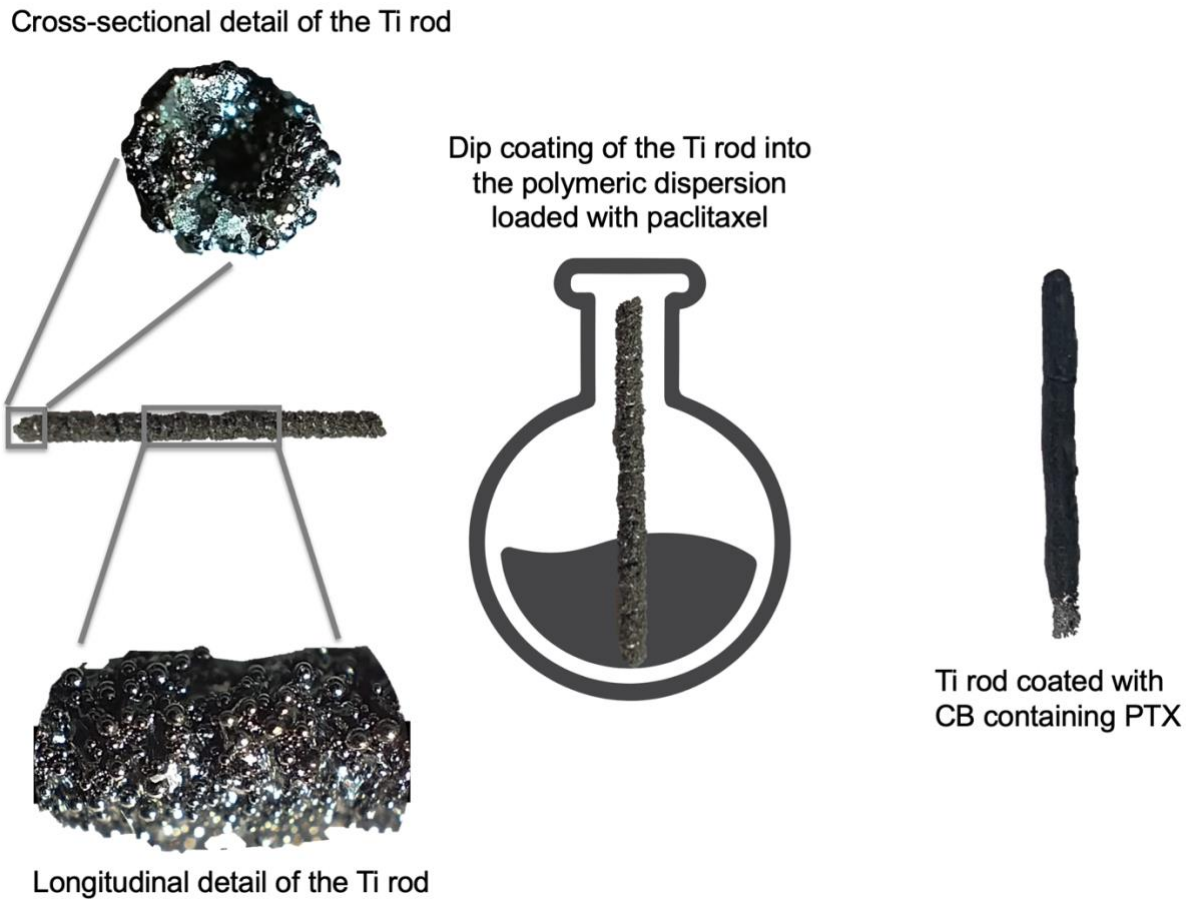

Figure 29 Illustration of the dip-coating process of the Ti rods into the PTX-loaded polymeric dispersion.

Specifically designed around the neurosurgical toolkit to perform a biopsy, they will be supported by a cartridge during the insertion in the tumour microenvironment. The determination of the final mass coated onto these devices involved weighing the completed samples and subtracting the previously collected weight of the titanium rods. A total of 50 samples were meticulously produced, exhibiting varied masses ranging from 3.5 to 7 mg, to facilitate comprehensive release and in vitro studies. To assess drug loading, four samples spanning the entire mass spectrum were selected. The coating was dispersed in Acetonitrile/water (65/35), and the amount of PTX in these solutions was quantified using High-Performance Liquid Chromatography (HPLC). The PTX peak manifested after 5.6 minutes during elution, and its area was calculated and compared with the area of a calibration curve to accurately convert the recorded signal into the amount of drug present in each sample. The resulting drug loading was determined to be 2.48% ± 0.04, signifying a homogeneous distribution of PTX and ensuring consistency and reliability in the drug loading for the entire range of masses under investigation.

Release study

Paclitaxel, a widely employed chemotherapeutic agent, plays a crucial role in the treatment of various solid cancers, including those affecting the breast, lung, bladder, and prostate. Its mechanism of action involves binding to beta-tubulin within microtubules, thereby impeding their depolymerization and effectively stabilizing these dynamic structures. Microtubules are composed of proteins that dynamically

polymerise and depolymerise during the cell cycle. Therefore, paclitaxel interferes with the dynamic processes required for cell division by preventing the normal disassembly of microtubules, this disruption not only halts the cell cycle but can also initiate apoptotic signals in tumour cells. Cells that are damaged or unable to complete the division process may activate apoptosis, a programmed cell death mechanism.

Currently, PTX administration typically involves intravenous injection, a method associated with severe side effects. Therefore, its controlled voltage-driven release from the presented CB devices could be particularly useful to attack the tumour from its centre, bypassing the BBB, while minimizing PTX side effects.

PTX's inherent lipophilic nature renders it poorly soluble in water or phosphate-buffered saline (PBS). Indeed, a recent study measured its solubility in PBS at 37 °C, revealing a limited solubility of approximately 0.2 µg/mL, with no discernible trend over varying incubation times. In contrast, when immersed in a 1:1 mixture of fetal bovine serum (FBS) and PBS buffer, paclitaxel exhibited a significantly increased solubility, reaching 35 µg/mL after a 7-hour incubation at 37 °C [108].

This finding underscores the pronounced solubilizing effect of serum proteins, indicating a potential avenue for improving paclitaxel's solubility during controlled release studies. Consequently, the release study of PTX from the presented CB devices was conducted at 37°C inside Franz's cells under stirring in a 1:1 mixture of FBS and PBS buffer. The release was performed in enhanced condition applying a constant voltage equal to -1V and in passive condition at 0V. A schematic representation of the release conditions and the extraction process is illustrated in Figure 30.

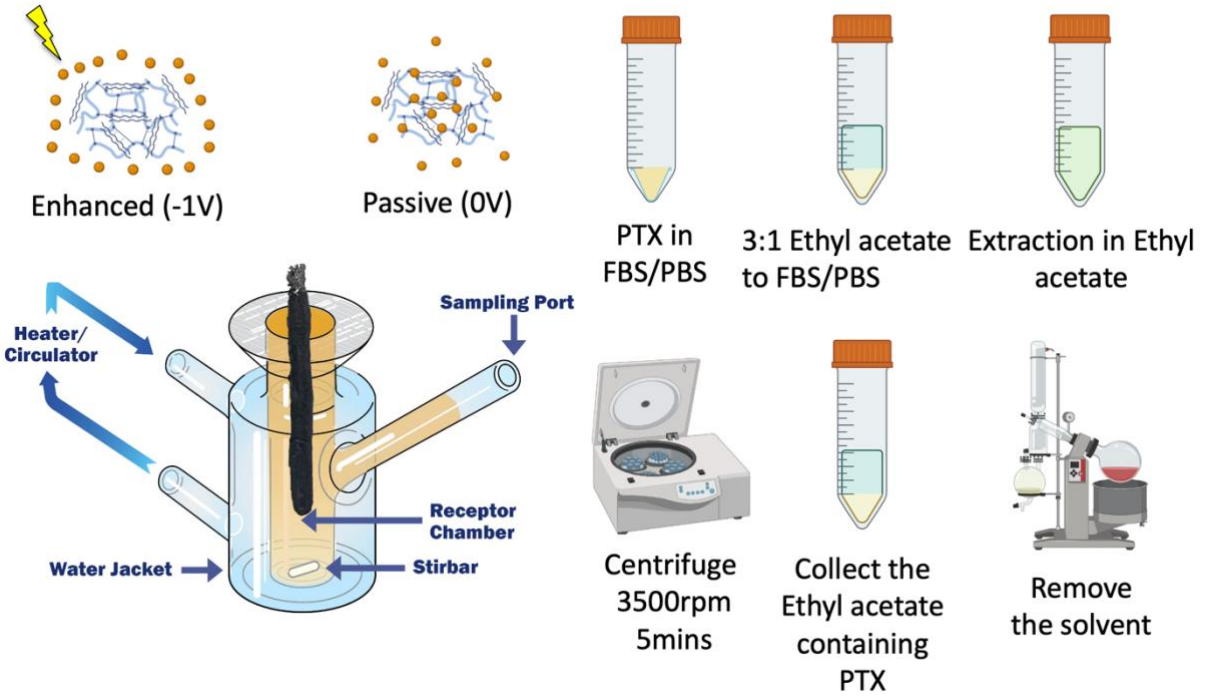

Figure 30 Schematic representation of the release conditions and the extraction process of PTX.

During the release study, the entire volume within the chamber was systematically collected and replenished with a fresh solution at each designated time point. The assessment of passive drug release spanned intervals of 10 minutes, 1 hour, 4 hours, 24 hours, 3 days, 7 days, 8 days, 9 days, and 10 days. In contrast, the evaluation of enhanced drug release involved measurements at 10 minutes, 1 hour, and 4 hours. Subsequently, the sample was maintained in passive conditions for an additional 20 hours, facilitating a direct comparison with the 24-hour time point under passive conditions. This experimental design allows for a comprehensive understanding of both passive and enhanced drug release dynamics over specified time frames.

The releases from the passive condition are reported in Figure 31-a while the cumulative release behaviour is illustrated in Figure 31-b.

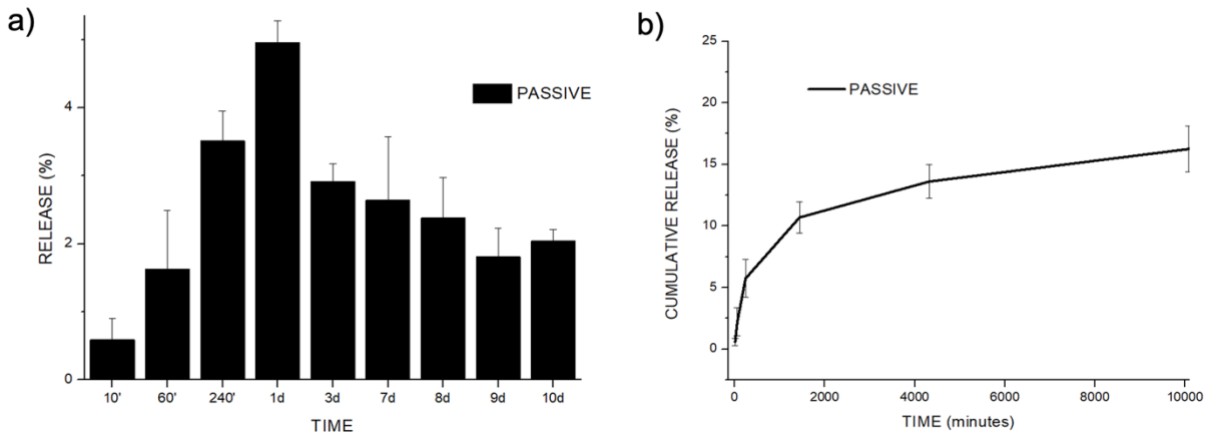

Figure 31 a) % of PTX released at each time point from the CB devices in passive conditions, b) cumulative release behaviour of the CB devices in passive conditions. Data represent the mean± standard deviation (n=3).

The observed trend in the drug release data reveals an initial increase over time, peaking at 1 day, followed by a subsequent decline until the conclusion of the study. This pattern suggests a saturation of the release profile, indicating that the system reaches a point where the capacity to release the drug becomes limited or stabilizes.

The releases from the enhanced condition are compared with the passive one and reported in Figure 32-a while the cumulative comparison, considering only the time points when the enhanced release was kept constant at -1V, are illustrated in Figure 32-b.

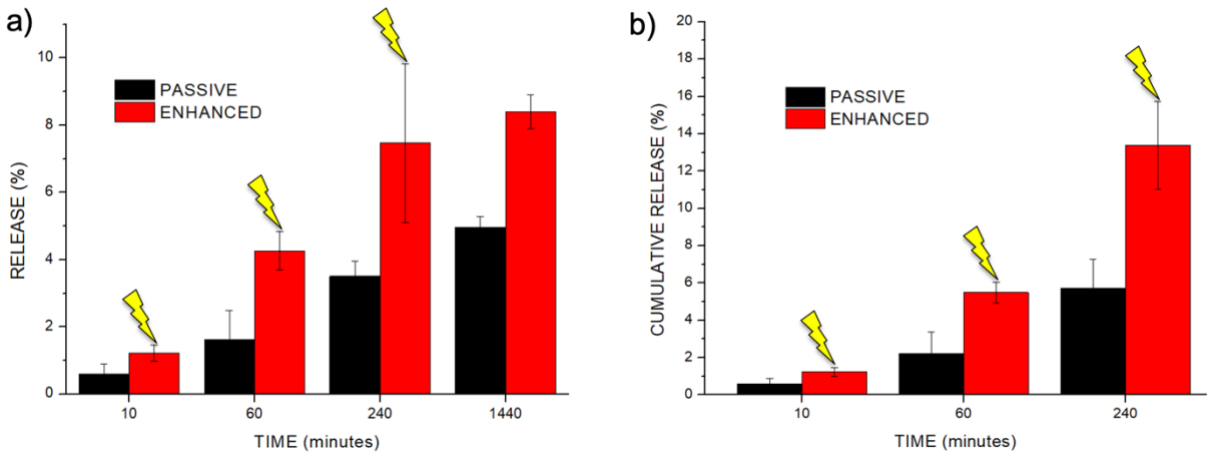

Figure 32 a) comparison of the % of PTX released at each time point between enhanced and passive conditions from the CB devices, b) cumulative comparison. Data represent the mean± standard deviation (n=3).

The comparison of drug release demonstrates a substantial increase when voltage is applied. In just 10 minutes, the enhanced group released 1.23% ± 0.24 of the loaded drug, while the passive group released 0.59% ± 0.3, resulting in a remarkable 108.4% increase in PTX released. After 60 minutes, this disparity widened further, with the enhanced group releasing 4.3% ± 0.54 of the loaded drug, compared to the passive group's release of 1.63% ± 0.86, representing a substantial 163.9% increase in PTX released. Interestingly, after 240 minutes, the gap between the groups began to narrow, as the enhanced group released 7.5% ± 1.25 of the loaded drug, while the passive group released 3.51% ± 0.44, still indicating a noteworthy 113.7% increase in PTX released. Subsequently, the enhanced sample was maintained in passive conditions for an additional 20 hours releasing 8.4% ± 0.5 compared to 5% ± 0.3 from the passive indicating a 68% increase. This dynamic interplay between the enhanced and passive release profiles highlights the effectiveness of applying

voltage in promoting controlled and increased drug release, presenting valuable insights for optimizing drug delivery systems.

Gliadel® wafers are currently the only implantable medicine to be granted with a marketing authorization, since 1998, specifically indicated for the treatment of glioblastoma. These implants are composed of a slow-degrading 1,3-bis-(p-carboxyphenoxy)-propane copolymer combined with fast-degrading sebacic acid, compressed into disks measuring 1.4 cm in width and 1 mm in thickness. The integration of Carmustine within the implant, directly placed into the tumor cavity, circumvents the BBB, facilitating heightened drug concentrations close to tumor cells[109].

The biocompatibility of the electroactive bioadhesive coating can be examined in terms of biological, anatomical, and functional compatibility, for comparison with Gliadel® wafers. The biological compatibility of PU-LDA, serving as the polymer matrix, was assessed in Chapter 3.1 and published in 2023 [84] and PEDOT:PSS, the conductive filler utilized, stands as one of the most widely employed conductive polymers in existing literature.

The functional compatibility of the electroactive bioadhesive coating is evidenced in its ability to finely regulate the release of drugs based on applied voltage and stimulus duration. This precise control mechanism leads to a more efficient drug release profile when compared to Gliadel® wafers.

Lastly, in terms of anatomical compatibility, the main advantage of the proposed devices lies in their utilization of the pathway to the inner core of the tumor that remains after a biopsy procedure. Indeed, this electroactive bioadhesive devices were designed around the neurosurgical toolkit to perform a biopsy to reduce the invasiveness of local drug delivery while overcoming the BBB. Furthermore, this

pathway will be safeguarded with an outer guide and a dummy component to prevent contaminations for as long as necessary, facilitating the insertion of a cartridge containing the delivery devices. This integrated system is poised to mitigate any potential long-term effects on tissues in contact with these coatings, while minimizing invasiveness, thereby fostering improved therapeutic outcomes.

In vitro cytotoxicity studies

Neuroblastoma cells SH-SY5Y were employed to assess the efficacy of various concentrations of PTX ranging from 0.1 to 1000 nM over 24 and 48 hours. Due to its lipophilic nature, PTX was initially dispersed in DMSO and subsequently diluted in complete media to achieve the desired concentrations. The resulting viability, as depicted in Figure 33, exhibited a linear decrease corresponding to the escalating concentration of PTX.

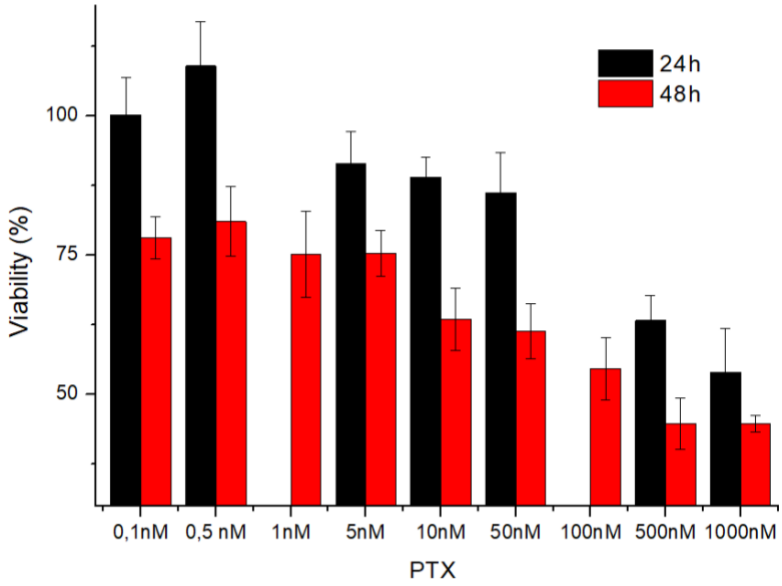

Figure 33 PTX cytotoxic effects on SH-SY5Y viability. Data represent the mean± standard deviation (n=5).

Notably, a more pronounced cytotoxic effect was observed after 48 hours, underscoring the time-dependent nature of PTX-induced apoptosis, wherein the impact on cell viability strengthens with prolonged exposure.

The PTX release from the CB devices in the growth media was analysed under both passive and enhanced conditions at 1 and 4 hours. Subsequently, these media were

employed to cultivate cells, and the observed effects were compared with the direct cytotoxicity of PTX. The cytotoxicity stemming from the devices was evidenced by the survival of only a few cell clusters in the passive groups and none in the enhanced ones. However, a noteworthy challenge arose during the analysis as the devices released microscopic polymer fragments that absorbed light at the same wavelength. This interference compromised the accuracy of the quantitative evaluation of the cytotoxic effect using the MTS assay (Figure 34).

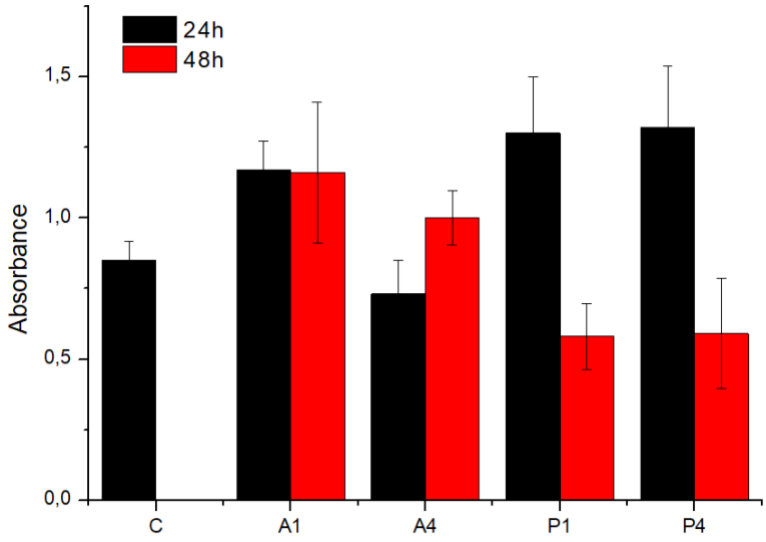

Figure 34 Absorbance recorded, using the MTS assay, from passive (P1, P4) and enhanced (A1, A4) conditions at 1 and 4 hours compared to the control (C). Data represent the mean± standard deviation (n=5).

Hence, to evaluate the efficacy of these devices under both passive and enhanced conditions after 1 hour, a chambered borosilicate coverglass was employed for visualization of cytotoxicity through live/dead staining. Additionally, the impact of voltage alone and its combination with a 5nM concentration of PTX was analyzed. This approach aims to provide a comprehensive understanding of the cytotoxic

effects, allowing for the assessment of both the intrinsic impact of the devices and the synergistic effects when voltage is applied in conjunction with PTX (Figure 35).

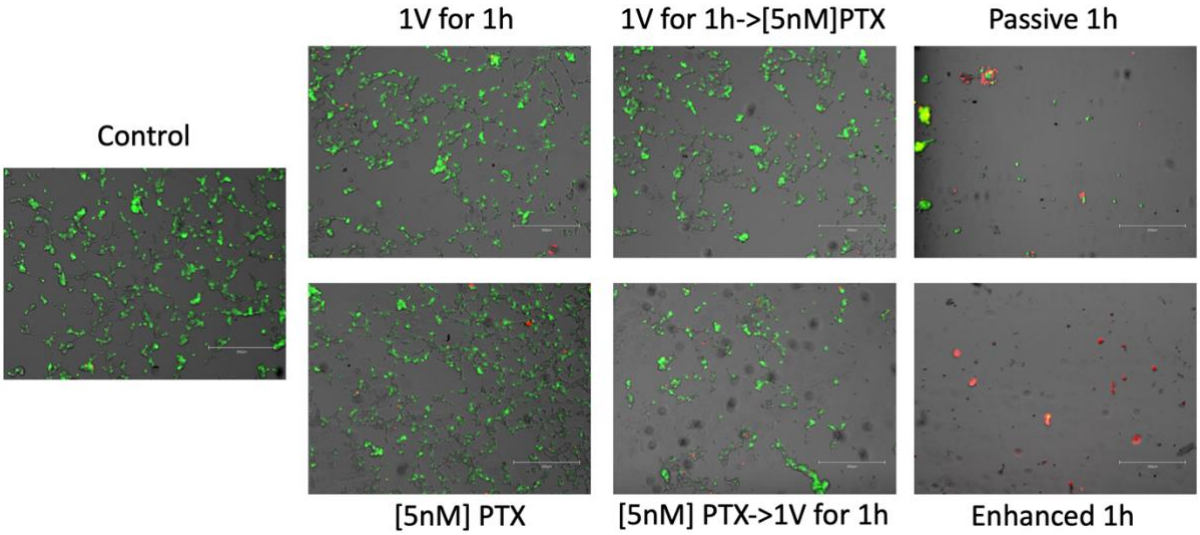

Figure 35 Live/dead staining of SH-SY5Y (scale bar 300μm). Control (only cells), 1V applied to cells for 1h, [5nM] concentration of PTX in the media,1V applied to cells for 1h before adding [5nM] PTX, [5nM] PTX added before applying 1V for 1h, effects of 1h passive release from the CB device, effects of 1h active release from the CB device.

The live/dead staining methodology offers a visual and qualitative perspective, complementing the quantitative assessments and contributing to a more thorough characterization of the device's performance under varied conditions.

The application of voltage alone appears to have an insignificant impact on cell viability. However, the cytotoxic effect observed with 5nM PTX aligns with the 75% viability noted after 48 hours in the MTS assay. Notably, when voltage is applied in conjunction with PTX, it becomes evident that the cytotoxic effect is more pronounced when the drug is administered before the application of voltage. This finding supports our hypothesis that applied voltage alters the permeability of the cell

membrane, facilitating enhanced drug uptake. In the case of passive release from the CB devices, only a few cell clusters survived, underscoring a notable cytotoxic effect. Contrastingly, enhanced release induced a complete cytotoxic effect. These results highlight the potential of combining voltage application with drug delivery systems to augment therapeutic efficacy, demonstrating the synergistic effects of drug administration and voltage application for optimized cytotoxic outcomes. Moreover, this strategy aims to overcome chemoresistance and unnecessary exposure to healthy tissues by circumventing the BBB.

3.3 Polybutylene Succinate Processing and Evaluation as a Micro Fibrous Graft for Tissue Engineering Applications.

Summary

Various polymers, both natural (e.g., collagen, silk fibroin, chitosan, alginate) and synthetic (e.g., PU, PCL, PLA, PGS), have been successfully employed in the fabrication of porous scaffolds through electrospinning. While several electrospun conduits have been extensively studied for diverse tissue engineering applications, there is currently no established use for small-diameter conduits. Moreover, the exploration of artificial bile ducts as an alternative to the standard choledochojejunostomy technique for biliary reconstruction holds promise for maintaining a more physiological conduit for bile. Additionally, the need for tubular conduits extends to other critical applications such as peripheric limb revascularization, arteriovenous fistulae for hemodialysis, and peripheric nerve regeneration. This underscores the versatility and potential clinical impact of developing tubular substitutes for various medical needs.

Fabrication and morphological assessment of PolyBS scaffolds

We developed and tested a tubular scaffold for tissue engineering applications obtained by electrospinning, focusing on the optimization of the processing and characterization of the three-dimensional tubular construct. The setup and processing parameters used for the above goal are reported in Figure 36.

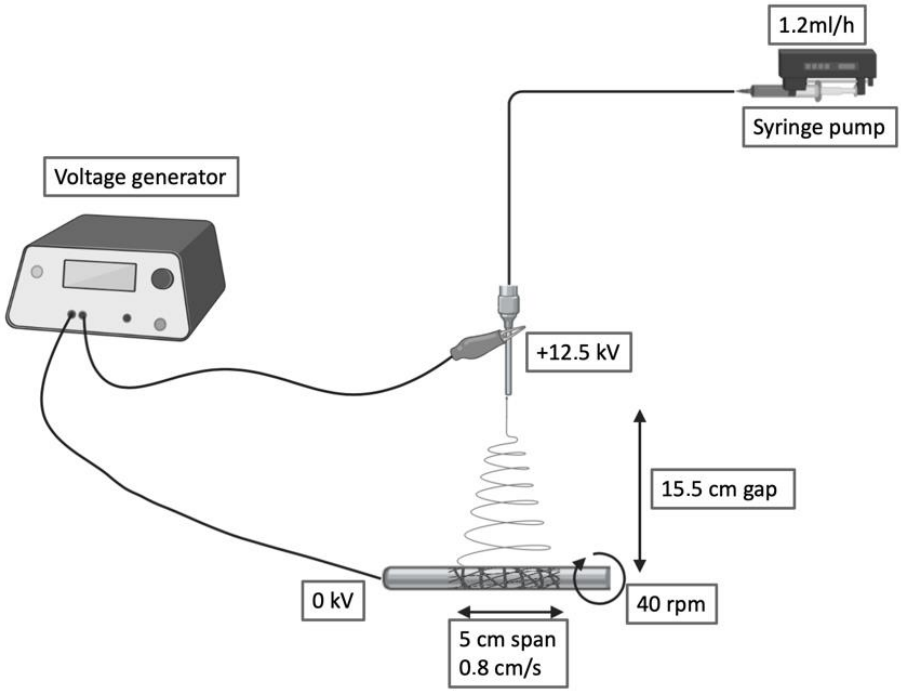

Figure 36 Schematic of the electrospinning setup and processing variables to produce PolyBS grafts.

The presented electrospinning setup can produce tubular constructs ranging from 2.6 to 10 cm in diameter and 2 to 12 cm in length. This versatility allows us to tailor the dimensions of this scaffold to different applications. Macroscopically, fibre deposition was smooth and homogeneous along the metal rod, without any gross defects (Figure 37-a).

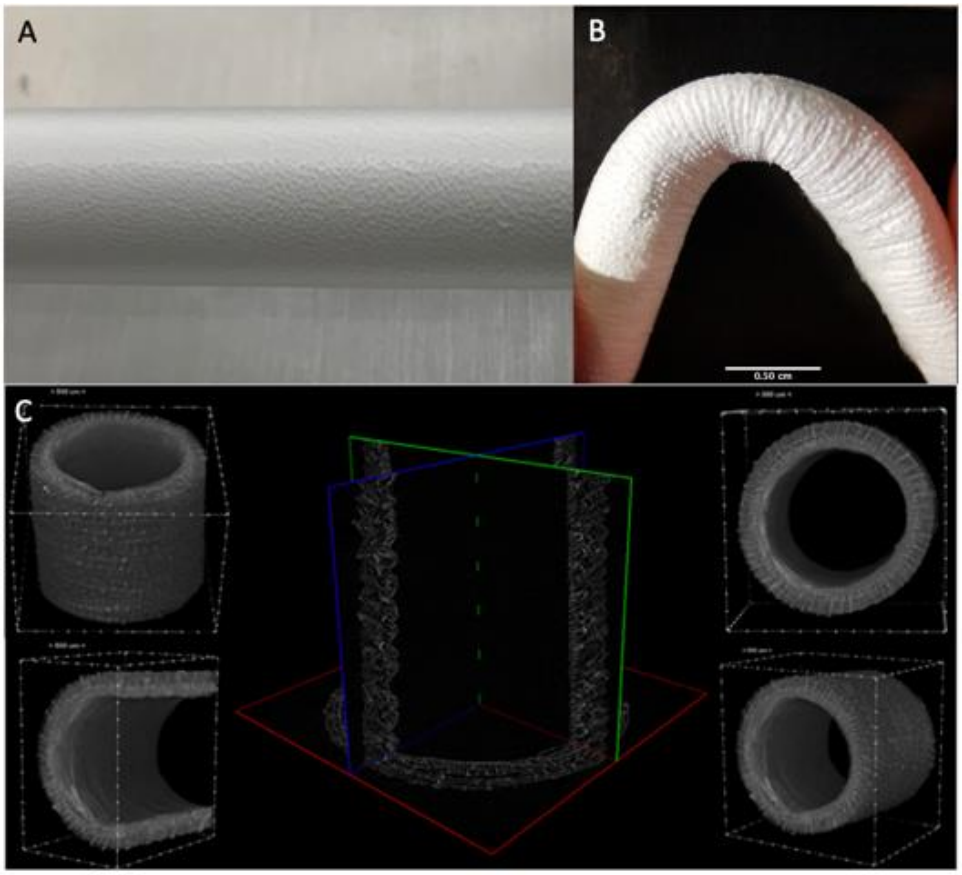

Figure 37 a) Details of the ES deposition on the rotating collector, b) Kinking resistance of the graft at 84°, c) uCT analysis of the graft structure.

An almost linear relation between the thickness of the electrospun layer and the deposition time was observed. The grafts were then plastically modified obtaining a corrugated geometry to minimize kinking when flexed (Figure 37-b). Indeed, this geometry allows them to be flexed up to 84° without compromising the lumen and avoid local perturbations in the fluid dynamics.

The micro-CT scans were adopted as an investigation method to study the whole morphology and size of the graft shown in (Figure 37-c) This analysis allowed us to inspect completely the graft structure and precisely measure wall thickness (mean size 490 ± 20 um) and inner diameter (mean size 3.62 ± 0.08 mm). The resulting

sample reconstruction underlines the absence of delamination and homogeneous morphology.

SEM was adopted as an investigation method to study the morphology and orientation of nanofibers. Observed under SEM (Figure 38), the scaffolds appeared as a random fibre mat characterized by a homogeneous matrix with fibre diameters equal to 1.19 ± 0.13 um.

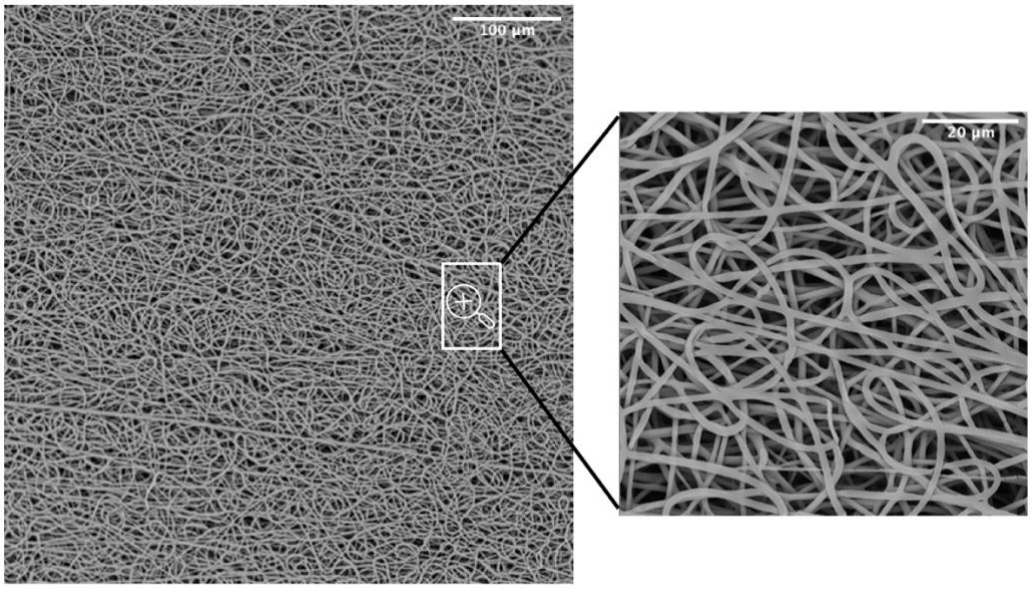

Figure 38 Fibers details from the SEM micrograph of the PolyBS graft.

A common challenge in tissue engineering is the difficulty of obtaining highly bulk-cellularized scaffolds due to intrinsic scaffold limitations such as insufficient pore size or interconnectivity. High porosity, pore interconnectivity, and large surface area to volume ratio of electrospun scaffolds dictate the extent of cellular infiltration and tissue ingrowth into the scaffold. Furthermore, they influence a range of cellular processes and are crucial for the diffusion of nutrients, metabolites, and waste products. We evaluated pore sizes using the ImageJ software, by measuring the

area of thousands of pores and porosity was calculated as a difference between the predicted scaffold density and the polymer density (gravimetry). The results showed an 88.6 ± 0.9 % porosity and a maximum pore size of 15.2 um (Table 4). The SEM analysis was also utilized to evaluate the potentially dangerous interaction with ethanol and gas plasma utilized to sterilize the scaffolds for in vitro experiments. The revealed quality of the microstructure demonstrated no morphological modifications.

Table 4 Porosity, inner diameter, and wall thickness calculated from the uCT data, pore size and fibre diameter calculated from SEM and kink resistance.

Porosity	Inner Diameter	Wall Thickness	Max Pore Size	Fiber Diameter	Kinking Resistance
88.6 ± 0.9%	2.62 ± 0.08 mm	490 ± 20 μm	15.2 μm	1.19 ± 0.13 μm	84°

Surface properties evaluation of the electrospun graft

The water vapour transmission rate (WVTR) of the graft was evaluated, both at 25 °C and 38 °C, according to the American Society for Testing and Materials (ASTM) standard. The result showed a linear increase of WVTR between 0 and 600 s and then the value remained constant. The WVTR after 10 min are remarkable, 14000 $g/m^2 \cdot 24$ h at 38 °C and 6500 $g/m^2 \cdot 24$ h at 25 °C (Figure 39-a).

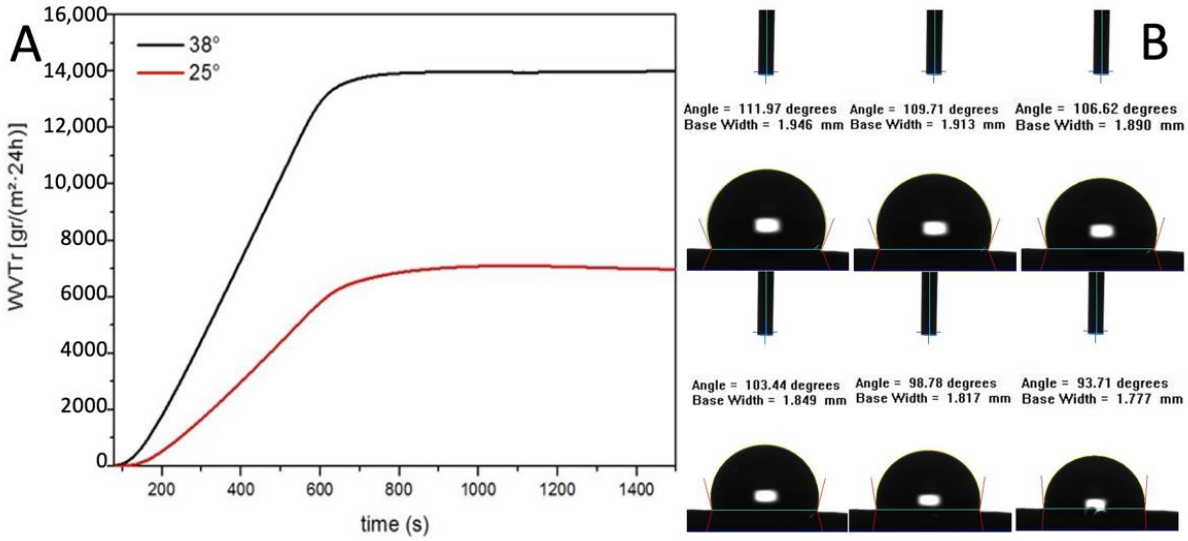

Figure 39 a) Water vapour transmission rate evaluation of PolyBS grafts, b) Contact angle measurements of PolyBS grafts.

As reported by Xu et al., a medium permeability membrane, WVTR 2000 g/m^2·24 h, provides the optimal local environment to promote the proliferation and functions of fibroblasts [110]. The resulting value of WVTR is three times higher than their highest value of permeability membrane which was considered extremely high. This data is also confirmed by the contact angle dynamic measure (Figure 39-b). Indeed, the water contact angle of the electrospun graft started at 114° indicating a hydrophobic surface and then decreased gradually since the surface is permeable to water. Taken together, the data on the contact angle and the WVTR studies suggest that the PolyBS graft should allow the physiological diffusion of metabolites through the tubular wall (Table 5).

Table 5 Parameters obtained from WVTR and contact angle analysis of PolyBS grafts.

WVTR $g/m^2 \cdot 24\ h\ 25°$	WVTR $g/m^2 \cdot 24\ h\ 38°$	Contact Angle t = 0 s	Contact Angle t = 1800 s
6500	14,000	114°	93°

Stability in physiological-like environments

The degradation test was performed in three different buffer solutions to mimic the physiological environment of different human tubular conduits. Bile is the common fluid present inside the bile ducts, used to digest lipids. It is a basic solution composed of water, salts, and bilirubin. It was selected to evaluate the degradation of PolyBS graft as an artificial bile duct for biliary reconstruction.

Plasma is the intravascular part of extracellular fluid without blood cells. Indeed, it was used to evaluate the degradation of PolyBS as an artificial vascular substitute. Lastly, phosphate-buffered saline was used to evaluate the hydrolytic resistance of PolyBS scaffolds. The results, in Figure 40 a-b, showed no remarkable difference in the degradation of these grafts up to one month.

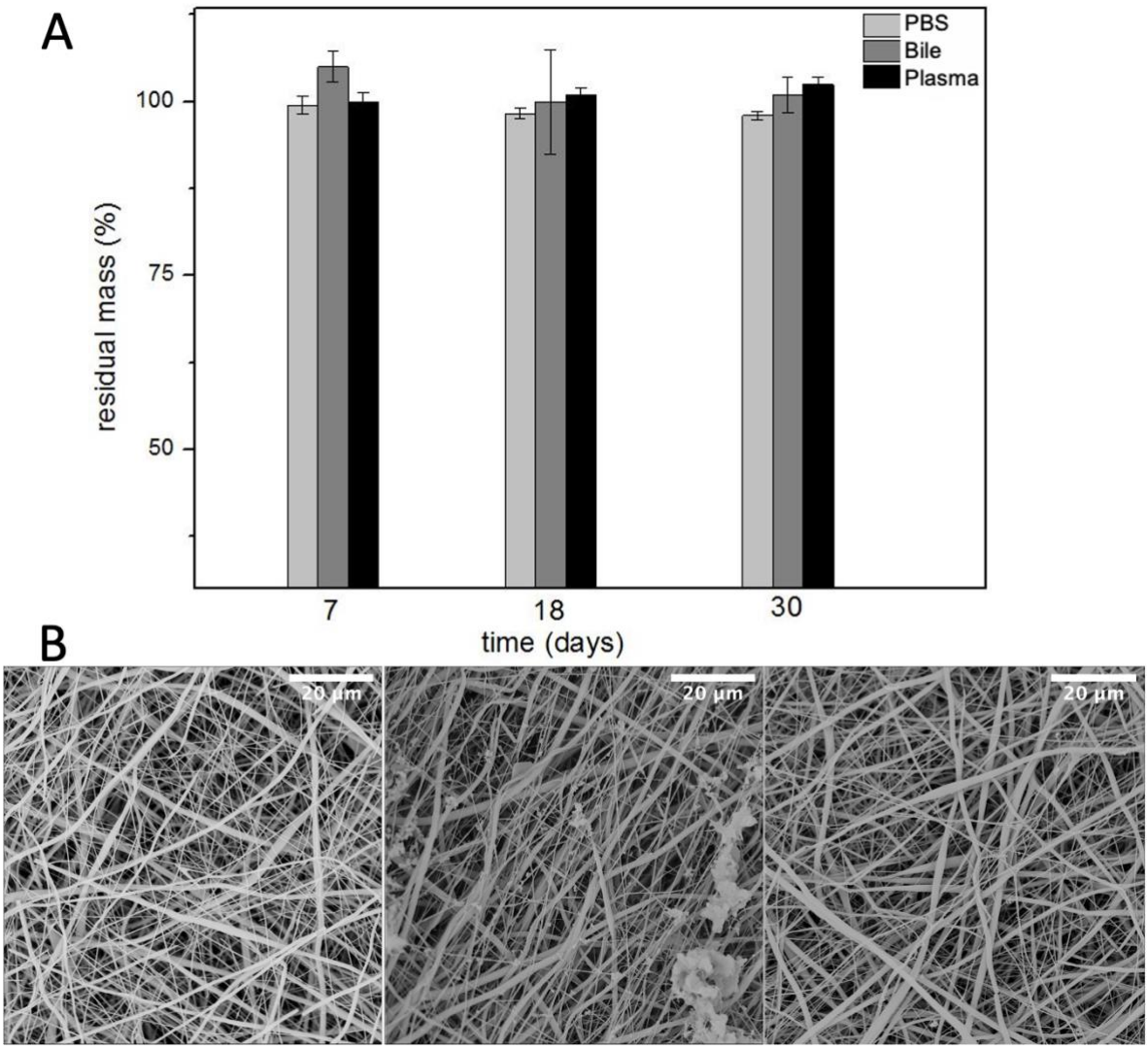

Figure 40 a) Residual mass, b) SEM micrographs of electrospun PolyBS after degradation in PBS (left), bile (centre), and plasma (right) (n = 5).

This would likely help the host remodelling mechanisms to gradually replace the scaffold with native tissue while the scaffold provides mechanical integrity over an extended period.

Mechanical properties

Mechanically, these PolyBS grafts showed a stress-strain curve, at room temperature and dry conditions, characterized by an initial linear region between 0 and 18% strain and a plastic region until rupture occurs. Indeed, these grafts retain their geometry and properties upon short-term mechanical conditioning when traction is applied longitudinally (Figure 41 a-b). It is crucial to withstand physiological pressures without experiencing permanent deformation or bursting.

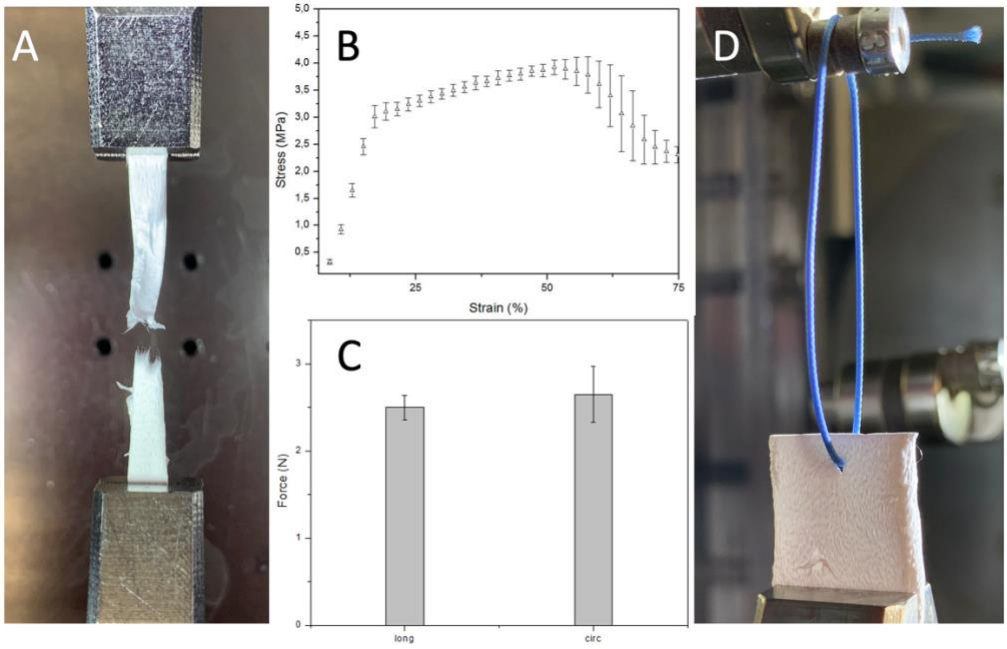

Figure 41 a) Sample detail after failure, b) Uniaxial stress-strain curve (n = 3), c) Uniaxial suture retention force (n = 3), d) Sample details of PolyBS graft before suture pullout.

The elastic modulus, obtained by dividing young stress (YS) 3.1 ± 0.1 MPa by young strain (YN) 17.7 ± 1% in the elastic region, is 17.5 ± 1.6 MPa. Which is stiffer than the

native soft tissue like other aliphatic polyesters such as poly (glycolic acid), poly (L-lactic acid), and their copolymers. Nevertheless, it could be adjusted to the desired range inducing anisotropy by regulating the mandrel rotation or designing a multilayer graft that combines the properties of different synthetic or natural materials. Both these solutions will have a significant implication on the mechanical properties giving us the possibility to tune them based on the application. The region between 17.7 ± 1 and 57 ± 4.5% strain is where strain hardening, caused by the alignment of polymer chains in the direction of the load, prevailed. Indeed, this is the reason why stress increased, after yield stress, until necking occurred. The ultimate tensile strength, the highest engineering stress the material can endure, is 3.95 ± 0.17 MPa. Instead, strain to failure (STF) indicates how much the material has stretched when necking overtakes strain hardening 57 ± 4.5%. Necking is when one region of the sample becomes thinner than the rest concentrating the stress.

The Suture retention force, in Figure 41 c-d, was 2.5 ± 0.14 N when the force was applied on the longitudinal axe of the graft and 2.65 ± 0.32 N when the force was applied on the circumferential axe. This result is consistent with the SEM analysis result that underlines the random fibre orientation. Suture retention strength is crucial for an implanted graft to withstand the tension at the anastomosis. The generally accepted minimum requirement for the suture retention force for a small-diameter graft is 2 N. The SRF of the PolyBS graft prepared in this study was higher than this standard and then autologous substitutes like human saphenous vein (1.81 ± 0.02) and internal mammary arteries (1.4 ± 0.01) [66].

These characteristics, reassumed in Table 6, suggest that the PolyBS graft may represent an attractive biomaterial for tissue engineering applications.

Table 6 Parameters obtained from uniaxial tensile test and suture retention test.

E	UTS	STF	SRF	YS	YN
17.5 ± 1.6 MPa	3.95 ± 0.17 MPa	57 ± 4.5%	2.5 ± 0.14 N	3.1 ± 0.1 MPa	17.7 ± 1%

Furthermore, since it is possible to reproducibly control the anisotropy of electrospun PolyBS by varying the rotational speed of the mandrel, fibre orientation end consequent mechanical properties could be tailored to that of the vessel targeted for replacement.

In vitro cytocompatibility and haemolytic studies

Cell's interaction with the graft was evaluated in static conditions up to 72 h. The scaffold's structure was designed to imitate the composition of the ECM to promote cell growth. Indeed, the results showed a proliferation of normal human fibroblasts after three days. The samples were washed several times to remove non-viable cells and then fixated in formalin and stained with DAPI to acquire reflectance images of the numbers of cells/mm^2 (Figure 42-a-b).

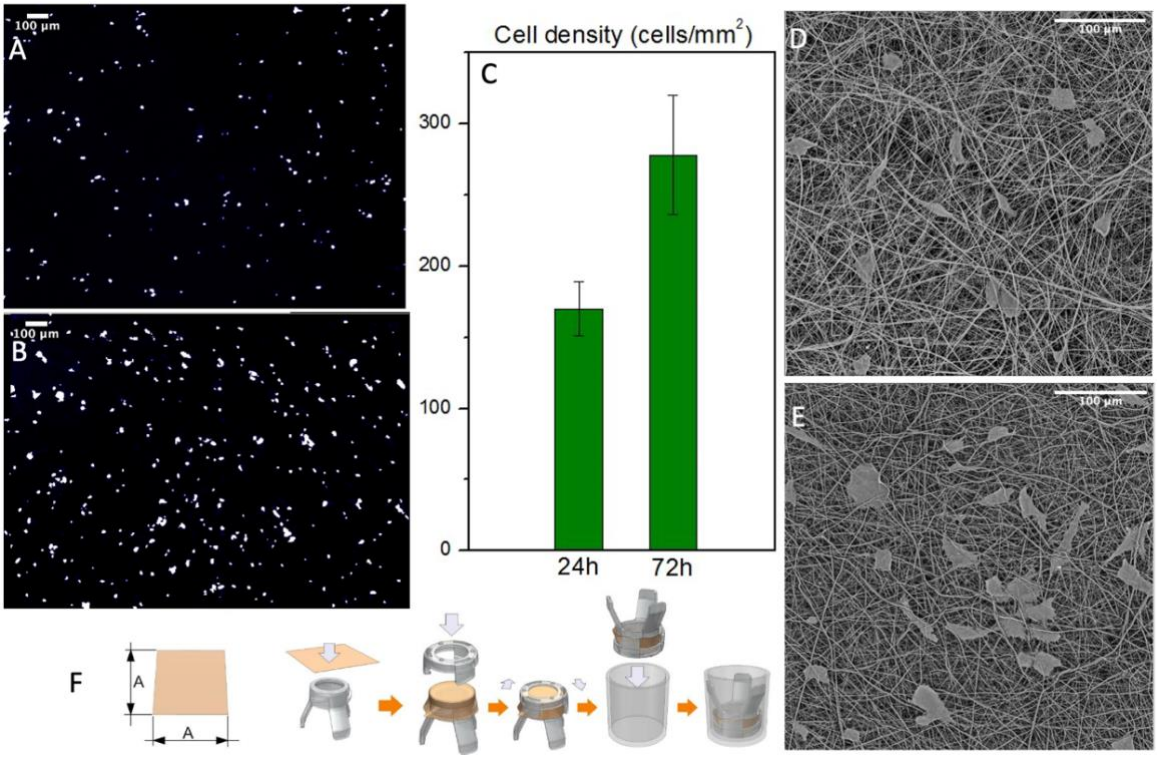

Figure 42 a,b) NHDF nuclei when stained with DAPI after 24 and 72 h respectively, c) Cell density count with ImageJ of the stained nuclei (n = 3), d,e) SEM micrographs of the cultured scaffold after 24 and 72 h respectively, f) Mounting process of the scaffolds on Scaffedex supports.

Then these images were processed on ImageJ software to automatically count the nuclei spots. The results showed a remarkable increase in cell density that underlines the cytocompatibility of the produced PolyBS grafts. Since this technique gives us only an indication of the cell's number, we processed the samples with hexamethyldisilazane to completely remove water. They were then analyzed with SEM to evaluate the cell's morphology and their interactions with the fibre mats (Figure 42-d-e). The dehydration process modified the cell's morphology and removed several cells, but it gives us an overview of the cell's orientation and interaction with the fiber mats confirming the cytocompatibility of the produced PolyBS grafts. Furthermore, both analyses showed no cells inside the graft's wall or

on the outer surface, confirming that this scaffold morphology acts as a barrier for cell infiltration, without preventing its adhesion.

The presence of certain materials can negatively affect red blood cells and destroy their cell membrane causing the release of haemoglobin into the solution [111]. Haemolysis rate was measured using a colourimetric assay of released haemoglobin from red blood cells. The lowest degree of haemolysis, the absorbance of 0.042 ± 0.0012, was provoked by negative controls containing PBS with the addition of diluted whole blood. The highest was provoked by the positive control group, 2% Triton X 100 in pure water, where the absorbance of released haemoglobin reached the value of 0.24 ± 0.05. The absorbance of released haemoglobin provoked by the electrospun sample is 0.045 ± 0.00073, which is very similar to the negative control (Figure 43-a). Blood cells, attached to the fibre mat are shown in Figure 43-b.

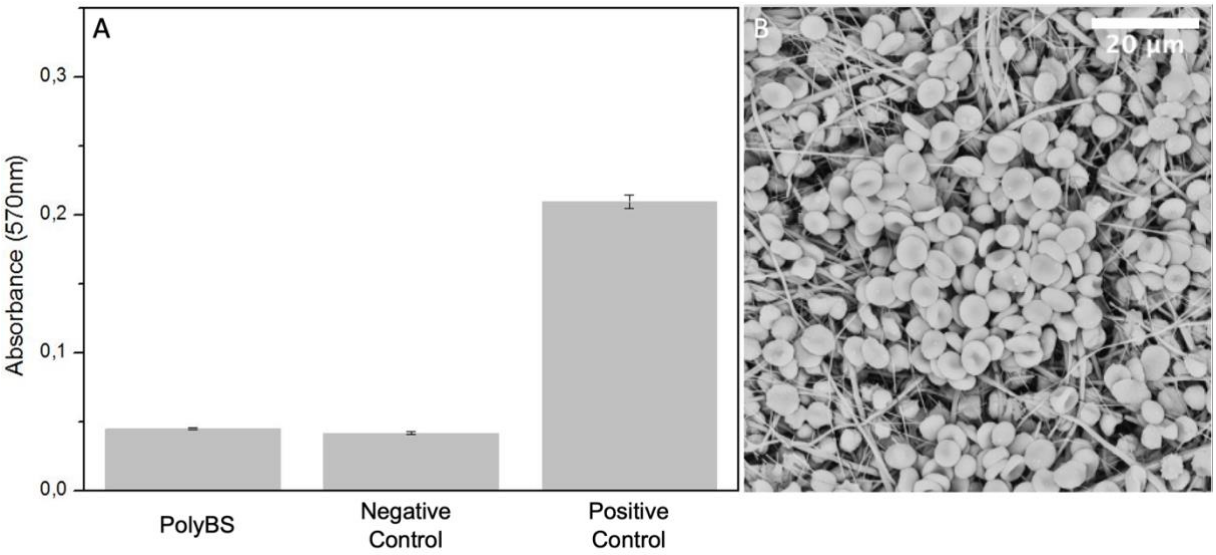

Figure 43 a) Measured absorbance after haemolysis assay in positive control group, negative control group and electrospun PolyBS (n = 5), b) SEM micrograph of electrospun PolyBS after incubation with diluted whole blood.

The degree of haemolysis (%) can be expressed according to the following formula:

$$\%\ \text{haemolysis} = \frac{(Ts - Tn)}{(Tp - Tn)} x\ 100$$

where *Ts* is the average absorbance of the test sample group, *Tn* is the absorbance of the negative control group and *Tp* is the absorbance of the positive control group. The degree of haemolysis of blood-contacting materials must be <5% according to ISO 10993-4:2002 standard and ASTM F756-00(2000). Therefore, our electrospun PolyBS is considered a non-haemolytic material since the resulting value is 1.8 ± 0.4%.

In vivo studies

The biocompatibility and tissue regenerative properties of a PolyBS microfibrous scaffold were assessed in vivo. To this end, the experiments were conducted on nine male New Zealand White rabbits to evaluate the healing of two calvarial bone defects (Figure 44-a).

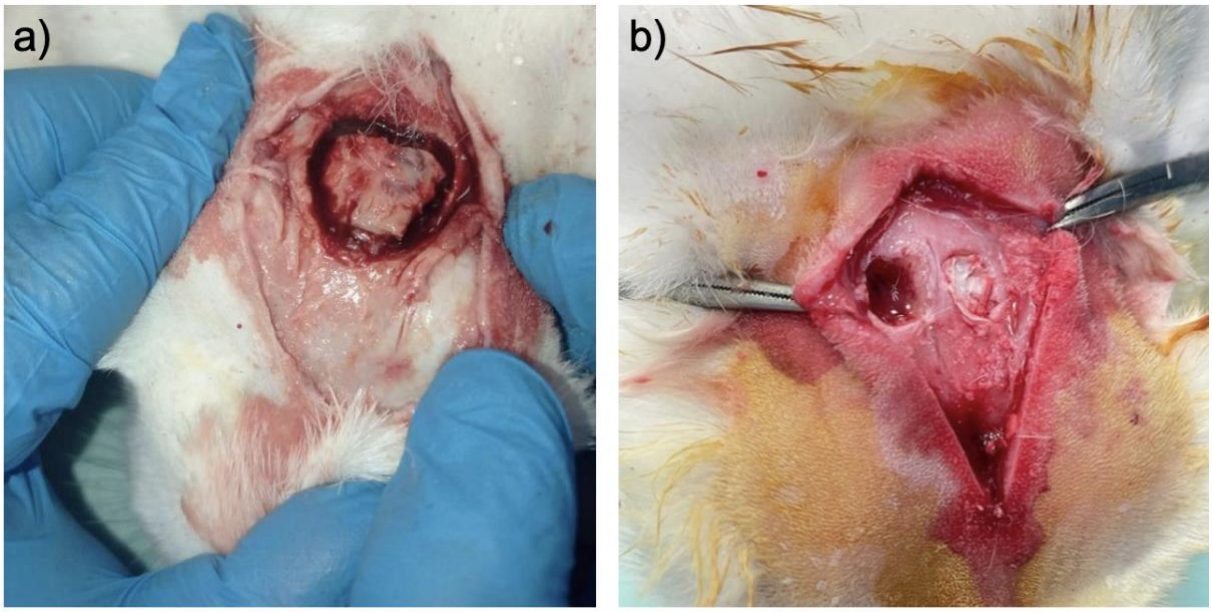

Figure 44 a) Sampling of the frontal bones, b) Scaffold implantation into the frontal bone defect

One defect was allowed to heal naturally while the other was treated with the scaffold (Figure 44-b). The rabbits were observed throughout the study period and various healing parameters, including bone regeneration, inflammation, and tissue integration were recorded.

The evaluation of bone formation was conducted employing computed tomography (CT) scans, at intervals of 4 (Figure 45-a), 12 (Figure 45-b), and 24 (Figure 45-c) weeks.

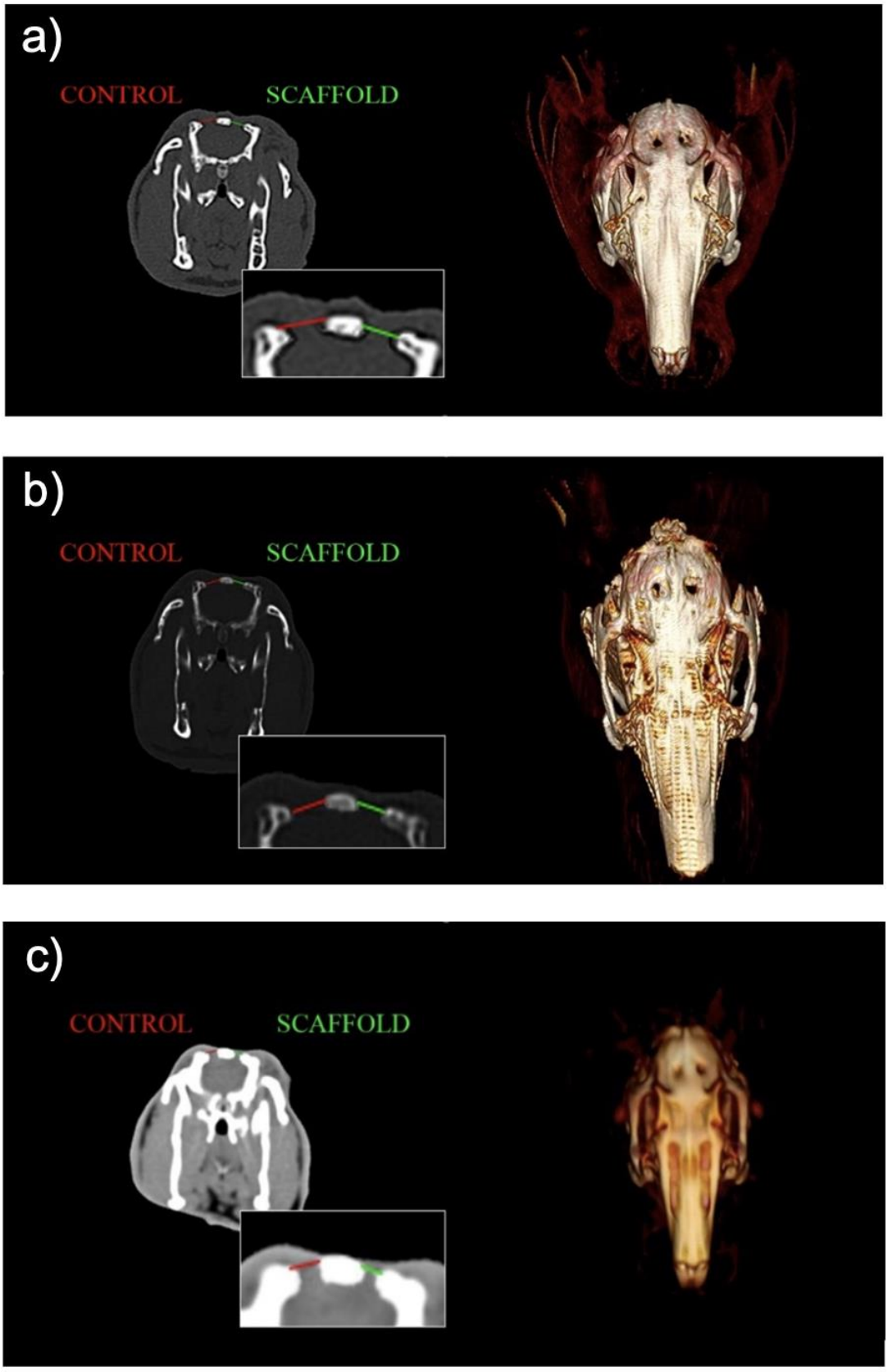

Figure 45 Comparison of treated vs untreated bone defects after 4 (a), 12 (b), and 24 (c) weeks using CT scan and 3D reconstruction in coronal view.

Upon examination during the last follow-up, both untreated and scaffold-treated defects showed incomplete healing. However, notable differences were observed in the evaluation of the area covered by mineralised tissue, which is in accordance with similar studies [89,112]. The untreated defect displays bone infiltration along the periphery and a large void in the centre. Conversely, the implantation of the scaffold led to a greater amount of mineralized tissue infiltration, encompassing almost the entirety of the scaffold's surface. The follow-up assessments at 4, 12, and 24 weeks demonstrated a gradual improvement in both the healing process and the penetration of mineralized tissue into the scaffold. Examining the bone sections of the defect, the histological evaluation confirmed the absence of inflammatory infiltrates around the scaffold. Upon analysis at the 24-week mark, it was observed that both the control and scaffold-treated defects exhibited two partially healed defects, accompanied by a reduction in parietal thickness in each case. In the untreated defect, a region of bone remodelling was visible in the haematoxylin-eosin sections. The area exhibited poorly mineralized, thinned, and fragmented trabeculae that contained multiple areas of osteonecrosis (Figure 46-a).

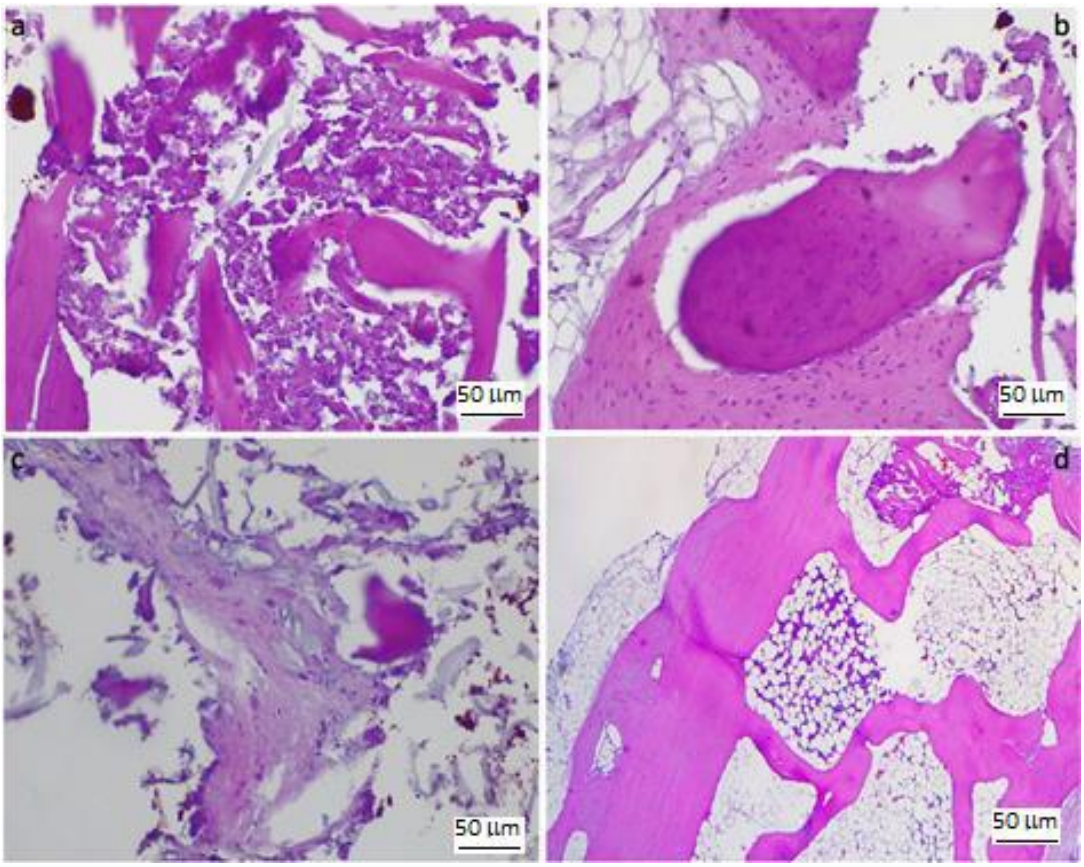

Figure 46 a) Osteonecrosis in H&E stain of treated bone defect 24 weeks post-implant (magnification: 20X); b) Bone deposition and necrotic bone fragments in H&E stain of treated bone defect 24 weeks post-implant (magnification: 20X); c) Periosseous tissue with embedded amorphous fragments (scaffold); d) Bone marrow with hematopoietic stem cell niches.

The medullary cavities consisted of exclusively adipose marrow. Conversely, the defect that was treated with the scaffold showed not only some sections of dead bone tissue with thin and poorly mineralized bone layers but also multiple sections where bone was being formed and many active osteoblasts were present (as shown in Figure 46-b). There are also fragments of birefringent amorphous material, which may be scaffold residues (Figure 46-c). We also note the presence of residual medullary cavities with clearly visible haemopoietic niches (Figure 46-d).

The presence of periosteal fibrous tissue is indicative of a robust osteosynthesis process. Additionally, numerous activated osteoblasts signify an advanced stage of bone regeneration. Furthermore, the haemopoietic niches point towards increased bone maturation.

The results of the immunohistochemical analysis demonstrate a remarkable positivity for CD56 at the point of transition between healthy bone and the 'fracture zone', a clear indication of significant osteoblastic proliferation occurring within the defect Figure 47.

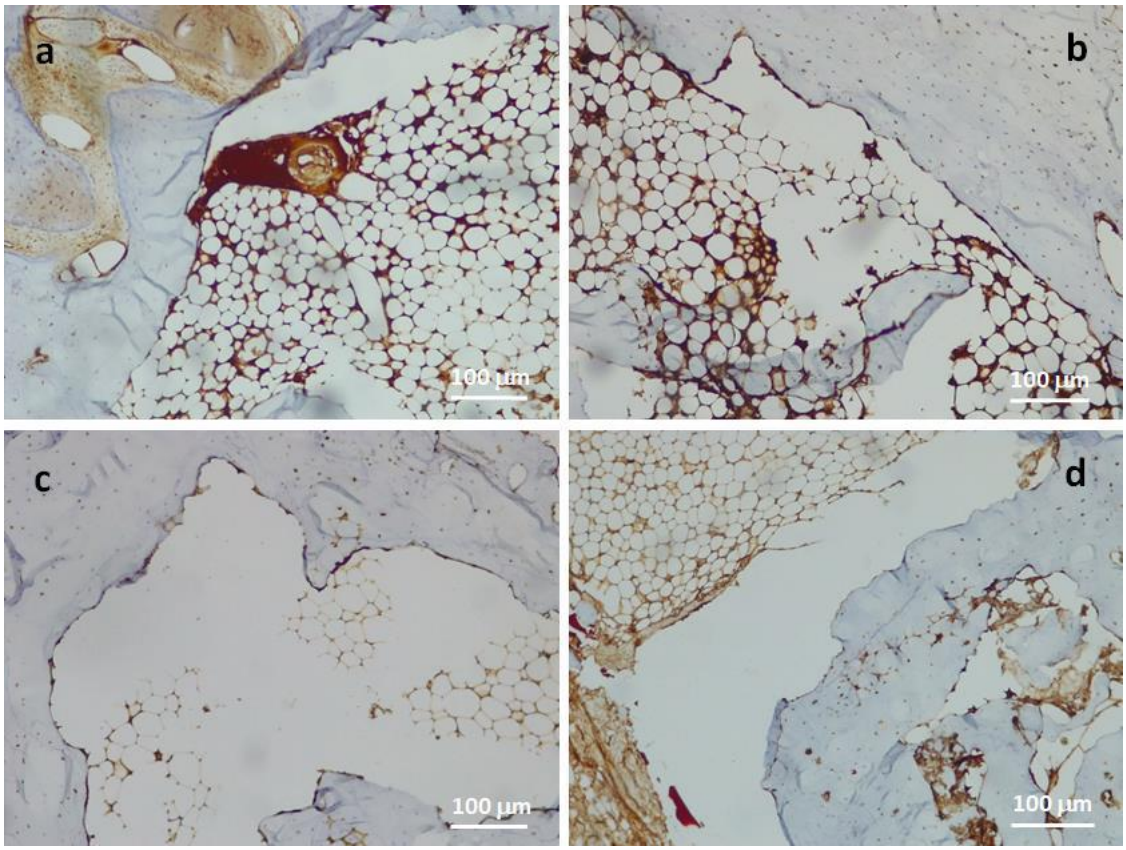

Figure 47 Activated osteoblasts with CD56 as an immunohistochemical marker at 24 weeks post-implant are related to scaffold-treated specimens (a,b) and control (c,d). Magnification is 10X.

The findings of this study confirmed that the PolyBS microfibrous scaffold is biocompatible and possesses significant potential for tissue regeneration. In comparison to defects undergoing natural healing, the defects treated with the scaffold displayed a marked increase in both bone regeneration and tissue integration.

4. Experimental section

4.1 Synthesis, Characterization, and Processing of Highly Bioadhesive Polyurethane Urea as a Microfibrous Scaffold Inspired by Mussels

Materials

Dopamine hydrochloride (DA-HCl), di-tert-butyl dicarbonate ($(Boc)_2O$), sodium bicarbonate ($NaHCO_3$), 1-ethyl-3-(3-dimethyl aminopropyl) carbodiimide hydrochloride (EDC-HCl), triethylamine (TEA), dimethylformamide DMF-d7, chloroform-d, dimethyl sulfoxide DMSO-d6, polyethylene glycol 1000 Da (PEG), ε-caprolactone (ε-CL), lithium bromide (LiBr), diethylamine (DEA), standards of PEG, sodium azide (NaN_3), Dulbecco's phosphate buffered saline (DPBS), L-Lysine hydrochloride, N-hydroxysuccinimide (NHS), Tetrahydrofuran (THF) and ethyl acetate (EA), were purchased from Merck (Germany).

Calcium hydride (CaH_2), stannous octoate ($Sn(Oct)_2$), 1,4-diisocyanatobutane (BDI) were purchased from Fluka (Italy) and used without further purification.

Dimethyl-formamide (DMF), diethyl ether, dichloromethane (DCM), toluene, methanol, 2-propanol and acetone, were purchased from VWR (Italy) and used without further purification.

Dulbecco's modified Eagle's medium (DMEM), fetal bovine serum (FBS), trypsin, l-glutamine, penicillin, streptomycin and amphotericin were purchased from Euroclone group (Italy).

Apparatus

Hydrogen nuclear magnetic resonance (1H-NMR) spectrum was recorded using a Bruker Avance II 300 MHz instrument at room temperature in DMSO-d6 for LDA, DMF-d7 Polyurethanes urea (PUUs) and Chloroform-d for PCL-PEG-PCL.

Fourier transform infrared spectroscopy analysis in total attenuated reflectance (ATR-FTIR) was performed using a Bruker Alpha instrument in a wavenumber range of 400 to 4000 cm-1 at room temperature on KBr tablets.

Ultraviolet (UV) measurements were performed using a spectrophotometer. UV-visible spectra were recorded with a Shimadzu UV-2400 spectrophotometer.

The analysis of size exclusion chromatography (SEC) was conducted with an Agilent 1260 Infinity multi-detector GPC/SEC system. The elution was performed on a Phenogel 5 µm with a 103 Å pore size column using LiBr/DMF 0,025 M as a mobile phase at 50°C, with a flow rate of 0.8 ml/min. Standards of PEG were used for calibration.

Differential scanning calorimetry (DSC) measurements were performed using a DSC 131 EVO, SETARAM Instrument. Samples were weighted and hermetically sealed in aluminium pans and heated from -50°C to 150°C with a heating rate equal to 5°C/min to measure melting (Tm) and glass (Tg) transition temperatures.

The hydrophilicity was studied by a video contact angle instrument FTA 1000 C class, First Ten Angstroms.

Rheological experiments were carried out using a DHR-2 oscillatory rheometer TA INSTRUMENTS equipped with a self-heating Peltier plate. The geometry used for all tests was a parallel flat plate device with a diameter of 20 mm.

The heat required to generate spot melting on the PU-LDA films was produced by irradiating with a GBox diode near-infrared (NIR) laser (λ: 810 nm).

Adhesive testing was performed, by tensile measurements, in lap shear configuration using a Bose TA Instruments ElectroForce Test Bench System.

The microfibrous scaffold was produced by 3D printing using a BioAssemblyBot 400.

Scanning electron microscopy (SEM) images were acquired with a Phenom PRO X instrument.

Synthesis of PU-LDA and chemical-physical characterization

The triblock copolymer PCL-PEG-PCL was synthesized by Ring-Opening Polymerization (ROP), setting a molar ratio between ε-CL and PEG equal to 30.

Before the reaction, ε-CL was distilled at 65°C with calcium hydride (CaH_2) under vacuum and PEG was dehydrated by azeotropic distillation in toluene at 76° C and room pressure.

The copolymer synthesis was carried out at 130°C for 24 hours, with $Sn(Oct)_2$ as the catalyst, in an argon atmosphere. Then the product was purified by dropwise precipitation in cold diethyl ether under stirring, then washed in 2-propanol and kept at 4°C overnight. Finally, the product was dried under vacuum resulting in a white powder. Copolymer was characterized by FTIR, ^{1}H-NMR and UV-Vis.

Lysine-dopamine (LDA) was synthesized from L-Lysine HCl (LYS) and dopamine HCl. LYS was dissolved in the mixed solvent distilled water/THF and $NaHCO_3$ was added. Then di-t-butyl dicarbonate (Boc anhydride) was added dropwise, the reaction was carried out at 30 °C for 24 hours under a nitrogen atmosphere. A rotary

evaporator was used to remove the solvent and HCl aqueous solution was added dropwise until lysine precipitation occurred. After that, it was extracted with ethyl acetate and then the solvent was removed with the rotary evaporator.

The Boc-Lysine (BL) synthesized in the previous step was dissolved in dichloromethane then N-hydroxysuccinimide (NHS) was added into the round bottom flask and cooled at 0°C. 1-Ethyl-3-(3-dimethyllaminopropyl) carbodiimide hydrochloride (EDC-HCl) was dissolved in the DCM and after 30 minutes the reaction was warmed to room temperature and allowed to proceed for another 6 hours under a nitrogen atmosphere. Pure water was used to wash the solution 3 times, then the solvent was removed with the rotary evaporator.

The Boc-lysine-NHS (BLN) synthesized above was dissolved in methanol and an excess of dopamine hydrochloride (dopamine-HCl) was added. After the dopamine-HCl dissolved, triethylamine (TEA) was added into the solution and the reaction proceeded for 12 hours at room temperature under a nitrogen atmosphere. Then the solvent was removed with the rotary evaporator. Ethyl acetate was applied to dissolve the product, followed by washing with deionized water 3 times. The ethyl acetate was removed, and the product was dried overnight.

The BLDA synthesized in the previous step was dissolved in HCl/ethyl acetate solution and the reaction was carried out for 6 hours at room temperature under a nitrogen atmosphere. Then, the solvent was removed with the rotary evaporator and the final product lysine-dopamine (LDA) lyophilized. Reaction intermediates and final product were characterized by FTIR, ^{1}H-NMR and UV-Vis.

LDA was utilized to obtain PU-LDA, allowing the chain extension, and lysine was used for PU-LYS as the control group for comparison.

The triblock copolymer PCL-PEG-PCL was dissolved in anhydrous DMF in a round bottom flask, then 1,4-diisocyanatobutane (BDI) was added and the reaction was carried out for 2 hours at 70°C, under argon, in the presence of $Sn(Oct)_2$ as catalyst. Then, the chain extenders LYS or LDA were dissolved in anhydrous DMF and DEA was added. This solution was added dropwise into the reaction round bottom flask and carried out at 25°C for 20 hours. The product was purified by dropwise precipitation in cold diethyl ether under stirring and washed 4 times in 2-propanol. Finally, the product was dried under vacuum resulting in a white powder for PU-LYS and a pink powder for PU-LDA. The stoichiometry of the reagents was set at 1:2,3:1 of PCL-PEG-PCL:BDI: LYS/LDA. Polyurethanes were characterized by FTIR, ^{1}H-NMR, SEC, and DSC. The amount of dopamine inserted on the PU-LDA derivative was quantified by UV-Vis, by using LDA as standard.

Film casting procedure, hydrolysis studies, swelling and contact angle measurements

The synthesized polymers were dispersed in chloroform at room temperature (30% w/v). The solutions were poured onto polytetrafluoroethylene (PTFE) moulds and allowed to dry at room temperature inside a drier. Initial solution volumes were selected to obtain a 0.5mm thickness of PUs films. The hydrolysis study on polyurethane films produced by film casting was carried out in DPBS pH 7.4, with 0.02 % of sodium azide, at 37° C in a 48-well plate placed inside an incubator. Polyurethane films produced by film casting were cut into 1cm^2 disks, washed in

distilled water, lyophilized, and weighed (W_0). The solution was replaced weekly, and the weight loss was measured at scheduled time intervals of up to 6 months. At each time point, the samples were washed four times in ultra-pure water and lyophilized. The hydrolysis experiments were performed in triplicate, and results were expressed as the mean value of recovered weight ± standard deviation. Results were plotted against t_0.

The swelling ability of the films was tested after incubation in DPBS pH 7.4 for up to 14 days in a 48-well plate placed inside an incubator. Polyurethane films produced by film casting were cut into 1cm^2 disks and weighed (W_0). At each time point, films were withdrawn and weighed, after gently removing the liquid that covered the external surface with soft filter paper. To quantify swelling behaviour, the swelling ratio was calculated using the following equation:

$$Swelling\ ratio = \frac{(W_s - W_0)}{W_0} \times 100$$

where W_0 is the dry weight of the polymeric films and W_s denotes the weight of films after swelling. Each experiment was performed five times.

The hydrophilic behaviour of the polyurethanes was analysed by contact angle measurements. Deionized water was dropped onto the surface of both PU-LYS and PU-LDA and an image of the drop was recorded. The software was used to calculate the contact angle, at scheduled time intervals, up to 10 minutes. The contact angle experiments were performed in triplicate at room temperature, and results were expressed as mean value ± standard deviation.

In vitro cytocompatibility studies

Human Dermal Fibroblasts-Adult (NHDF–Ad) were obtained from Lonza bioscience and used after 7 doublings. The cell line was grown in the minimum essential medium [Dulbecco's modified Eagle's medium (DMEM)] supplemented with 10% (v/v) fetal bovine serum (FBS), 2 mM l-glutamine, 100 U/mL penicillin, 100 µg/mL streptomycin, and 2.5 µg/mL amphotericin B (all reagents were from Euroclone, Milan, Italy) under standard conditions (95% relative humidity, 5% CO2, 37 °C). The cells were seeded in flasks at 2.5×104 cells/cm^2 and allowed to grow until confluence.

Films produced as described in paragraph 2.4, were sterilized with 75% alcohol and ultraviolet light irradiation. Then, were transferred into a 48-well tissue culture polystyrene plate and 500 ml cell suspension (about 30 000 cells per well) was used for culture seeding.

Indirect cell viability in the presence of PUUs disks was assessed by an 3-(4,5-dimethylthiazol-2-yl)-5-(3-carboxymethoxyphenyl)-2-(4-sulphophenyl)-2H-tetrazolium (MTS) assay, using a commercially available kit (CellTiter 96 Aqueous One Solution Cell Proliferation assay, Promega) containing MTS and phenazine methosulfate (PMS).

At each time point, the supernatant was removed, and each well was washed with sterile DPBS. After this, cells in each well were incubated with 500 µL of fresh DMEM and 100 µL of an MTS solution, and plates were incubated for 2 h at 37 °C. 100 µl of the solution in each well was transferred into a 96-well flat plate. The absorbance at 490 nm was read using a Microplate reader (Multiskan Ex, Thermo Labsystems, Finland). Relative cell viability (percentage) was expressed as (Abs490 PU-LDA

cells/Abs490 PU-LYS cells) × 100, based on three experiments conducted in multiple of four. Cells incubated with the medium were used as the negative control.

Moreover, acridine orange/ethidium bromide (AO/EB) double staining was performed to confirm MTS results.

Direct cell viability was performed, in triplicate, by directly seeding cells (5x104, 50µl) on PUU disks in a 48-well plate. After 30 minutes 500 µl of DMEM was added and cells were cultured for 7 days, then the discs were washed with DPBS and stored in 4 % formaldehyde for 30 min at 4 °C. Dehydration was performed with mixtures containing increasing amounts of ethanol (15, 30, 50, 75, 100 %) and the films were stored in the dryer until SEM analysis.

Adhesion evaluation

Tack test

Tack test measurements were performed with a DHR-2 TA Instrument rotational rheometer with a Peltier plate cartridge using a 20mm upper plate. For tack test adhesive strengths experiments, PU-LDA obtained by film casting was placed between the bottom and the upper plate and kept at 55 °C for 15 minutes, until a complete melting occurred. The gap was set at 300 µm and, following a conditioning period of 60 seconds at 37 °C or 25 °C, it was linearly increased up to 450 µm at 0.5 µm/s. These tests were all performed in tension mode to evaluate the tendency of these materials to form a connection to a substrate after melting. All measurements

were performed at 37 °C and 25 °C in triplicate and results were expressed as the mean value.

NIR-induced film fusion procedure and lap shear tests

Lap-shear experiments were conducted on aluminium, glass, polypropylene and porcine skin at room temperature and dry conditions to evaluate adhesive strength. Further tests were conducted on porcine skin in wet conditions and at 37°C submerged in water to evaluate the interaction with biological tissue. Each specimen was cut into a rectangular shape, 7.50 cm long and 2.5 cm wide. As a general procedure to allow the PU-LDA to melt, a NIR irradiation procedure was applied. The PUUs films were weighted, placed onto the specimen, and irradiated with a NIR laser from a distance of 15cm until melting occurred. PU-LDA required less than 60 seconds at 4W/cm^2 and PU-LYS 7.5W/cm^2 for 120 seconds. The film (1 cm^2) was first fused by NIR irradiation on the surface of a single porcine skin specimen then a second specimen was rapidly overlapped 2.5 cm in a lap shear configuration with the specimen where the PU was fused and 200g weight was placed on top of them for 5 minutes. For dry measurements, no further preparation was needed, and mechanical testing was performed, by tensile measurements. The wet condition was made by submerging in DPBS for 2 minutes the overlapped porcine skin. The analysis at 37°C was conducted by submerging the overlapped porcine skin already mounted on the heated tensile system. The load was incremented stepwise until failure occurred. The adhesive strength was obtained by dividing the maximum load (N) observed by the area of the adhesive overlap (m^2), giving the lap-shear adhesion in Pascals (Pa =

N/m^2). These experiments were performed in triplicate, and results were expressed as mean value ± standard deviation.

Rheology

To perform rheological studies DHR-2 TA Instrument rotational rheometer with a Peltier plate cartridge and 20mm upper plate was used. PU-LDA films, obtained by solvent casting, were used for the analysis. Before carrying out each experiment, the sample was conditioned for 60 seconds at the analysis temperature. The flow sweep experiment was conducted by applying a range from 0.01 to 100 s^{-1}. The time sweep measurements were conducted at a constant temperature, constant strain (1%) and constant frequency (10 rad/s) for 600 seconds. All these analyses were performed at constant temperatures, at 80, 75, 70 and 65 °C. Moreover, the time sweep measurements were conducted in 2 steps by applying a constant strain of 1% and a constant frequency of 10 rad/s. The first step was at 80 °C for 120 seconds and the second step was at 37 °C for 1200 seconds.

The measurement gap was set at 200 µm for all analyses. All experiments were conducted in triplicate, using a 20 mm parallel plate, and results were expressed as the mean value.

Thermo-rheological experiments were conducted in 2 steps, cooling down the sample from 80 to 25 °C and after heating it again to 80 °C at a rate of 1 °C/min by applying a constant strain of 1% in the linear viscoelastic region and a frequency of 10 rad/s.

3D Printing Processing

PU-LDA was melted at 80°C inside a heat-controlled print head equipped with a 23-gauge needle to produce 300 μm filaments. The deposition was performed with a constant pressure of 75 psi on a heated glass surface at 50°C. We chose two different patterns to evaluate different fibre diameters and shape fidelity to the digital model.

Statistical analyses

All reported values are means with error bars corresponding to standard deviation. A paired sample Student's t-test was used to identify differences in lap shear tests. Two-way ANOVA was performed on the porcine skin experiments in lap shear configuration. Statistical significance was determined by p-values < 0.001.

4.2 Overcoming the Blood-Brain Barrier: A Novel Approach Using a Conductive Bioadhesive Coating for Voltage-driven Drug Delivery in Glioblastoma Multiforme

Bioadhesive coating fabrication

The PU-LDA powder was dispersed in dimethylacetamide at 60°C under stirring and poly(3,4-ethylenedioxvthiophe): polystyrene sulfonate (PEDOT: PSS) was added (3:1 w/w). After 3 days DI water was added to the dispersion 1:5.5 v/v. The solvent evaporation technique, at 50°C under vacuum overnight, was used to create the rectangular film for dry conductivity measurements and the platinum coatings for wet electrochemical impedance spectroscopy and cyclic voltammetry. The films were produced by pouring the dispersion onto Teflon molds 2.5x1.5 cm. The 1 cm diameter platinum disks were coated with 140um CB.

Conductivity measurements

A two-probe set-up was utilized to measure the conductivity of CB films. Samples were clamped at each end using platinum sheets to connect them to a potentiostat (Multi Autolab/M101, Eco Chemie, Netherlands). Sample resistivity was acquired by extracting the impedance output at 1 kHz from EIS measurements. The conductivity (σ) was derived using the following Equation:

$$\sigma = \frac{L}{R \times A}$$

wherein L = length between the clamps, R = recorded impedance, and A = cross-sectional area of the sample. These experiments were performed in triplicate, and results were expressed as mean value ± standard deviation.

Electrochemical characterization

Electrochemical characterization was assessed by performing electrochemical impedance spectroscopy (EIS) and cyclic voltammetry (CV) using an Autolab potentiostat (Multi Autolab/M101, Eco Chemie, Netherlands). All measurements were conducted using a three-electrode set-up with a platinum wire counter electrode and an isolated silver/silver chloride (Ag/AgCl) reference electrode immersed in Dulbecco's phosphate-buffered saline (Sigma). EIS was measured using a 10-mV sinusoidal voltage at frequencies ranging from 0.1 to 10 kHz. Bode plots of the impedance magnitude spectra and phase shift spectra were analyzed. These experiments were performed in triplicate, and results were expressed as mean value ± standard deviation.

CV curves were obtained by sweeping the voltage between −0.6 to 0.8 V at a scan rate of 150 mV s–1 for a total of 11 cycles and measuring the resulting current. These experiments were performed in triplicate, and the results were expressed as mean values.

Charge storage capacity (CSC) values were computed by integrating the current response of the 10th CV cycle with respect to time. These experiments were performed in triplicate, and results were expressed as mean value ± standard deviation.

Drug delivery device fabrication

A polymeric blend composed of 73% PU-LDA, 24% PEDOT: PSS and 3% Paclitaxel (PTX) was prepared. First PU-LDA and PEDOT: PSS were dispersed in DMAC/water 5.5/1 blend (7% W/V) at 60°C under stirring for 48h. Then, PTX was dispersed in the same solvent blend and added to the polymeric dispersion at 60°C under stirring for 24h. Finally, titanium rods were weighted and dip-coated 8 times in this dispersion every 30 minutes and then dried completely. The final mass coated on these devices was calculated by weighting the final samples and removing the weight of the titanium rods previously collected.

Drug loading evaluation

4 samples were used to evaluate the drug loading dispersing the coating in Acetonitrile/water 65/35. When fully dispersed the solution was centrifuged for 3 minutes at 3500rpm to let the polymer precipitate and the solvent was collected and filtered with a 0.2μm in regenerated cellulose. To quantify the amount of PTX in these solutions we used High Performance Liquid Chromatography (HPLC) mounting a Luna 5u C18 column and performing the elution in Acetonitrile/water 65/35 at 25°C and 1mL/minute at 227nm. The peak of PTX appeared after 5.6 minutes from the start of the elution and its area was calculated and compared with the area of a calibration curve to convert the recorded signal with the amount of drug present in each sample. The resulting drug loading was 2.48% $\pm$ 0.04.

Release study

The release study was conducted at 37°C inside Franz's cells under stirring in 3.5mL 1:1 FBS/PBS buffer. The PTX from the collected buffer was extracted in ethyl acetate (3:1 v/v compared to the buffer) under stirring for 1h and then centrifuged at 3500rpm for 5 minutes to allow a clear separation between the two phases. The ethyl acetate containing PTX was collected and dried. The obtained pellet was then redispersed in Acetonitrile/water 65/35 and analyzed using HPLC as reported in the previous paragraph.

The passive release was evaluated by collecting and replacing the buffer after 10 minutes, 1h, 4h, 24h, 3d, 7d, 8d, 9d, 10d. Instead, the enhanced release was performed by applying a constant voltage of -1V using a potentiostat for 4h and was evaluated by collecting and replacing the buffer after 10 minutes, 1h, 4h, and 24h.

The area of the PTX peak, recorded with HPLC, was compared with the area of a calibration curve to accurately convert the recorded signal into the amount of drug released at each time point. Then, it was divided by the weight of the relative device multiplied by the drug loading to express the result as a % of PTX released from the total PTX loaded.

In vitro cytotoxicity studies

Neuroblastoma cells SH-SY5Y were grown in a 1:1 mix of the minimum essential medium [Dulbecco's modified Eagle's medium (DMEM)] and Ham's F12 medium supplemented with 10% (v/v) fetal bovine serum (FBS), 100 U/mL penicillin, 100 µg/mL streptomycin, and 2.5 µg/mL amphotericin B (all reagents were from Euroclone, Milan, Italy) under standard conditions (95% relative humidity, 5% CO_2, 37°C). The cells were seeded in flasks at 5×10^4 cells/cm^2 and allowed to grow until confluence.

To test the effect of PTX, the cells were transferred into two 96-well tissue culture polystyrene plates and 300 µl cell suspension (around 15 000 cells per well) was used for culture seeding. After 24h 0.1, 0.5, 1, 5, 10, 50, 100, 500, and 1000 nM concentrations of PTX were solubilized in DMSO and added to the growing media (1% V/V). The release of PTX in the growing media was analyzed for both passive and enhanced conditions after 1 and 4 hours. These media were then used to cultivate the cells and compared with the effects of PTX.

Cell viability was assessed by an 3-(4,5-dimethylthiazol-2-yl)-5-(3-carboxymethoxyphenyl)-2-(4-sulphophenyl)-2H-tetrazolium (MTS) assay, using a commercially available kit (CellTiter 96 Aqueous One Solution Cell Proliferation assay, Promega) containing MTS and phenazine methosulfate (PMS). At each time point, the supernatant was removed, and each well was washed with sterile DPBS. After this, cells in each well were incubated with 100 µL of fresh DMEM and 20 µL of an MTS solution, and plates were incubated for 4h at 37 °C. The absorbance at 490 nm was read using a Microplate reader (Multiskan Ex, Thermo Labsystems, Finland). Relative cell viability (percentage) was expressed as (Abs490-MTS /Abs490-MTS) ×

100, based on five experiments. Cells incubated with the medium were used as the negative control.

Ti rods were sterilized with ultraviolet light irradiation for 1h.

The cells were transferred into an 8-well chambered borosilicate coverglass and 600 μl cell suspension (around 20,000 cells per well) was used for culture seeding. After 24h 7 different conditions were tested: the passive release for 1h, the active release for 1h, 5nM PTX, 1V applied for 1h, 5nM PTX followed by 1V applied for 1h, 1V applied for 1h followed by 5nM PTX and 2 wells were used as control. Live and dead staining was performed 48 hours after the conditioning.

4.3 Polybutylene Succinate Processing and Evaluation as a Micro Fibrous Graft for Tissue Engineering Applications

Materials

Poly (1,4-butylene succinate) extended with 1,6-diisocyanatohexane (T_m 120 °C) (PolyBS), 1,1,1,3,3,3-hexafluoroisopropanol (HFIP) and Dulbecco's phosphate buffered saline (DPBS) were purchased from Aldrich Milan, Italy.

Dulbecco's modified Eagle's medium (DMEM), fetal bovine serum (FBS), trypsin, l-glutamine, penicillin, streptomycin, and amphotericin were purchased from Euroclone group (Milan, Italy).

Porcine bile was extracted from pigs at Istituto Zooprofilattico della Sicilia "A. Mirri," Palermo, Italy accordingly with European rules on animal experiments.

Human blood was extracted from volunteers upon informed consent and isolated at the University of Palermo, Palermo, Italy.

NHDF-Ad-Human Dermal Fibroblasts, Adult were obtained from Lonza bioscience and used after 9 doublings. The cell line was grown in a minimum essential medium [Dulbecco's modified Eagle's medium (DMEM)] supplemented with 10% (*v*/*v*) fetal bovine serum (FBS), 2 mM l-glutamine, 100 um/mL penicillin, 100 µg/mL streptomycin, and 2.5 µg/mL amphotericin B (all reagents were from Euroclone, Milan, Italy) under standard conditions (95% relative humidity, 5% CO_2, 37 °C).

Fabrication of the fibrous graft through electrospinning

PolyBS was blended at 15% *w*/*v* in 1,1,1,3,3,3-hexafluoroisopropanol (HFIP) under mechanical stirring at room temperature. The polymer solution was collected by a precision 10 mL syringe and placed in an NF 103 Electrospinning (MECC, Fukuoka, Japan). The flow passed through a PTFE tube and then in a steel flat needle (22 gauge) with 15.5 cm gap between the needle tip and the collector. One high-voltage generator was employed with a positive voltage (+12.5 kV) to charge the steel capillary containing the polymer solution while the stainless-steel collector rod was maintained at ground voltage. Rotational speed and translational movement were kept constants for all the fabrications (40 rpm, 0.8 cm/s, span 5 cm). The humidity was maintained in a range between 23% and 27%. Deposited scaffolds were soaked in water for 10 min, then the electrospun grafts were quickly slipped through the metal rod and dried.

Morphological characterization of the electrospun graft

In this study, scanning electron microscopy (SEM) was adopted as an investigation method to study the morphology of ES scaffolds. The samples were dehydrated and mounted on aluminium stubs with double adhesive carbon tape. Stubs were vacuum-coated with a 5-nm thick layer of gold (Sputter Coater LuxorAu, Luxor Tech, Nazareth BELGIUM) and observed by a Phenom PRO X SEM.

The fiber diameter, morphology and pore size were evaluated using the ImageJ (1.52Q Wayne Rasband National Institute of Health, Bethesda, MD, USA) software by measuring the diameters of at least 50 fibers and hundreds of pores from each SEM micrograph.

A micro-Computed Tomography (μCT) scanner (Skyscan 1272, Bruker Kontich, Belgium) has been used to run the μCT analysis. One side of the sample was held fixed on the instrument rotating support by laying a layer of wax. The images were acquired by setting a rotation step of 0.2° with a pixel size of 3 um. An X-ray beam with a source voltage of 40 kV and a source current of 250 uA was used. To image the whole sample in high resolution mode the functions ’oversize’ and ’batch Scanning’ were used. These functions allow to scan the whole object by dividing it into sub-objects and then reconstructing the sample. In this case, the uCT of the full cylinder has been achieved by combining 5 scans of sub-cylinders.

Water permeability and wettability evaluations of the graft

The water vapour transmission rate (WVTR) was evaluated, with distilled water, at 25 °C and 38 °C by using a PermeH2O ExtraSolution instrument at 37 °C and with a relative humidity of 50%. The analysis was performed in triplicate and results were expressed as mean permeability ($g/m^2 \cdot 24\ h$) ± standard deviation.

The porosity was calculated as a difference between the predicted scaffold density and the polymer density (gravimetry) by the equation as follows:

$$P = \left(1 - \frac{M}{v \times \rho \times 1000}\right) \times 100$$

where P (%) is porosity, M is the weight of the graft [g], v is the volume of the graft [m^3], ρ is the density of PolyBS [g/cm^3].

The hydrophilicity of the grafts was studied by a video contact angle instrument (FTA 1000 C class, First Ten Angstroms, Portsmouth, VA, USA). Deionized water was deposited on the graft surface and an image of the drop was recorded. From the images of the droplets on the surface of the mats, at scheduled time intervals of up to 30 min, acquired by a digital camera and processed by a software program, the average values of the water contact angles were determined. The contact angle experiments were performed in triplicate at room temperature, and the results were expressed as mean value ± standard deviation.

Degradation evaluation

The degradation test was carried out at 37 °C in three different buffer solutions sodium azide/PBS 0.02 M pH 7.4, porcine bile and human plasma. The electrospun grafts were cut, washed in distilled water, lyophilized, and weighed (w_0). The weight loss was measured at scheduled time intervals, up to one month, after washing them four times in ultra-pure water and lyophilising them. These experiments were performed in triplicate, and results were expressed as the mean value of recovered weight ± standard deviation. Results were plotted against t_0. Finally, the samples were coated with gold and observed with SEM.

Uniaxial and suture retention tests

Mechanical testing was performed, by tensile measurements, on the fibrous scaffolds using a Bose TA Instruments ElectroForce Test Bench System. Dry scaffolds were cut into strips, width = 5 mm and length =30 mm, along their circumferential or longitudinal directions. The thickness measurement of each specimen, obtained with a digital calibre, was 400 um. The initial length between the clamps was 15 mm and firm retention of the scaffold was ensured by the rugged metal clamps of the tensile system. The dry specimens from each direction were tested at room temperature by pulling at 10 mm/min crosshead speed until rupture following 10 cycles of preconditioning to 15% strain. Load-displacement curves were computed to obtain

stress-strain relationships according to current length and cross-sectional area with the assumption of incompressibility.

Ultimate tensile stress (UTS) and strain to failure (STF) were considered, respectively as the maximum stress value before failure and its corresponding value of strain. Elastic modulus was estimated by calculating the slope of the stress-strain curves in the elastic region. Suture retention tests were performed on rectangular specimens clamped at the edge located opposite the suture. The thread was passed through the material using the provided triangular needle (2–0) and closed into a loop by multiple knots. The specimen had a free length of 20 mm, a width of 11 mm and 0.2 mm thickness. The suture bite was centred to the specimen width and its distance from the clamp was 18 mm. The suture loop was first pulled at 0.2 N while the specimen was held fixed. Once the suture wire was taut, a pulling rate of 1 mm/s was applied until final specimen failure, characterized by suture pullout.

In vitro cytocompatibility and haemolytic studies

The electrospun grafts were cut into a square shape of 1.5 mm × 1.5 mm and sterilized with gas plasma for in vitro cell culture studies. Then, were mounted on sterile CellCrown inserts (Scaffdex) and transferred into a 48-well tissue culture polystyrene plate. Cultured NHDF were suspended in complete DMEM, about 30,000 cells per well, and used for culture seeding. Cell morphology and proliferation were studied through SEM and immunocytochemistry to visualize cytoskeleton organization and count cell nuclei. At each time point, the samples were washed with

DPBS and fixated in 4% formaldehyde in PBS for 15 min at room temperature. Nuclei were counterstained with 4–6-diamidino-2-phenylindole (DAPI) for 10 min after 24 and 72 h in culture. Then, the samples were washed three times with PBS for 5 min, mounted onto glass slides and viewed under a Zeiss Axio vert. A1.

For the proliferation and attachment assessment, the number of DAPI-stained nuclei on the surface of the scaffold was counted using the image editing software ImageJ.

After the fluorescence analysis, the samples were washed four times in ultra-pure water and dehydrated using gradual ethanol concentrations (30%, 60%, 90% *v*/*v* and pure ethanol) for 10 min each. Finally, the samples were treated with hexamethyldisilazane (HMDS) and dried under a flow hood. The samples were coated with gold and observed with SEM.

Three millilitres of blood from a healthy donor were collected in Vacuette® containing sodium edetate. The anticoagulated blood was kept for 60 min at 37 °C, after which the tubes were centrifuged at 500× *g* for 5 min. The supernatant was removed, and the pellet was washed 5 times with 2.5 mL of PBS. It was subsequently diluted 1:50 in PBS providing the source of haemoglobin for haemolysis assay. The rate of haemolysis was evaluated by determining the relative amounts of haemoglobin released into the solution phase from erythrocytes in diluted whole blood exposed to the test materials. Electrospun samples were cut into 1 cm^2 squares and covered with the prepared solution. The negative controls contained only the erythrocytes solution in PBS and positive controls contained 2% Triton 100× in distilled water to induce maximal lysis of erythrocytes. The tested samples were kept for 60 min at 37 °C, after which the solutions were centrifuged at 500× *g* for 5 min. The supernatant containing the solubilized haemoglobin was removed and its absorbance was measured at a wavelength of 570 nm (three measurements from each sample). After

the analysis, the samples were fixated in 4% formaldehyde in PBS for 15 min at room temperature. Then washed four times in ultra-pure water and dehydrated using gradual ethanol concentrations (30%, 60%, 90% *v*/*v* and pure ethanol) for 10 min each. Finally, the samples were coated with gold and observed with SEM.

In vivo studies

Study population

Procedures involving animals were carried out following the Italian Legislative Decree N° 26/2014 and the European Directive 2010/63/EU. The animals were housed and tested at the Istituto Zooprofilattico Sperimentale della Sicilia 'A. Mirri' with ministerial authorisation: 14/2015-UT. The number of animals used for this project is reduced to the minimum compatible with the verification of the scientific objectives, compatible with the standards published in the literature that allow statistical evaluation. The present in vivo study was conducted on 9 male New Zealand white rabbits from the company Harlan Laboratories srl Zona Industriale Azzida, 57 33049 - San Pietro al Natisone, with an average body weight of 4.85 kg (range: 3.5-6 kg). A sample size of 9 rabbits was required to obtain a 98% power and an average SFI of at least 15 points better than the control group. A one-sided two-sample t-test was calculated with a significance level (alpha) of 0.05. Animals were housed in polypropylene cages and kept at controlled temperature (22 ± 2°C), humidity (50–55%) and light (12 hr

light/dark cycle). Animals had access to food and water ad libitum. Rabbits were randomly divided into 3 groups of three individuals each and allowed to acclimate for at least 2 days before experiments.

Surgical procedure

The experimental procedure was conducted under general anaesthesia and with the administration of analgesics and antibiotic therapy so as not to induce any pain, suffering or stress to the animal. Animals were induced to anaesthetic depth with inhaled isoflurane at 2% and then anaesthetised with intramuscular injection (i.m.) of Zoletil(r) (tiletamine/zolazepam; 10 mg/kg) and Domitor(r) (medetomidine hydrochloride; 0.5 mg/kg.

The surgical procedure was performed by the same surgeon, in a sterile field after shaving and disinfecting the skin with iodine solution. After shaving, a full-thickness incision was made along the midline of the skull exposing both frontal and parietal bones. An approximately 8mm full-thickness circular defect was created on one frontal bone using a high-precision surgical drill under constant saline irrigation. An equal defect was created on the contralateral frontal bone. All procedures were performed under constant saline irrigation to avoid injury to the dura mater and underlying brain tissue. Then, the 8 mm x 2.5 mm scaffold was placed in one of the randomly chosen bone defects without exerting any pressure on the underlying tissue.

At the end of the procedure, each subject had two bone defects. One defect was treated by applying the scaffold while the other was left to heal spontaneously. No suturing of the periosteum was performed. The skin was sutured with 3-0 silk and disinfected with iodine solution (Betadine). I.m. atipamezole (Antisedan) (300 µg/kg) was used to awaken all rabbits. Carprofen (5 mg/kg) and Enrofloxacin (5 mg/kg) were daily administered for 1 week to each rabbit. After the procedure, each animal was assigned an identification number and housed one per cage. They were monitored daily for infection, self-mutilation, and signs of distress.

Imaging by CT scanning

CT images were acquired with a Simens SOMATOM Definition AS machine, 128 banks, rotation time 0.5 seconds, maximum mAs 250, effective 100-120 mAs, Kilovolt (KV)120, thickness 1.2 mm with 0.6 mm interval, pitch 0.6. The filter used was B20fsmooth and window W450C40.

The bone reconstruction was done with 0.6 mm thickness with 0.3 mm interval, B60fsharp filter, "osteo" window W1500C450.

As in the 2018 study by Pihlman H. et al, the area of the defect covered by mineralised bone tissue was assessed by CT evaluation [112].

Histological examination

Upon completion of the CT examination, the subjects were promptly and humanely euthanized through intra-cardiac administration of Tranax (1 ml). Following the process of shaving, a median incision was executed to expose the frontal bones. Subsequently, the frontal bones were harvested with the aid of a high-precision surgical burr.

The specimens, fixed and preserved in 10% buffered formalin, were decalcified using Na EDTA (10% w/v, pH 7.2), before histological analysis. The decalcified frontal bone samples were cut transversely in two from the centre of the defect. All samples were embedded in paraffin and sectioned at a thickness of 5.0 μm for staining with haematoxylin and eosin (H&E).

The samples were subjected to a drying process overnight in an oven maintained at 37°C. Following this, the samples were treated with xylene to remove any remaining impurities for 20 minutes. After a series of passages in decreasing alcohol (100°, 95°, 75° and 50°), the slides were washed in distilled water and then stained with H&E. This was followed by dehydration in ascending alcohols (50°, 75°, 95° and 100°) and clarification in xylene. After this step, the slides were mounted in an acrylic mounting medium (Eukitt®, O. Kindler GmbH).

The stained samples were analysed for tissue infiltration, bone formation patterns and scaffold integration. Images of the stained slides were obtained with a Leica DMR microscope equipped with a Leica DFC 320 digital camera and analysed using digital image analysis (Nikon NIS Br, Nikon Instruments Europe BV, Amsterdam, The Netherlands).

Immunohistochemical evaluation of the samples was also performed for CD56 (to assess the presence of osteoblasts), CD68 (to assess the presence of osteoclasts) and CD34 (to assess the presence of per-vessels).

Statistical analysis

The collected data were analysed within each group using GraphPad PrismTM 4.0 software (GraphPad Software Inc., San Diego, CA, USA). The two-way ANOVA associated with the 'Sidak' push-out test was used. All data were presented as mean and the statistical significance was set at $p<0.05$.

5. Conclusions

In this comprehensive exploration of biomaterials, the present study has delved into the complexities and nuances surrounding tailored polymers for advanced biomedical devices. Specifically, a biodegradable segmented polyurethane was synthesized, characterized, and processed to serve as a biomaterial. The synthesis involved employing BDI as a reactive agent for generating hard segments, following the chemistry of isocyanates, with the addition of LDA as a dopamine-containing chain extender. This polyurethane urea exhibits a remarkable hydrolytic resistance against degradation, coupled with a low melting point of 55°C and impressive adhesive properties. The advantageous combination of a relatively low melting temperature and the rheological characteristics of the molten polymer positions PU-LDA favourably for the melt-extrusion 3D printing process. This facilitates the production of precise microfibers and enables the construction of structures with a customizable microarchitecture and external shape. The unique properties of PU-LDA pave the way for intricate and controlled 3D printing applications, showcasing its versatility in generating finely tuned structures for various purposes. The demonstrated high adhesion and excellent processability of this biomaterial unveil compelling possibilities for diverse applications. Specifically, it could find utility in micropattern coatings on implantable devices or drug delivery systems, offering the capability to incorporate even thermolabile drugs or biomolecules. Furthermore, these remarkable properties make this polyurethane urea well-suited for serving as a coating interface between metallic prostheses or implantable devices and biological tissues to enhance biological tolerance and promote biointegration. Consequently, poly(3,4-

ethylenedioxythiophene) (PEDOT) doped with polystyrene sulfonate was integrated into the bioadhesive polyurethane urea matrix to create a conductive bioadhesive coating. The resulting polymer underwent comprehensive characterization through electrochemical impedance spectroscopy, conducted in both wet and dry conditions, and cyclic voltammetry. It emerged as an enticing candidate for a multifunctional coating capable of actively regulating therapeutic release within the tumour microenvironment. Therefore, to harness this potential, paclitaxel was incorporated in the PEDOT-doped polyurethane urea matrix and porous titanium rods were dip-coated into the loaded polymeric solution. These final devices were designed around the neurosurgical toolkit to perform a biopsy and will be supported by a cartridge during the insertion. The assessment of drug release was conducted in physiological-like conditions demonstrating a substantial increase when voltage is applied. This dynamic interplay between the enhanced and passive release profiles highlights the effectiveness of applying voltage in promoting controlled and increased drug release, presenting valuable insights for optimizing drug delivery systems. Lastly, the in vitro effects were evaluated using a neuroblastoma cell line (SH-SY5Y). The findings demonstrated the cytotoxic effectiveness of the CB devices and supported our hypothesis that applied voltage alters the permeability of the cell membrane, facilitating enhanced drug uptake.

Simultaneously, a tubular scaffold composed of electrospun polybutylene succinate (PolyBS) for tissue engineering applications was described. Enhancing biointegration and functionality in electrospun scaffolds presents several challenges. The primary hurdles include the production of cytocompatible small-diameter grafts that are impermeable to cells yet permeable to metabolites, all while retaining their geometries during short-term mechanical conditioning and remaining suturable and

non-hemolytic. Additionally, considerations such as sterilizability and scalability for clinical applications add further practical challenges that must always be kept at the forefront of development efforts. The key benefits of this aliphatic polyester include a regular and controllable structure, robust mechanical properties, and a gradual degradation rate. Moreover, PolyBS holds the advantage of being amenable to mass production, facilitating efficient shipping and storage in a reproducible and controlled manner, all at an economically viable cost. These attributes collectively position electrospun PolyBS as a promising material for tissue engineering, offering a harmonious balance of structural integrity, degradation kinetics, and cost-effectiveness. The chosen processing technique holds the advantage of allowing precise tuning of the ranges of lengths, diameters, and even anisotropy. Consequently, it becomes feasible to tailor various properties, effectively meeting the diverse requirements for its applications as a scaffold. This flexibility in customization offers a strategic approach to optimizing the material for specific uses, ensuring that the electrospun PolyBS scaffold can be finely tuned to address a variety of applications within the field of tissue engineering. Additionally, the fibres generated through electrospinning contribute to the formation of a structure characterized by interconnected and adjustable pores. This, coupled with the material's inherent permeability, facilitates the physiological exchange of metabolites and catabolites. A morphological and mechanical characterization showed that these grafts retain their geometry and properties upon short-term mechanical conditioning. The shown degradation profile of the graft enables it to provide initial mechanical support and functionality while being colonized and then replaced by host cells. The scaffold's intentionally designed structure emulates the composition of the ECM, fostering optimal conditions for cell growth. In vitro results have unequivocally shown a

noteworthy increase in cell density after three days, underscoring the cytocompatibility of the produced PolyBS grafts. Moreover, the absence of cells within the graft's wall or on the outer surface confirmed that the scaffold's morphology serves as a barrier to cell infiltration without impeding cell adhesion. Additionally, this material is considered suitable for implantation, given its ease of handling and suturing, non-haemolytic nature, and remarkable resistance to kinking. These attributes collectively highlight the electrospun PolyBS graft's potential as a reliable and effective biomaterial for implantation, offering a balance between controlled cellular interactions and the necessary mechanical properties for successful integration.

The experimental study conducted in vivo has demonstrated that the administration of a microfibrillar scaffold made of PolyBS constitutes a highly effective approach for inducing accelerated bone regeneration in cases of critical bone defects. Evaluation through CT scans and histologic assessments revealed a substantial enhancement in both qualitative and quantitative aspects of bone regeneration compared to spontaneous healing. The absence of any adverse events served as compelling evidence for the exceptional biocompatibility and biodegradability properties of the scaffold. This combination of features might represent a step toward future research on PolyBS as a biomaterial to produce scaffolds that provide structure and function over time and support host cell remodelling.

6. References

(1) Oveissi, F.; Naficy, S.; Lee, A.; Winlaw, D. S.; Dehghani, F. Materials and Manufacturing Perspectives in Engineering Heart Valves: A Review. **2019**. https://doi.org/10.1016/j.mtbio.2019.100038.

(2) Singh, C.; Wong, C.; Wang, X. Medical Textiles as Vascular Implants and Their Success to Mimic Natural Arteries. *J. Funct. Biomater.* **2015**, *6* (3), 500–525. https://doi.org/10.3390/jfb6030500.

(3) Park, H.; Otte, A.; Park, K. Evolution of Drug Delivery Systems: From 1950 to 2020 and Beyond. *J. Control. Release* **2022**, *342*, 53–65. https://doi.org/10.1016/J.JCONREL.2021.12.030.

(4) Teo, A. J. T.; Mishra, A.; Park, I.; Kim, Y. J.; Park, W. T.; Yoon, Y. J. Polymeric Biomaterials for Medical Implants and Devices. *ACS Biomater. Sci. Eng.* **2016**, *2* (4), 454–472. https://doi.org/10.1021/ACSBIOMATERIALS.5B00429/ASSET/IMAGES/LARGE/AB-2015-00429V_0019.JPEG.

(5) Punj, S.; Singh, J.; Singh, K. Ceramic Biomaterials: Properties, State of the Art and Future Prospectives. *Ceram. Int.* **2021**, *47* (20), 28059–28074. https://doi.org/10.1016/J.CERAMINT.2021.06.238.

(6) Wilson, J. Metallic Biomaterials: State of the Art and New Challenges. *Fundam. Biomater. Met.* **2018**, 1–33. https://doi.org/10.1016/B978-0-08-102205-4.00001-5.

(7) Barrows, T. Degradable Implant Materials: A Review of Synthetic Absorbable Polymers and Their Applications. *Clin. Mater.* **1986**, *1* (4), 233–257.

https://doi.org/10.1016/S0267-6605(86)80015-4.

(8) Lee, Y. J.; Son, H. S.; Jung, G. B.; Kim, J. H.; Choi, S.; Lee, G. J.; Park, H. K. Enhanced Biocompatibility and Wound Healing Properties of Biodegradable Polymer-Modified Allyl 2-Cyanoacrylate Tissue Adhesive. *Mater. Sci. Eng. C* **2015**, *51*, 43–50. https://doi.org/10.1016/J.MSEC.2015.02.042.

(9) Ju, Y. M.; Choi, J. S.; Atala, A.; Yoo, J. J.; Lee, S. J. Bilayered Scaffold for Engineering Cellularized Blood Vessels. *Biomaterials* **2010**, *31* (15), 4313–4321. https://doi.org/10.1016/j.biomaterials.2010.02.002.

(10) McClure, M. J.; Sell, S. A.; Simpson, D. G.; Walpoth, B. H.; Bowlin, G. L. A Three-Layered Electrospun Matrix to Mimic Native Arterial Architecture Using Polycaprolactone, Elastin, and Collagen: A Preliminary Study. *Acta Biomater.* **2010**, *6* (7), 2422–2433. https://doi.org/10.1016/j.actbio.2009.12.029.

(11) Gupta, D.; Jassal, M.; Agrawal, A. K. The Electrospinning Behavior of Poly(Vinyl Alcohol) in DMSO-Water Binary Solvent Mixtures. *RSC Adv.* **2016**, *6* (105), 102947–102955. https://doi.org/10.1039/c6ra15017a.

(12) Sun Han Chang, R. A.; Shanley, J. F.; Kersh, M. E.; Harley, B. A. C. Tough and Tunable Scaffold-Hydrogel Composite Biomaterial for Soft-to-Hard Musculoskeletal Tissue Interfaces. *Sci. Adv.* **2020**, *6* (34), 1–11. https://doi.org/10.1126/sciadv.abb6763.

(13) Llorens, E.; Ibañez, H.; Del Valle, L. J.; Puiggalí, J. Biocompatibility and Drug Release Behavior of Scaffolds Prepared by Coaxial Electrospinning of Poly(Butylene Succinate) and Polyethylene Glycol. *Mater. Sci. Eng. C* **2015**, *49*, 472–484. https://doi.org/10.1016/j.msec.2015.01.039.

(14) Pandey, N.; Soto-Garcia, L. F.; Liao, J.; Zimmern, P.; Nguyen, K. T.; Hong, Y. Mussel-Inspired Bioadhesives in Healthcare: Design Parameters, Current

Trends, and Future Perspectives. *Biomater. Sci.* **2020**, *8* (5), 1240–1255. https://doi.org/10.1039/c9bm01848d.

(15) Zhu, W.; Chuah, Y. J.; Wang, D. A. Bioadhesives for Internal Medical Applications: A Review. *Acta Biomater.* **2018**, *74*, 1–16. https://doi.org/10.1016/J.ACTBIO.2018.04.034.

(16) Ryssel, H.; Gazyakan, E.; Germann, G.; Öhlbauer, M. The Use of MatriDerm® in Early Excision and Simultaneous Autologous Skin Grafting in Burns—A Pilot Study. *Burns* **2008**, *34* (1), 93–97. https://doi.org/10.1016/J.BURNS.2007.01.018.

(17) Singer, A. J.; Quinn, J. V.; Hollander, J. E. The Cyanoacrylate Topical Skin Adhesives. *Am. J. Emerg. Med.* **2008**, *26* (4), 490–496. https://doi.org/10.1016/J.AJEM.2007.05.015.

(18) Kirsch, M.; Ginat, M.; Lecerf, L.; Houël, R.; Loisance, D. Aortic Wall Alterations after Use of Gelatin-Resorcinol-Formalin Glue. *Ann. Thorac. Surg.* **2002**, *73* (2), 642–644. https://doi.org/10.1016/S0003-4975(01)03008-9.

(19) Hata, H.; Takano, H.; Matsumiya, G.; Fukushima, N.; Kawaguchi, N.; Sawa, Y. Late Complications of Gelatin-Resorcin-Formalin Glue in the Repair of Acute Type A Aortic Dissection. *Ann. Thorac. Surg.* **2007**, *83* (5), 1621–1626. https://doi.org/10.1016/J.ATHORACSUR.2007.01.025.

(20) Hyon, S.-H.; Nakajima, N.; Sugai, H.; Matsumura, K. Low Cytotoxic Tissue Adhesive Based on Oxidized Dextran and Epsilon-Poly-L-Lysine. *J Biomed Mater Res Part A* **2013**, *102*, 2511–2520. https://doi.org/10.1002/jbm.a.34923.

(21) Zhang, W.; Wang, R.; Sun, Z. M.; Zhu, X.; Zhao, Q.; Zhang, T.; Cholewinski, A.; Yang, F.; Zhao, B.; Pinnaratip, R.; Forooshani, P. K.; Lee, B. P. Catechol-Functionalized Hydrogels: Biomimetic Design, Adhesion Mechanism, and

Biomedical Applications. *Chem. Soc. Rev.* **2020**, *49* (2), 433–464. https://doi.org/10.1039/c9cs00285e.

(22) Ribena, D. *Dopamine Modification of Interfaces between Polymers and Metals*; 2012. https://doi.org/10.6100/IR735527.

(23) Sun, P.; Lu, H.; Yao, X.; Tu, X.; Zheng, Z.; Wang, X. Facile and Universal Immobilization of L-Lysine Inspired by Mussels. *J. Mater. Chem.* **2012**, *22* (19), 10035–10041. https://doi.org/10.1039/c2jm16598h.

(24) Hong, S.; Yang, K.; Kang, B.; Lee, C.; Song, I. T.; Byun, E.; Park, K. I.; Cho, S. W.; Lee, H. Hyaluronic Acid Catechol: A Biopolymer Exhibiting a PH-Dependent Adhesive or Cohesive Property for Human Neural Stem Cell Engineering. *Adv. Funct. Mater.* **2013**, *23* (14), 1774–1780. https://doi.org/10.1002/adfm.201202365.

(25) Jo, Y. K.; Choi, B. H.; Zhou, C.; Ahn, J. S.; Jun, S. H.; Cha, H. J. Bioengineered Mussel Glue Incorporated with a Cell Recognition Motif as an Osteostimulating Bone Adhesive for Titanium Implants. *J. Mater. Chem. B* **2015**, *3* (41), 8102–8114. https://doi.org/10.1039/c5tb01230a.

(26) Hauser, D.; Septiadi, D.; Turner, J.; Petri-Fink, A.; Rothen-Rutishauser, B. From Bioinspired Glue to Medicine: Polydopamine as a Biomedical Material. *Materials (Basel).* **2020**, *13* (7), 1–22. https://doi.org/10.3390/ma13071730.

(27) Suneetha, M.; Madhusudana Rao, K.; Soo Han, S. Mussel-Inspired Cell/Tissue-Adhesive, Hemostatic Hydrogels for Tissue Engineering Applications. **2019**. https://doi.org/10.1021/acsomega.9b01302.

(28) Sun, P.; Wang, J.; Yao, X.; Peng, Y.; Tu, X.; Du, P.; Zheng, Z.; Wang, X. Facile Preparation of Mussel-Inspired Polyurethane Hydrogel and Its Rapid Curing Behavior. *ACS Appl. Mater. Interfaces* **2014**, *6* (15), 12495–12504.

https://doi.org/10.1021/am502106e.

(29) Mehdizadeh, M.; Weng, H.; Gyawali, D.; Tang, L.; Yang, J. Injectable Citrate-Based Mussel-Inspired Tissue Bioadhesives with High Wet Strength for Sutureless Wound Closure. *Biomaterials* **2012**, *33* (32), 7972–7983. https://doi.org/10.1016/J.BIOMATERIALS.2012.07.055.

(30) Xu, J.; Tam, M.; Samaei, S.; Lerouge, S.; Barralet, J.; Stevenson, M. M.; Cerruti, M. Mucoadhesive Chitosan Hydrogels as Rectal Drug Delivery Vessels to Treat Ulcerative Colitis. *Acta Biomater.* **2017**, *48*, 247–257. https://doi.org/10.1016/J.ACTBIO.2016.10.026.

(31) Yoon Park, J.; Yeom, J.; Seon Kim, J.; Lee, M.; Lee, H.; Sung Nam, Y.; Park, J. Y.; Kim, J. S.; Nam, Y. S.; Yeom, J.; Lee, M.; Lee, H. Cell-Repellant Dextran Coatings of Porous Titania Using Mussel Adhesion Chemistry A. https://doi.org/10.1002/mabi.201300224.

(32) Fernandes, H. R.; Gaddam, A.; Rebelo, A.; Brazete, D.; Stan, G. E.; Ferreira, J. M. F. Bioactive Glasses and Glass-Ceramics for Healthcare Applications in Bone Regeneration and Tissue Engineering. *Materials (Basel).* **2018**, *11* (12), 1–54. https://doi.org/10.3390/ma11122530.

(33) Vallejo-Giraldo, C.; Genta, M.; Cauvi, O.; Goding, J.; Green, R. Hydrogels for 3D Neural Tissue Models: Understanding Cell-Material Interactions at a Molecular Level. *Front. Bioeng. Biotechnol.* **2020**, *8* (November), 1–14. https://doi.org/10.3389/fbioe.2020.601704.

(34) Cuttaz, E. A.; Chapman, C. A. R.; Syed, O.; Goding, J. A.; Green, R. A. Stretchable, Fully Polymeric Electrode Arrays for Peripheral Nerve Stimulation. *Adv. Sci.* **2021**, *8* (8), 1–14. https://doi.org/10.1002/advs.202004033.

(35) Peressotti, S.; Koehl, G. E.; Goding, J. A.; Green, R. A. Self-Assembling

Hydrogel Structures for Neural Tissue Repair. *ACS Biomater. Sci. Eng.* **2021**, *7* (9), 4136–4163. https://doi.org/10.1021/acsbiomaterials.1c00030.

(36) Khan, A.; Alamry, K. A. Stimuli-Responsive Conducting Polymer Composites. *Actuators Fundam. Princ. Mater. Emerg. Technol.* **2020**, 159–186. https://doi.org/10.1002/9781119662693.CH7.

(37) Balberg, I. The Physical Fundamentals of the Electrical Conductivity in Nanotube-Based Composites. *J. Appl. Phys.* **2020**, *128* (20). https://doi.org/10.1063/5.0031257/1025331.

(38) Dalrymple, A. N.; Robles, U. A.; Huynh, M.; Nayagam, B. A.; Green, R. A.; Poole-Warren, L. A.; Fallon, J. B.; Shepherd, R. K. Electrochemical and Biological Performance of Chronically Stimulated Conductive Hydrogel Electrodes. *J. Neural Eng.* **2020**, *17* (2). https://doi.org/10.1088/1741-2552/ab7cfc.

(39) Xu, Y.; Patsis, P. A.; Hauser, S.; Voigt, D.; Rothe, R.; Günther, M.; Cui, M.; Yang, X.; Wieduwild, R.; Eckert, K.; Neinhuis, C.; Akbar, T. F.; Minev, I. R.; Pietzsch, J.; Zhang, Y. Cytocompatible, Injectable, and Electroconductive Soft Adhesives with Hybrid Covalent/Noncovalent Dynamic Network. *Adv. Sci.* **2019**, *6* (15). https://doi.org/10.1002/advs.201802077.

(40) Chapman, C. A. R.; Cuttaz, E. A.; Goding, J. A.; Green, R. A. Actively Controlled Local Drug Delivery Using Conductive Polymer-Based Devices. *Appl. Phys. Lett.* **2020**, *116* (1). https://doi.org/10.1063/1.5138587.

(41) Portillo-Lara, R.; Goding, J. A.; Green, R. A. Adaptive Biomimicry: Design of Neural Interfaces with Enhanced Biointegration. *Curr. Opin. Biotechnol.* **2021**, *72*, 62–68. https://doi.org/10.1016/j.copbio.2021.10.004.

(42) Chapman, C. A. R.; Fernandez-Patel, S.; Jahan, N.; Cuttaz, E. A.; Novikov, A.;

Goding, J. A.; Green, R. A. Controlled Electroactive Release from Solid-State Conductive Elastomer Electrodes. *Mater. Today Bio* **2023**, *23* (November), 100883. https://doi.org/10.1016/j.mtbio.2023.100883.

(43) *Worldwide cancer incidence statistics | Cancer Research UK*. https://www.cancerresearchuk.org/health-professional/cancer-statistics/worldwide-cancer/incidence (accessed 2024-01-11).

(44) Krukiewicz, K.; Zak, J. K. Biomaterial-Based Regional Chemotherapy: Local Anticancer Drug Delivery to Enhance Chemotherapy and Minimize Its Side-Effects. **2016**. https://doi.org/10.1016/j.msec.2016.01.063.

(45) Aigner, K. R.; Stephens, F. O. Induction Chemotherapy: Systemic and Locoregional: Second Edition. *Induction Chemother. Syst. Locoregional Second Ed.* **2016**, 1–506. https://doi.org/10.1007/978-3-319-28773-7/COVER.

(46) Solid Tumor Therapy: Manipulation of the Vasculature with TNF.

(47) De Souza, R.; Zahedi, P.; Allen, C. J.; Piquette-Miller, M. Polymeric Drug Delivery Systems for Localized Cancer Chemotherapy. *Drug Deliv.* **2010**, *17* (6), 365–375. https://doi.org/10.3109/10717541003762854.

(48) Darvin, P.; Chandrasekharan, A.; Santhosh Kumar, T. R. Introduction to Smart Drug Delivery Systems. *Biomim. Nanoeng. Mater. Adv. Drug Deliv.* **2019**, 1–9. https://doi.org/10.1016/B978-0-12-814944-7.00001-1.

(49) Abouelmagd, S. A.; Ellah, N. H. A.; Hamid, B. N. A. El. Temperature and PH Dual-Stimuli Responsive Polymeric Carriers for Drug Delivery. *Stimuli Responsive Polym. Nanocarriers Drug Deliv. Appl. Vol. 2 Adv. Nanocarriers Ther.* **2018**, 87–109. https://doi.org/10.1016/B978-0-08-101995-5.00003-9.

(50) Pérez-Martínez, C. J.; Morales Chávez, S. D.; Del Castillo-Castro, T.; Lara Ceniceros, T. E.; Castillo-Ortega, M. M.; Rodríguez-Félix, D. E.; Gálvez Ruiz,

J. C. Electroconductive Nanocomposite Hydrogel for Pulsatile Drug Release. *React. Funct. Polym.* **2016**, *100*, 12–17. https://doi.org/10.1016/J.REACTFUNCTPOLYM.2015.12.017.

(51) Zhang, A.; Jung, K.; Li, A.; Liu, J.; Boyer, C. Recent Advances in Stimuli-Responsive Polymer Systems for Remotely Controlled Drug Release. *Prog. Polym. Sci.* **2019**, *99*. https://doi.org/10.1016/J.PROGPOLYMSCI.2019.101164.

(52) Alkahtani, M. E.; Elbadawi, M.; Chapman, C. A. R.; Green, R. A.; Gaisford, S.; Orlu, M.; Basit, A. W. Electroactive Polymers for On-Demand Drug Release. *Adv. Healthc. Mater.* **2024**, *13* (3), 2301759. https://doi.org/10.1002/ADHM.202301759.

(53) Puiggalí-Jou, A.; del Valle, L. J.; Alemán, C. Drug Delivery Systems Based on Intrinsically Conducting Polymers. *J. Control. Release* **2019**, *309*, 244–264. https://doi.org/10.1016/J.JCONREL.2019.07.035.

(54) Mirvakili, S. M.; Langer, R. Wireless On-Demand Drug Delivery. *Nat. Electron. 2021 47* **2021**, *4* (7), 464–477. https://doi.org/10.1038/s41928-021-00614-9.

(55) Ahmed, T. Biomaterial-Based in Vitro 3D Modeling of Glioblastoma Multiforme. *Cancer Pathog. Ther.* **2023**, *1* (3), 177–194. https://doi.org/10.1016/j.cpt.2023.01.002.

(56) Ameer, J. M.; Anil Kumar, P. R.; Kasoju, N. Strategies to Tune Electrospun Scaffold Porosity for Effective Cell Response in Tissue Engineering. *J. Funct. Biomater.* **2019**, *10* (3), 1–21. https://doi.org/10.3390/jfb10030030.

(57) Badylak, S. F.; Freytes, D. O.; Gilbert, T. W. Extracellular Matrix as a Biological Scaffold Material: Structure and Function. *Acta Biomater.* **2009**, *5* (1), 1–13. https://doi.org/10.1016/j.actbio.2008.09.013.

(58) Harley, B. A. C.; Kim, H. Do; Zaman, M. H.; Yannas, I. V.; Lauffenburger, D. A.; Gibson, L. J. Microarchitecture of Three-Dimensional Scaffolds Influences Cell Migration Behavior via Junction Interactions. *Biophys. J.* **2008**, *95* (8), 4013–4024. https://doi.org/10.1529/biophysj.107.122598.

(59) Williams, D. F. Specifications for Innovative, Enabling Biomaterials Based on the Principles of Biocompatibility Mechanisms. *Front. Bioeng. Biotechnol.* **2019**, *7* (October), 1–10. https://doi.org/10.3389/fbioe.2019.00255.

(60) Gaharwar, A. K.; Singh, I.; Khademhosseini, A. Engineered Biomaterials for in Situ Tissue Regeneration. *Nat. Rev. Mater.* https://doi.org/10.1038/s41578-020-0209-x.

(61) Jianjun Guana, Kazuro L. Fujimotoa, Michael S. Sacksa,b, and W. R. W. Preparation and Characterization of Highly Porous, Biodegradable Polyurethane Scaffolds for Soft Tissue Applications. **2010**, *26* (18), 3961–3971. https://doi.org/10.1016/j.biomaterials.2004.10.018.Preparation.

(62) Uttayarat, P.; Perets, A.; Li, M.; Pimton, P.; Stachelek, S. J.; Alferiev, I.; Composto, R. J.; Levy, R. J.; Lelkes, P. I. Micropatterning of Three-Dimensional Electrospun Polyurethane Vascular Grafts. *Acta Biomater.* **2010**, *6* (11), 4229–4237. https://doi.org/10.1016/j.actbio.2010.06.008.

(63) Contreras-Cáceres, R.; Cabeza, L.; Perazzoli, G.; Díaz, A.; López-Romero, J. M.; Melguizo, C.; Prados, J. Electrospun Nanofibers: Recent Applications in Drug Delivery and Cancer Therapy. *Nanomater. 2019, Vol. 9, Page 656* **2019**, *9* (4), 656. https://doi.org/10.3390/NANO9040656.

(64) Xue, J.; Wu, T.; Dai, Y.; Xia, Y. Electrospinning and Electrospun Nanofibers: Methods, Materials, and Applications. *Chem. Rev.* **2019**, *119* (8), 5298–5415. https://doi.org/10.1021/acs.chemrev.8b00593.

(65) Rnjak-Kovacina, J.; Weiss, A. S. Increasing the Pore Size of Electrospun Scaffolds. *Tissue Eng. - Part B Rev.* **2011**, *17* (5), 365–372. https://doi.org/10.1089/ten.teb.2011.0235.

(66) Zhang, Y.; Li, X. S.; Guex, A. G.; Liu, S. S.; Müller, E.; Malini, R. I.; Zhao, H. J.; Rottmar, M.; Maniura-Weber, K.; Rossi, R. M.; Spano, F. A Compliant and Biomimetic Three-Layered Vascular Graft for Small Blood Vessels. *Biofabrication* **2017**, *9* (2). https://doi.org/10.1088/1758-5090/aa6bae.

(67) Alsoufi, M. S.; Elsayed, A. E. How Surface Roughness Performance of Printed Parts Manufactured by Desktop FDM 3D Printer with PLA+ Is Influenced by Measuring Direction. *Am. J. Mech. Eng. Vol. 5, 2017, Pages 211-222* **2017**, *5* (5), 211–222. https://doi.org/10.12691/AJME-5-5-4.

(68) Benjamin, E. J.; Muntner, P.; Alonso, A.; Bittencourt, M. S.; Callaway, C. W.; Carson, A. P.; Chamberlain, A. M.; Chang, A. R.; Cheng, S.; Das, S. R.; Delling, F. N.; Djousse, L.; Elkind, M. S. V.; Ferguson, J. F.; Fornage, M.; Jordan, L. C.; Khan, S. S.; Kissela, B. M.; Knutson, K. L.; Kwan, T. W.; Lackland, D. T.; Lewis, T. T.; Lichtman, J. H.; Longenecker, C. T.; Loop, M. S.; Lutsey, P. L.; Martin, S. S.; Matsushita, K.; Moran, A. E.; Mussolino, M. E.; O'Flaherty, M.; Pandey, A.; Perak, A. M.; Rosamond, W. D.; Roth, G. A.; Sampson, U. K. A.; Satou, G. M.; Schroeder, E. B.; Shah, S. H.; Spartano, N. L.; Stokes, A.; Tirschwell, D. L.; Tsao, C. W.; Turakhia, M. P.; VanWagner, L. B.; Wilkins, J. T.; Wong, S. S.; Virani, S. S. *Heart Disease and Stroke Statistics-2019 Update: A Report From the American Heart Association*; 2019; Vol. 139. https://doi.org/10.1161/CIR.0000000000000659.

(69) Timmis, A.; Townsend, N.; Gale, C. P.; Torbica, A.; Lettino, M.; Petersen, S. E.; Mossialos, E. A.; Maggioni, A. P.; Kazakiewicz, D.; May, H. T.; De Smedt, D.;

Flather, M.; Zuhlke, L.; Beltrame, J. F.; Huculeci, R.; Tavazzi, L.; Hindricks, G.; Bax, J.; Casadei, B.; Achenbach, S.; Wright, L.; Vardas, P.; Mimoza, L.; Artan, G.; Aurel, D.; Chettibi, M.; Hammoudi, N.; Sisakian, H.; Pepoyan, S.; Metzler, B.; Siostrzonek, P.; Weidinger, F.; Jahangirov, T.; Aliyev, F.; Rustamova, Y.; Mrochak, N. M. A.; Lancellotti, P.; Pasquet, A.; Claeys, M.; Kusljugic, Z.; Hudic, L. D.; Smajic, E.; Tokmakova, M. P.; Gatzov, P. M.; Milicic, D.; Bergovec, M.; Christou, C.; Moustra, H. H.; Christodoulides, T.; Linhart, A.; Taborsky, M.; Abdelhamid, M.; Shokry, K.; Kampus, P.; Viigimaa, M.; Ryödi, E.; Niemela, M.; Rissanen, T. T.; Le Heuzey, J. Y.; Gilard, M.; Aladashvili, A.; Gamkrelidze, A.; Kereselidze, M.; Zeiher, A.; Katus, H.; Bestehorn, K.; Tsioufis, C.; Goudevenos, J.; Csanádi, Z.; Becker, D.; Tóth, K.; Hrafnkelsdóttir, P. J.; Crowley, J.; Kearney, P.; Dalton, B.; Zahger, D.; Wolak, A.; Gabrielli, D.; Indolfi, C.; Urbinati, S.; Imantayeva, G.; Berkinbayev, S.; Bajraktari, G.; Ahmeti, A.; Berisha, G.; Erkin, M.; Saamay, A.; Erglis, A.; Bajare, I.; Jegere, S.; Mohammed, M.; Sarkis, A.; Saadeh, G.; Zvirblyte, R.; Sakalyte, G.; Slapikas, R.; Ellafi, K.; El Ghamari, F.; Banu, C.; Beissel, J.; Felice, T.; Buttigieg, S. C.; Xuereb, R. G.; Popovici, M.; Boskovic, A.; Rabrenovic, M.; Ztot, S.; Abir-Khalil, S.; Van Rossum, A. C.; Mulder, B. J. M.; Elsendoorn, M. W.; Srbinovska-Kostovska, E.; Kostov, J.; Marjan, B.; Steigen, T.; Mjølstad, O. C.; Ponikowski, P.; Witkowski, A.; Jankowski, P.; Gil, V. M.; Mimoso, J.; Baptista, S.; Vinereanu, D.; Chioncel, O.; Popescu, B. A.; Shlyakhto, E.; Oganov, R.; Foscoli, M.; Zavatta, M.; Dikic, A. D.; Beleslin, B.; Radovanovic, M. R.; Hlivak, P.; Hatala, R.; Kaliska, G.; Kenda, M.; Fras, Z.; Anguita, M.; Cequier, A.; Muniz, J.; James, S.; Johansson, B.; Platonov, P.; Zellweger, M. J.; Pedrazzini, G. B.; Carballo, D.; Shebli, H. E.; Kabbani, S.; Abid, L.; Addad, F.; Bozkurt, E.;

Kayikçioğlu, M.; Erol, M. K.; Kovalenko, V.; Nesukay, E.; Wragg, A.; Ludman, P.; Ray, S.; Kurbanov, R.; Boateng, D.; Daval, G.; De Benito Rubio, V.; Sebastiao, D.; De Courtelary, P. T.; Bardinet, I. European Society of Cardiology: Cardiovascular Disease Statistics 2019. *Eur. Heart J.* **2020**, *41* (1), 12–85. https://doi.org/10.1093/eurheartj/ehz859.

(70) Keshvardoostchokami, M.; Majidi, S. S.; Huo, P.; Ramachandran, R.; Chen, M.; Liu, B. Electrospun Nanofibers of Natural and Synthetic Polymers as Artificial Extracellular Matrix for Tissue Engineering. *Nanomaterials* **2021**, *11* (1), 1–23. https://doi.org/10.3390/nano11010021.

(71) Ravichandran, R.; Venugopal, J. R.; Sundarrajan, S.; Mukherjee, S.; Sridhar, R.; Ramakrishna, S. Minimally Invasive Injectable Short Nanofibers of Poly(Glycerol Sebacate) for Cardiac Tissue Engineering. *Nanotechnology* **2012**, *23* (38). https://doi.org/10.1088/0957-4484/23/38/385102.

(72) Lorenzo Soletti1, 2, 3, 4, Alejandro Nieponice1, 3, 4, Yi Hong1, 3, 4, Sang-Ho Ye1, 3, 4, John J. Stankus3, 5 , William R. Wagner1, 2, 3, 4, 5, and David A. Vorp1, 2, 3, 4. In Vivo Performance of a Phospholipid-Coated Bioerodable Elastomeric Graft for Small-Diameter Vascular Applications. *Bone* **2014**, *23* (1), 1–7. https://doi.org/10.1002/jbm.a.32997.In.

(73) Lorenzo Soletti1, 3, 4, 5, Yi Hong3, 4, 5, Jianjun Guan3, 4, 5, John J. Stankus2, 4, Mohammed S. El- Kurdi1, 3, 4, 5William R. Wagner1, 2, 3, 4, 5, and David A. Vorp1, 3, 4, 5. A Bi-Layered Elastomeric Scaffold for Tissue Engineering of Small-Diameter Vascular Grafts. *Bone* **2013**, *23* (1), 237–337. https://doi.org/10.1016/j.actbio.2009.06.026.A.

(74) Rafiqah, S. A.; Khalina, A.; Harmaen, A. S.; Tawakkal, I. A.; Zaman, K.; Asim, M.; Nurrazi, M. N.; Lee, C. H. A Review on Properties and Application of

Bio-based Poly(Butylene Succinate). *Polymers (Basel).* **2021**, *13* (9), 1–28. https://doi.org/10.3390/polym13091436.

(75) Fabbri, M.; Gigli, M.; Gamberini, R.; Lotti, N.; Gazzano, M.; Rimini, B.; Munari, A. Hydrolysable PBS-Based Poly(Ester Urethane)s Thermoplastic Elastomers. *Polym. Degrad. Stab.* **2014**, *108*, 223–231. https://doi.org/10.1016/j.polymdegradstab.2014.03.033.

(76) Stoyanova, N.; Paneva, D.; Mincheva, R.; Toncheva, A.; Manolova, N.; Dubois, P.; Rashkov, I. Poly(l-Lactide) and Poly(Butylene Succinate) Immiscible Blends: From Electrospinning to Biologically Active Materials. *Mater. Sci. Eng. C* **2014**, *41*, 119–126. https://doi.org/10.1016/j.msec.2014.04.043.

(77) Ju, J.; Gu, Z.; Liu, X.; Zhang, S.; Peng, X.; Kuang, T. Fabrication of Bimodal Open-Porous Poly (Butylene Succinate)/Cellulose Nanocrystals Composite Scaffolds for Tissue Engineering Application. *Int. J. Biol. Macromol.* **2020**, *147*, 1164–1173. https://doi.org/10.1016/J.IJBIOMAC.2019.10.085.

(78) Tian, L.; Wang, P.; Zhao, Z.; Ji, J. Antimicrobial Activity of Electrospun Poly(Butylenes Succinate) Fiber Mats Containing PVP-Capped Silver Nanoparticles. *Appl. Biochem. Biotechnol.* **2013**, *171* (7), 1890–1899. https://doi.org/10.1007/s12010-013-0461-2.

(79) Ribeiro, V. P.; Almeida, L. R.; Martins, A. R.; Pashkuleva, I.; Marques, A. P.; Ribeiro, A. S.; Silva, C. J.; Bonifácio, G.; Sousa, R. A.; Oliveira, A. L.; Reis, R. L. Modulating Cell Adhesion to Polybutylene Succinate Biotextile Constructs for Tissue Engineering Applications. *J. Tissue Eng. Regen. Med.* **2017**, *11* (10), 2853–2863. https://doi.org/10.1002/term.2189.

(80) Cicero, L.; Licciardi, M.; Cirincione, R.; Puleio, R.; Giammona, G.; Giglia, G.; Sardo, P.; Edoardo Vigni, G.; Cioffi, A.; Sanfilippo, A.; Cassata, G.

Polybutylene Succinate Artificial Scaffold for Peripheral Nerve Regeneration. *J. Biomed. Mater. Res. - Part B Appl. Biomater.* **2022**, *110* (1), 125–134. https://doi.org/10.1002/jbm.b.34896.

(81) Almeida, L. R.; Martins, A. R.; Fernandes, E. M.; Oliveira, M. B.; Correlo, V. M.; Pashkuleva, I.; Marques, A. P.; Ribeiro, A. S.; Durães, N. F.; Silva, C. J.; Bonifácio, G.; Sousa, R. A.; Oliveira, A. L.; Reis, R. L. New Biotextiles for Tissue Engineering: Development, Characterization and in Vitro Cellular Viability. *Acta Biomater.* **2013**, *9* (9), 8167–8181. https://doi.org/10.1016/j.actbio.2013.05.019.

(82) Di Prima, G.; Licciardi, M.; Carfì Pavia, F.; Lo Monte, A. I.; Cavallaro, G.; Giammona, G. Microfibrillar Polymeric Ocular Inserts for Triamcinolone Acetonide Delivery. *Int. J. Pharm.* **2019**, *567* (April), 118459. https://doi.org/10.1016/j.ijpharm.2019.118459.

(83) Gigli, M.; Fabbri, M.; Lotti, N.; Gamberini, R.; Rimini, B.; Munari, A. Poly(Butylene Succinate)-Based Polyesters for Biomedical Applications: A Review in Memory of Our Beloved Colleague and Friend Dr. Lara Finelli. *Eur. Polym. J.* **2016**, *75*, 431–460. https://doi.org/10.1016/j.eurpolymj.2016.01.016.

(84) Miceli, G. C.; Martorana, A.; Cancilla, F.; Pitarresi, G.; Licciardi, M.; Palumbo, F. S. Synthesis, Characterization, and Processing of Highly Bioadhesive Polyurethane Urea as a Microfibrous Scaffold Inspired by Mussels. *ACS Appl. Polym. Mater.* **2023**, *5* (10), 8483–8494. https://doi.org/10.1021/acsapm.3c01578.

(85) Miceli, G. C.; Palumbo, F. S.; Bonomo, F. P.; Zingales, M. Polybutylene Succinate Processing and Evaluation as a Nano- Fibrous Graft for Tissue Engineering Applications. **2022**, 1–13.

(86) Vigni, G. E.; Cassata, G.; Caldarella, G.; Cirincione, R.; Licciardi, M.; Miceli, G. C.; Puleio, R.; D'Itri, L.; Lo Coco, R.; Camarda, L.; Cicero, L. Improved Bone Regeneration Using Biodegradable Polybutylene Succinate Artificial Scaffold in a Rabbit Model. *J. Funct. Biomater.* **2023**, *14* (1), 1–14. https://doi.org/10.3390/jfb14010022.

(87) Palumbo, F. S.; Federico, S.; Pitarresi, G.; Fiorica, C.; Giammona, G. Synthesis and Characterization of Redox-Sensitive Polyurethanes Based on L-Glutathione Oxidized and Poly(Ether Ester) Triblock Copolymers. *React. Funct. Polym.* **2021**, *166* (July), 104986. https://doi.org/10.1016/j.reactfunctpolym.2021.104986.

(88) Wang, R.; Zhang, F.; Lin, W.; Liu, W.; Li, J.; Luo, F.; Wang, Y.; Tan, H. Shape Memory Properties and Enzymatic Degradability of Poly(ε-Caprolactone)-Based Polyurethane Urea Containing Phenylalanine-Derived Chain Extender. *Macromol. Biosci.* **2018**, *18* (6), 1–11. https://doi.org/10.1002/mabi.201800054.

(89) Pfau, M. R.; Beltran, F. O.; Woodard, L. N.; Dobson, L. K.; Gasson, S. B.; Robbins, A. B.; Lawson, Z. T.; Brian Saunders, W.; Moreno, M. R.; Grunlan, M. A. Evaluation of a Self-Fitting, Shape Memory Polymer Scaffold in a Rabbit Calvarial Defect Model. *Acta Biomater.* **2021**, *136*, 233–242. https://doi.org/10.1016/J.ACTBIO.2021.09.041.

(90) Wienen, D.; Gries, T.; Cooper, S. L.; Heath, D. E. An Overview of Polyurethane Biomaterials and Their Use in Drug Delivery. *J. Control. Release* **2023**, *363*, 376–388. https://doi.org/10.1016/J.JCONREL.2023.09.036.

(91) Shi, R.; Xue, J.; He, M.; Chen, D.; Zhang, L.; Tian, W. Structure, Physical Properties, Biocompatibility and in Vitro/Vivo Degradation Behavior of Anti-Infective Polycaprolactone-Based Electrospun Membranes for Guided

Tissue/Bone Regeneration. *Polym. Degrad. Stab.* **2014**, *109*, 293–306. https://doi.org/10.1016/J.POLYMDEGRADSTAB.2014.07.017.

(92) Bennour, S.; Louzri, F. Study of Swelling Properties and Thermal Behavior of Poly(N,N-Dimethylacrylamide- Co -Maleic Acid) Based Hydrogels . *Adv. Chem.* **2014**, *2014*, 1–10. https://doi.org/10.1155/2014/147398.

(93) Baskić, D.; Popović, S.; Ristić, P.; Arsenijević, N. N. Analysis of Cycloheximide-Induced Apoptosis in Human Leukocytes: Fluorescence Microscopy Using Annexin V/Propidium Iodide versus Acridin Orange/Ethidium Bromide. *Cell Biol. Int.* **2006**, *30* (11), 924–932. https://doi.org/10.1016/j.cellbi.2006.06.016.

(94) Matos-Pérez, C. R.; Wilker, J. J. Ambivalent Adhesives: Combining Biomimetic Cross-Linking with Antiadhesive Oligo(Ethylene Glycol). *Macromolecules* **2012**, *45* (16), 6634–6639. https://doi.org/10.1021/ma300962d.

(95) Zhou, J.; Defante, A. P.; Lin, F.; Xu, Y.; Yu, J.; Gao, Y.; Childers, E.; Dhinojwala, A.; Becker, M. L. Adhesion Properties of Catechol-Based Biodegradable Amino Acid-Based Poly(Ester Urea) Copolymers Inspired from Mussel Proteins. *Biomacromolecules* **2015**, *16* (1), 266–274. https://doi.org/10.1021/bm501456g.

(96) Xu, Z.; Chen, L.; Lu, L.; Du, R.; Ma, W.; Cai, Y.; An, X.; Wu, H.; Luo, Q.; Xu, Q.; Zhang, Q.; Jia, X. A Highly-Adhesive and Self-Healing Elastomer for Bio-Interfacial Electrode. *Adv. Funct. Mater.* **2021**, *31* (1). https://doi.org/10.1002/adfm.202006432.

(97) Than, Y. M.; Suriyarak, S.; Titapiwatanakun, V. Rheological Investigation of Hydroxypropyl Cellulose–Based Filaments for Material Extrusion 3D Printing. *Polymers (Basel).* **2022**, *14* (6). https://doi.org/10.3390/POLYM14061108.

(98) Mackay, M. E. The Importance of Rheological Behavior in the Additive

Manufacturing Technique Material Extrusion. *Cit. J. Rheol.* **2018**, *62*, 1549. https://doi.org/10.1122/1.5037687.

(99) Aho, J.; Boetker, J. P.; Baldursdottir, S.; Rantanen, J. Rheology as a Tool for Evaluation of Melt Processability of Innovative Dosage Forms. *Int. J. Pharm.* **2015**, *494* (2), 623–642. https://doi.org/10.1016/J.IJPHARM.2015.02.009.

(100) Suwardie, H.; Wang, P.; Todd, D. B.; Panchal, V.; Yang, M.; Gogos, C. G. Rheological Study of the Mixture of Acetaminophen and Polyethylene Oxide for Hot-Melt Extrusion Application. *Eur. J. Pharm. Biopharm.* **2011**, *78* (3), 506–512. https://doi.org/10.1016/J.EJPB.2011.03.013.

(101) Elbadawi, M.; Gustaffson, T.; Gaisford, S.; Basit, A. W. 3D Printing Tablets: Predicting Printability and Drug Dissolution from Rheological Data. *Int. J. Pharm.* **2020**, *590*, 119868. https://doi.org/10.1016/J.IJPHARM.2020.119868.

(102) Azad, M. A.; Olawuni, D.; Kimbell, G.; Badruddoza, A. Z. M.; Hossain, M. S.; Sultana, T. Polymers for Extrusion-Based 3D Printing of Pharmaceuticals: A Holistic Materials–Process Perspective. *Pharmaceutics* **2020**, *12* (2). https://doi.org/10.3390/PHARMACEUTICS12020124.

(103) Pla, T. P. Deformation Behavior of 3D Printed Auxetic Structures Of. **2023**, No. 1, 1–19.

(104) Patti, A.; Acierno, S.; Cicala, G.; Acierno, D. Predicting the Printability of Poly(Lactide) Acid Filaments in Fused Deposition Modeling (FDM) Technology: Rheological Measurements and Experimental Evidence. *ChemEngineering* **2022**, *7* (1), 1. https://doi.org/10.3390/chemengineering7010001.

(105) Elbadawi, M. Polymeric Additive Manufacturing: The Necessity and Utility of Rheology. *Polym. Rheol.* **2018**. https://doi.org/10.5772/INTECHOPEN.77074.

(106) Kollamaram, G.; Croker, D. M.; Walker, G. M.; Goyanes, A.; Basit, A. W.;

Gaisford, S. Low Temperature Fused Deposition Modeling (FDM) 3D Printing of Thermolabile Drugs. *Int. J. Pharm.* **2018**, *545* (1–2), 144–152. https://doi.org/10.1016/J.IJPHARM.2018.04.055.

(107) Cuttaz, E.; Goding, J.; Vallejo-Giraldo, C.; Aregueta-Robles, U.; Lovell, N.; Ghezzi, D.; Green, R. A. Conductive Elastomer Composites for Fully Polymeric, Flexible Bioelectronics. *Biomater. Sci.* **2019**, *7* (4), 1372–1385. https://doi.org/10.1039/C8BM01235K.

(108) Abouelmagd, S. A.; Sun, B.; Chang, A. C.; Ku, Y. J.; Yeo, Y. Release Kinetics Study of Poorly Water-Soluble Drugs from Nanoparticles: Are We Doing It Right? *Mol. Pharm.* **2015**, *12* (3), 997–1003. https://doi.org/10.1021/MP500817H/SUPPL_FILE/MP500817H_SI_001.PDF.

(109) Gazaille, C.; Sicot, M.; Saulnier, P.; Eyer, J.; Bastiat, G. Local Delivery and Glioblastoma: Why Not Combining Sustained Release and Targeting? *Front. Med. Technol.* **2021**, *3*, 791596. https://doi.org/10.3389/FMEDT.2021.791596.

(110) Xu, R.; Xia, H.; He, W.; Li, Z.; Zhao, J.; Liu, B.; Wang, Y.; Lei, Q.; Kong, Y.; Bai, Y.; Yao, Z.; Yan, R.; Li, H.; Zhan, R.; Yang, S.; Luo, G.; Wu, J. Controlled Water Vapor Transmission Rate Promotes Wound-Healing via Wound Re-Epithelialization and Contraction Enhancement. *Sci. Rep.* **2016**, *6* (November 2015), 1–12. https://doi.org/10.1038/srep24596.

(111) Horakova, J.; Mikes, P.; Saman, A.; Svarcova, T.; Jencova, V.; Suchy, T.; Heczkova, B.; Jakubkova, S.; Jirousova, J.; Prochazkova, R. Comprehensive Assessment of Electrospun Scaffolds Hemocompatibility. *Mater. Sci. Eng. C* **2018**, *82*, 330–335. https://doi.org/10.1016/j.msec.2017.05.011.

(112) Pihlman, H.; Keränen, P.; Paakinaho, K.; Linden, J.; Hannula, M.; Manninen, I. K.; Hyttinen, J.; Manninen, M.; Laitinen-Vapaavuori, O. Novel Osteoconductive

β-Tricalcium Phosphate/Poly(L-Lactide-Co-e-Caprolactone) Scaffold for Bone Regeneration: A Study in a Rabbit Calvarial Defect. *J. Mater. Sci. Mater. Med.* **2018**, *29* (10). https://doi.org/10.1007/s10856-018-6159-9.